Development of CIELAB colour system for colorimetric detection of heavy metals in wastewater using metal nanoparticles.

by

Sindisiwe Fortunate Shange

(MAppSc: Chemistry)

Thesis submitted in fulfilment of the requirements for the degree of Doctor of Philosophy in Chemistry in the Faculty of Applied Sciences at Durban University of Technology

April 2021

Supervisor : **Prof. Phumlane Selby Mdluli**

Co-Supervisor : **Dr. Mbuso Mlambo**

DECLARATION

I, Sindisiwe Fortunate Muthwa hereby declare that this thesis is my original work and has not been presented for a degree award in any other university or institution for this or any other degree or award.

Student number: **20809282**

Sindisiwe Fortunate Muthwa

Declaration by Supervisors

This thesis has been submitted for examination with our approval as student Supervisors

Prof. Phumlane Selby Mdluli

Department of Chemistry,

Durban University of Technology,

P O Box 1334,

Durban, 4000, South Africa

Dr. Mbuso Mlambo

Department of Physics,

University of Pretoria,

Pretoria, 0002, South Africa

ACKNOWLEDGEMENTS

First and foremost, I would like to thank my God Almighty, Jesus Christ for his love, mercy and kindness at all times. Most of all for the grace to pursue my dream. “Nginamandla ukwenza konke ngaye ongiqinisayo”. (KwabaseFiliphi 4 vs 13)

I would like to extend my sincere gratitude to Prof. Phumlane S. Mdluli not only for gifting me this opportunity but also for the unique knowledge, sustained support and enthusiastic encouragement, he has afforded me over the past few years. Furthermore, I would like to thank Dr. Mbuso Mlambo for the opportunity and continuous support.

I would like to extend my humble and sincere gratitude to:

My pillar and my reason for breathing princess Snakekelwe Sbahle (**Bahleh**) and my prince my sweet son **Njabulo.**

My husband **Sbusiso Shange** for his motivation throughout my course of study, constant encouragement, always available when I need his assistance. I have never felt alone with you.

My mother Mrs. Nokuthula Muthwa, My brothers Thabani, Mbongeni and Sandile. My sisters Hlengiwe, Thembi and Mpume. My nieces Nosihle, Ozzie and Nonku. My nephews Nkanyiso, Mkhehla, Thando, Njabulo and Bandile. My wonderful grandchildren Thafa, Covid and Ling-Ling.

My lovely family in-law Mr. and Mrs Shange, my brothers in-law Thulane, Syabonga and Snenhlanhla. My sisters in-law Thenjiwe and Nomthandazo. My children Khanyi, Nonto, Zama, Luyanda, Amahle, Wandile, Oluhle, Melokuhle, Asiphile and Snakhokonke.

My sisters from another mother Makhosi and Nonto Zulu. You guys came into my life and gave me unconditional love. I’ll forever be grateful and I love you so much.

Dr. Talent Makhanya, Sis Mpumeh Cele, Sis Mavis, Avy Naicker, Sandile Majola, Sandile Sthole, Nyanga Cele and Zamo Miya for your continuous support, willingness to help and patience throughout this research.

Ncomeka Mgxadeni, Bakusele Kabane and Nkanyezi Kubheka for your words of encouragement, pushing me when I was slacking and you support.

Moses Kotane Institute and National Research Foundation for financial support.

DEDICATION

THIS DISSERTATION IS DEDICATED TO MY LATE FATHER MR. SIFISO A. MUTHWA.

Wawuhlale uthi uyawabona wonke lawa amanye amajazi. Wena olifunayo kumina “IJAZI ELIBOMVU”.

LALA KAHLE PHUNGAZA OMUHLE, UYOHLALA NJALO USENHLIZWENI YAMI

ABSTRACT

This study presents a simple colorimetric assay that was used to develop gold nanoparticles (AuNPs) enabled optical sensor. The sensor was fabricated using 3-(p-tolyl)-2,3-dihydropyrazolo[3,4-b] indole-1(4H)-carbothioamide (TRPIDA_CH_3) complex synthesized through one pot reaction of toluidine, thio-semi-carbazide and indole in the presence of indium chloride as a catalyst under reflux. The attained product was then characterized fully by Fourier Transform Infrared (FT-IR), ^{1}H and ^{13}C Nuclear Magnetic Resonance (NMR), Time of flight (Mass Spectroscopy (TOF-MS) and elemental analysis for selective detection of hexavalent chromium (Cr(VI)). Two well-separated Surface Plasmon Resonance (SPR) peaks were observed in the spectra at 520 nm and 645 nm, respectively. The introduction of Cr(VI) into TRPIDA_CH_3-AuNPs solution resulted in a decrease of SPR intensity at 520 nm with an increase of the peak at 645 nm. ImageJ software version 1.8.0_172 was used to measure the colour dynamics between the reaction of TRPIDA_CH_3-AuNPs and Cr(VI) for image processing. The CIE L*a*b* colour system was utilized to analyse the digital images obtained which were converted to CIE Yxy chromaticity diagram. The chromaticity diagram of gold nanoparticle TRPIDA_CH_3 complex was in agreement with colour change as observed from RGB values after addition of different concentration of the chromium standards. The obtained recoveries for both tap and river water which was spiked with chromium ranged from 72 to 101 % with a limit of detection (LOD) and limit of quantification (LOQ) of 0.14 and 0.47 µM, respectively. Nine possible interfering ions (Cr, Cu, Fe, Ni, Zn, Pb and Mn) were investigated and showed low detection, thus, indicating low interference with the analyte of choice. Additionally, a significant feature of this method is that it involves a simple technique exhibiting high selectivity to Cr(VI) over other heavy metal ions that were tested.

The application of CIE L*a*b*/Yxy colour space based on the TRPIDA_CH_3-AuNPs aggregation to quantify Cr(VI) in wastewater effluent was studied. The colorimetric sensor showed an excellent linear range of 0.01-100.0 µM (R^2=0.9856). Additionally, the residual plot showed that residual errors were randomly distributed, meaning we should accept the results of a linear regression. The wastewater effluent samples were collected over a period of 10 days and each sample was analysed in triplicate for statistical purposes. The concentration in the collected wastewater effluent samples were in the range of 0.5-25.0 µM. Furthermore, the measured concentrations of Cr(VI) in wastewater effluent samples using the proposed colorimetric method agreed with those obtained when using the traditional 1,5-diphenyl

carbazide (DPC) method. The DPC method also showed an excellent linear range of 10.0-100.0 µg/L (R^2=0.9955) with a residual plot showing random distribution of residual errors. The RGB colour coordinates of the TRPIDA_CH_3-AuNPs with wastewater effluent were compared with one without TRPIDA_CH_3-AuNPs to determine the effect of the TRPIDA_CH_3-AuNPs on the water samples.

Development of a Smartphone and spectrophotometric based systems for colorimetric detection of Cr(VI) using functionalized AuNPs supported by CIEL*a*b*/Yxy colour space and molecular dynamics was also conducted in this study. This demonstrated the comparative study of the application of smartphone as well as spectrophotometer as tools to detect colour variation of functionalized DPC-AuNPs. These tools were demonstrated for their potential use as a colorimetric device for detecting Cr(VI) in wastewater. Color Grab 3.6.1 app was used to capture and recognize colours from samples containing gold nanoparticles with different concentrations of chromium standards. The RGB values obtained were compared with those obtained from spectrophotometer. It was observed that DPC-AuNPs aggregated in the presence of Cr(VI), with clear colour change from pink to blue due SPR of AuNPs. This resulted in a decrease in the intensity of the SPR band at 520 nm and the formation of a new red-shifted band at 670 nm and a colour change from red to blue from UV-Visible spectra. The R colour coordinates decreased as Cr(VI) concentration was increased to 16 µM then a rapid decreased was noted between 18–25 µM and G and B colour coordinates followed the same trend. Colour difference *(ΔE)* increased significantly as the Cr(VI) concentration was increased. A rapid decrease was noticed in hue angle between 16-25 µM while chroma decreased significantly as the Cr(VI) concentration increased. Molecular dynamics using gold cluster was used to simulate the aggregation process. The radial distribution *[g(r)]* was calculated from cluster models. The radial distribution of Cr-DPC complex was more than two-fold than for Cr-AuNPs. This was associated with the aggregation of AuNPs leading to the appearance of blue colour of AuNPs solution which was also supported by the intensity obtained from Color Grab.

The other case study presented herein is on the development of a simple and facile colorimetric method for the detection of lead (Pb(II)) ions using silver nanoparticles (AgNPs) functionalized with 1-methyl-6-phenyl-6, 7-dihydro-5H-indolo [3, 2-c] [1, 8] naphthyridine (TRPIDB_H) ligand. The synthesized AgNPs were characterized by UV-Vis, TEM and Dynamic Light Scattering (DLS). The UV–Vis spectrum displayed a local surface Plasmon resonance (LSPR) absorption with a peak maximum at 410 nm and TEM results image showed that the

synthesised AgNPs were well dispersed in aqueous solution. The TRPIDB_H complex was synthesized through Povarov reaction [4+2] cycloaddition and yielded 80% of the product which was characterized by FT-IR, ^{1}H and ^{13}C NMR, TOF-MS. The Pb(II) ions induced aggregation of the TRPIDB_H-AgNPs in solution from 60-100 mg/L. This resulted in a colour change from yellow to reddish brown which was accompanied by the appearance of the second surface plasmon absorption peak at 505 nm.

Moreover, further study reported herein focus on the development of a rapid and efficient colorimetric method for the detection of Mn(II) with high selectivity and sensitivity using 3-(4-hydroxy-3-methoxyphenyl)-2, 3-dihydropyrazolo [3, 4-b] indole-1(4H)-carbothioamide (TRPIDA_V) modified gold nanoparticles (TRPIDA_V-AuNPs). The TRPIDA_V-AuNPs aggregated upon the introduction of 2 mg/L, this led to a change in colour of the dispersed TRPIDA_V-AuNPs from red to blue and a decrease of the surface plasmon absorption intensity at 520 nm. The TRPIDA_V-AuNPs aggregated between 2-10 mg/L resulting in the formation of a second peak at 655 nm. The colorimetric detection showed high selectivity to Mn(II) ions and was not selective to other investigated metal ions as there was no aggregation induced upon addition of 2 mg/L of other metal ions. Furthermore, only Mn(II) ion resulted in colour change from wine red to blue and forming a second absorption peak at 655 nm. Additionally, the colorimetric detection system yielded a detection limit of 0.00691 mg/L showing excellent sensitivity towards Mn(II). The results obtained on the spiked river and tap water samples further confirmed that the TRPIDA_V-AuNPs colorimetric detection system is applicable for Mn(II).

LIST OF CONTENTS

DECLARATION ..... **i**

ACKNOWLEDGEMENTS ..... **ii**

DEDICATION ..... **iii**

ABSTRACT ..... **iv**

LIST OF CONTENTS ..... **vii**

LIST OF TABLES ..... **xi**

LIST OF FIGURES ..... **xiii**

LIST OF EQUATIONS ..... **xviii**

LIST OF SCHEMES ..... **xix**

ACRONYMS AND SYMBOLS ..... **xx**

PUBLICATIONS AND CONFERENCE CONTRIBUTIONS ..... **xxiii**

CHAPTER ONE **1**

1.0 INTRODUCTION **1**

1.1 Background 1

1.2 Gold and Silver Nanoparticles as a colorimetric sensor 3

1.3 The properties of light 5

1.4 Colorimetric Assays 7

1.5 Problem Statement 11

1.6 Motivation 13

1.7 Aim and Objectives 15

1.8 Research Hypothesis 15

1.9 Thesis Outline 16

CHAPTER TWO **18**

2.0 LITERATURE REVIEW **18**

2.1 Heavy metals of interest 18

2.2 Gold and Silver Nanoparticles as an optical sensor for 21

2.2.1 Chromium 21
2.2.2 Lead 22
2.2.3 Manganese 23
2.3 Detection of chromium using functionalized AuNPs 29
2.4 Selectivity studies of Cr(VI), Pb(II) and Mn(II) using CIE L*a*b*/Yxy chromaticity analysis. 34
2.5 Detection limits of Cr(VI), Pb(II) and Mn(II) 38
CHAPTER THREE 40
3.0 MATERIALS AND METHODS 40
3.1 Experimental 40
3.1.1 Chemicals and Reagents 40
3.1.2 Characterization of AuNPs, AgNPs and ligand complexes 40
3.1.3 Synthesis of gold and silver nanoparticles. 41
3.1.4 Synthesis of functionalization complex ligands 42
3.1.5 Fabrication of AuNPs and AgNPs with complex ligands 43
3.1.6 Preparation of working standards 46
3.1.7 Selectivity Studies 47
3.1.8 Analysis of the intensity of colours using a smartphone 47
3.1.9 Computational simulations 47
3.1.10 Conversion of RGB colour coordinates to XYZ and CIE L*a*b* colour space 48
3.1.11 Optical properties and image processing 49
CHAPTER FOUR 50
CASE STUDY I 50
4.1 Synthesis and characterization of 3-(p-tolyl)-2,3-dihydropyrazolo[3,4-b] indole-1 (4H)-carbothioamide functionalized gold nanoparticles for the CIEL*a*b*/Yxy colorimetric detection of Cr(VI) 50
4.1.1 Characterization of synthesized citrate capped AuNPs 50

4.1.2 Characterization of the synthesized TRPIDA_CH_3 50
4.1.3 Optimization of RGB colour coordinates and CIE L*a*b* colour system 53
4.1.4 Colorimetric sensing of Cr(VI) 60
4.1.5 Selectivity and sensitivity of the sensor 63
4.1.6 Practical application 67
4.1.7 Application of optimized conditions in wastewater effluent samples 69
4.1.8 Colorimetric sensing of wastewater effluent samples 74
4.1.9 Application of CIEL*a*b* to wastewater effluent samples 75
4.1.10 Analysis of wastewater effluent samples 78
4.1.11 Statistical analysis or wastewater effluent samples 80
CHAPTER FIVE 83
CASE STUDY II 83
5.1 Development of a Smartphone and spectrophotometric based systems for colorimetric detection of hexavalent chromium using 1,5-diphenylcarbazide functionalized gold nanoparticles supported by CIE L*a*b*/Yxy colour space and molecular dynamics. 83
5.1.1 Sensitivity of the response of DPC-AuNPs to Cr(VI) 83
5.1.2 Image analysis using RGB colour coordinates and CIE La*b*/Yxy colour system 87
5.1.3 Qualitative and quantitative analysis of the response of DPC-AuNPs to Cr(VI) 89
5.1.4 Molecular simulation of DPC-AuNPs to Cr(VI) 91
CHAPTER SIX 94
CASE STUDY III 94
6.1 Understanding interaction between 1-methyl-6-phenyl-6, 7-dihydro-5H-indolo [3, 2-c] [1, 8] naphthyridine complex with silver nanoparticles and Pb(II): a CIE L*a*b*/Yxy and RGB colour coordinates study 94
6.1.1 Characterization of unmodified AgNPs 94

6.1.2 Characterization of 1- methyl-6-phenyl-6, 6a, 7, 11b-tetrahydro-5H-indolo [3, 2 - c] [1, 8] naphthyridine. 95
6.1.3 Characterization of TRPIDB_H-AgNPs aggregation 96
6.1.4 RGB colour coordinates measurements 99
6.1.5 Optimization of CIE L*a*b* colour space 100
6.1.6 Intensity and colour difference analysis 101
6.1.7 Hue and chroma evaluations 102
6.1.8 Chromaticity system 103
CHAPTER SEVEN 104
7.0 CASE STUDY FOUR 104
7.1 Colorimetric detection of Mn(II) using 3-(4-hydroxy-3-methoxyphenyl)-2, 3-dihydropyrazolo [3, 4-b] indole-1(4H)-carbothioamide capped gold nanoparticles: A CIE L*a*b*/Yxy colour space study. 104
7.1.1 Characterization of TRPIDA_V complex 104
7.1.2 Optimization of TRPIDA_V-AuNPs colorimetric sensor 105
7.1.3 Selectivity and sensitivity of Mn(II) 108
7.1.4 Image processing 110
7.1.5 Detection of river and tap water samples 113
CHAPTER EIGHT 114
8.0 CONCLUSIONS 114
REFERENCES 116

LIST OF TABLES

Table 1.1: Colour appearance and corresponding wavelengths 6

Table 2.1: Showing the preparation of AuNPs by Turkevich method 25

Table 2.2: Showing chromium, lead and manganese sensing based on AuNPs aggregation using different capping ligands. 26

Table 2.3: Showing the image analysis of standard solutions for the detection of Cr(VI), Pb(II) and Mn(II). 31

Table 2.4: Showing the CIE L*a*b* chromaticity and RGB colour models of interfering ions for the detection of Cr(VI), Pb(II) and Mn(II). 35

Table 2.5: Showing reported LOD's of functionalized AuNPs and AgNPs for the detection of Cr(VI), Pb(VI) and Mn(II). 38

Table 4.1: Showing RGB values, CIE L*a*b/Yxy colour space, colour difference, hue angle and chroma of Cr(VI) standards 56

Table 4.2: showing recovery values of spiked Cr(VI) in tap and river water samples and the relative standard deviation (RSD) values of each sample (n=3) 69

Table 4.3: Showing colorimetric data obtained from photographic images of effluent wastewater samples. 76

Table 4.4: Showing colorimetric data obtained from photographic images of effluent wastewater samples and TRPIDA_CH_3-AuNPs as a blank 77

Table 4.5: Showing TRPIDA_CH_3-AuNPs and DPC method results the detection of Cr(VI) in wastewater effluent samples. 79

Table 4.6: t-Test: Paired Two Sample for Means 81

Table 4.7: F-Test Two-Sample for Variances 82

Table 5.1: Showing photograph images of the DPC-AuNPs blank and different concentrations of Cr(VI) in the range of 0.5-50.0 µM, captured by smartphone using Color Grab. 85

Table 7.1: Showing the %Recovery and %RSD of the proposed colorimetric sensor for the detection of Mn(II)..... 113

LIST OF FIGURES

Figure 1.1: Schematic representation of the synthesis of citrate-stabilized AuNPs by Turkevich method (Shiraishi et al. 2017). 4

Figure 1.2: Diagram of preparation methods of silver nanoparticles obtained in aqueous solutions (Zielińska et al. 2009)..... 5

Figure 1.3: Electromagnetic spectrum (Shen 2003)..... 6

Figure 1.4: The three-dimensional colour space defined by lightness (L), red versus green (a*) and yellow versus blue (b*) (Choudhury and Chatterjee 1996). 9

Figure 1.5: CIE 2° and 10° Standard observers (Sharma 2018) 10

Figure 1.6: (a) CIE 1931 (x,y) chromaticity diagram and (b) Chromaticity diagram (Sharma 2018). 11

Figure 4.1: (a) UV-Vis spectra of the citrate capped AuNPs and (b) TEM image of AuNPs sample at 20 nm scale (insert of corresponding particle size distribution). 50

Figure 4.2: (a) IR spectrum of TRPIDA_CH_3 and (b) numbers for peripheral atoms of TRPIDA_CH_3 51

Figure 4.3: (a) ^{1}H NMR spectrum for TRPIDA_CH_3 and (b) ^{13}C NMR spectrum for TRPIDA_CH_3 52

Figure 4.4: TOF-MS spectrum for TRPIDA_CH_3..... 52

Figure 4.5: Photograph of the TRPIDA_CH_3-AuNPs in the presence of Cr(VI), the volume ratio of TRPIDA_CH_3-AuNPs and Cr(VI) was 700 µL:300 µL..... 53

Figure 4.6: (a) Graph of intensity vs. concentration of Cr(VI) TRPIDA_CH_3-AuNPs (blank) 0.01-100 µM and (b) representative plots of absorbance vs concentration of Cr(VI) TRPIDA_CH_3-AuNPs (blank) 0.01-100 µM. 54

Figure 4.7: (a) Illustration of the R, G, and B colour combination dynamics for the corresponding to Cr(VI) concentration and (b) chromaticity diagram of TRPIDA_CH_3-AuNPs and Cr(VI) standards 0-100 µM. 57

Figure 4.8: (a) Plots of L*a*b* values against concentration, (b) plot of colour difference against concentration and (c) plot of chroma and hue angle *vs.* concentration. 59

Figure 4.9: (a) UV-Vis spectra of the TRPIDA_CH_3-AuNPs (blank) and after addition of different concentrations of Cr(VI) ranging from 0.01 to 100.0 µM, (b) UV-Vis analysis resultant plot for the evaluation of ionic strength on the performance of TRPIDA_CH_3-AuNPs as efficient sensors for the detection of Cr(VI), measured at 520 nm and 645 nm.... 61

Figure 4.10: (a) Photograph image of colorimetric response of interfering metal ions and Cr(VI) at different concentrations and (b) chromaticity image of interfering metals and Cr(VI). 64

Figure 4.11: (a) UV-Vis spectra of the blank of the proposed sensor in the presence of interfering metal ions and Cr(VI) and (b) bar graph showing responses of interfering metal ions. 65

Figure 4.12: (a) Graph of absorbance at 645/520 nm wavelength *vs.* concentration of Cr(VI) TRPIDA_CH_3-AuNPs (blank) 0.01-100 µM and (b) representative plots of exact concentration *vs* prepared concentration of Cr(VI) TRPIDA_CH_3-AuNPs (blank) 0.01-100 µM. 66

Figure 4.13: (a) Colorimetric scheme with corresponding calculated mean RGB values, (b) chromaticity image of Cr(VI) standards and real water samples 67

Figure 4.14: UV-Vis spectra of Cr(VI) standards and real water samples. 68

Figure 4.15: (a) Photograph image of filtered wastewater effluent samples from Day 1-10 and (b) photograph image of wastewater effluent from Day 1-10 and TRPIDA_CH_3-AuNPs (700:300 µL) as blank. 70

Figure 4.16: a) Photograph images of the TRPIDA_CH_3-AuNPs in the presence of different concentrations of Cr(VI) in the range of 0.01-100 µM and (b) UV–Vis spectra of the TRPIDA_CH_3-AuNPs after the addition of different concentrations of Cr(VI) in the range of 0.01-100 µM. 71

Figure 4.17: (a) Plot of absorbance @ 645/520 nm versus the concentrations of Cr(VI) in the range of 0.01–100 µM and (b) residual plot of absorbance against concentration 72

Figure 4.18: (a) Photographs of DPC in the presence of different concentrations of Cr(VI) in the range of 10-100 µg/L, (b) Plot of 540 nm vs the concentrations of Cr(VI) in the range of 10–100 µg/L and (c) residual plot of absorbance against concentration. 73

Figure 4.19: UV–Vis absorption spectra of TRPIDA_CH_3-AuNPs after the addition of wastewater effluent samples from Day 1-10. 74

Figure 4.20: Bar graph showing exact concentration of Cr(VI) detected in wastewater effluent using the TRPIDA_CH_3-AuNPs and DPC method over a period of 10 days. 80

Figure 5.1: (a) Photograph image of the DPC-AuNPs blank and different concentrations of Cr(VI) in the range of 0.5-50.0 µM, (b) concentration-dependent extinction spectra of the DPC-AuNPs blank and different concentrations of Cr(VI) in the range of 0.5-50.0 µM and (c) TEM image of AuNPs sample at 20 nm scale 84

Figure 5.2: (a) RBG colour plot against the corresponding Cr(VI) concentration (Color Grab) and (b) RBG colour plot against the corresponding Cr(VI) concentration (UV spectrophotometer) 88

Figure 5.3: (a) Plots of L*a*b* against Cr(VI) concentration (Color Grab) and (b) plots of L*a*b* against Cr (VI) concentration (UV spectrophotometer). 88

Figure 5.4: (a) Plot of colour difference against Cr(VI) concentration (Colour Grab) and (b) plot of colour difference against Cr(VI) concentration (UV spectrophotometer). 89

Figure 5.5: (a) Plots of hue angle and chroma values against Cr(VI) concentration (Color Grab) and (b) Plots of hue angle and chroma values against Cr(VI) concentration (UV spectrophotometer). 90

Figure 5.6: (a) Chromaticity image of calibration standards of Cr(VI) (colour Grab) and (b) chromaticity image of calibration standards of Cr(VI) (UV spectrophotometer). 91

Figure 5.7: Model for simulation DPC-AuNPs and Cr (VI) (a) DPC-AuNPs and (b) Cr-DPC-AuNPs. 92

Figure 5.8: Radial distribution function for DPC-AuNPs and Cr(VI) (a) DPC-AuNPs, (b) Cr-AuNPs and (c) Cr-DPC. 93

Figure 6.1: (a) UV-Vis absorption spectrum showing maxima at 410 nm, (b) TEM image of the synthesized AgNPs and (c) shows average particle distribution by DLS. 94

Figure 6.2: (a) IR spectrum and (b) TOF-MS spectrum for TRPIDB_H 95

Figure 6.3: ^{1}H NMR spectrum and (b) ^{13}C NMR spectrum for TRPIDB_H 96

Figure 6.4: (a) Photographic image of TRPIDB_H-AuNPs (blank) in the presence of Pb(II) and (b) UV-Vis spectra of TRPIDB_H-AuNPs in the presence of Pb(II) concentration in the range of 1-100 mg/L..... 97

Figure 6.5: Plot of RGB colour coordinates vs concentration of Pb(II) in the range of 1-100 mg/L. 99

Figure 6.6: Plot of CIEL*a*b* values vs concentration of Pb(II) in the range of 1-100 mg/L. 100

Figure 6.7: Plot of colour intensity *vs* concentration of Pb(II) *black line and plot of colour difference *vs* concentration of Pb(II) (blue line) 101

Figure 6.8: Plot of hue *vs* concentration of Pb(II) (black line) and plot of chroma *vs* concentration of Pb(II) (blue line)..... 102

Figure 6.9: Chromaticity diagram of TRPIDB_H-AgNPs in the presence of Pb(II) concentration in the range of 1-100 mg/L. 103

Figure 7.1: (a) IR spectrum and (b) TOF-MS spectrum for TRPIDA_V 104

Figure 7.2: ^{1}H NMR spectrum and (b) ^{13}C NMR spectrum for TRPIDA_V 105

Figure 7.3: UV-Vis spectra of TRPIDA_V-AuNPs (blank) and different concentrations of Mn(II) in the range of 0.5-10.0 mg/L. 106

Figure 7.4: (a) Photographic image and (b) UV–Vis spectra of the TRPIDA_V-AuNPs in the presence of different metal ions at 2mg/L 108

Figure 7.5: (a) Plot of absorbance (@655/520 nm) *vs* concentration and (b) plot of residual absorbance *vs* concentration of Mn(II)in the range of 0,10 mg/L. 109

Figure 7.6: (a) Photographic image of TRPIDA_V-AuNPs and Mn(II) and (b) plot of RGB values *vs* Mn(II) concentration in the range of 0-10 mg/L..... 110

Figure 7.7: (a) Plot of XYZ values *vs* Mn(II) concentration and (b) plot of L*a*b* values *vs* Mn(II) concentration in the range of 0-10 mg/L. 111

Figure 7.8: (a) Plot of colour difference (black line) and plot of colour intensity (blue line) *vs* Mn(II) concentration and (b) plot of hue (black line) and *vs* Mn(II) concentration..... 112

LIST OF EQUATIONS

Equation 1-1..... 5

Equation 2-1……29

Equation 2-2……29

Equation 2-3……29

Equation 3-1……48

Equation 3-2……49

Equation 4-1…….....54

LIST OF SCHEMES

Scheme 3.1: Outline synthesis of TRPIDA_CH_3 complex 42

Scheme 3.2: Outline synthesis of TRPIDB_H 42

Scheme 3.3: Outline synthesis of TRPIDA_V complex. 43

Scheme 3.4: Proposed mechanism for the modification of AuNPs with TRPIDA_CH_3 44

Scheme 3.5: Proposed mechanism for the modification of AuNPs with DPC 44

Scheme 3.6: Fabrication of gold nanoparticles with TRPIDB_H 45

Scheme 3.7: Proposed mechanism for the modification of AuNPs with TRPIDA_V 45

Scheme 3.8: Segmentation method of image processing 49

Scheme 4.1: Pathway for colorimetric colour change of TRPIDA_CH_3 AuNPs upon the addition of chromium(VI) (Muthwa et al. 2020). 62

Scheme 6.1: Schematic of aggregating process of TRPIDB_H-AgNPs induced by adding Pb (II) 98

Scheme 7.1: Schematic illustration of the detection mechanism of Mn(II) ions based on the aggregation of TRPIDA_V modified AuNPs. 107

ACRONYMS AND SYMBOLS

$-NH_2$	- Amine group
As	- Arsenic
Cd-TSPP	- Cadmium(II) meso-Tetrakis (4-sulfophenyl) porphyrin
CF	- Calixarene
^{13}C NMR	- Carbon 13 Nuclear Magnetic Resonance
COOH	- Carboxyl group
Cr	- Chromium
Co	- Cobalt
ΔE	- Colour Difference
Cu	- Copper
CMYK	- Cyan Magenta Yellow (Black)
DNA	- Deoxyribonucleic Acid
ssDNA	- Single-Stranded Deoxyribonucleic Acid
dsDNA	- Anti-Double Stranded Deoxyribonucleic Acid
DPC	- 1,5-Diphenyl Carbazide
DPP	- Diphenyl Phosphine
ETAAS	- Electrothermal Atomic Absorption Spectrometry
V	- Five
FAAS	- Flame Atomic Absorption Spectrometry
IV	- Four
FT-IR	- Fourier Transform Infrared Spectroscopy
AuNPs	- Gold nanoparticles
HPLC	- High Performance Liquid Chromatography

HSL	- Hue, Saturation, Lightness
IDA	- Iminodiacetic Acid
CIE	- International Commission on Illumination
ICP-MS	- Inductively Coupled Plasma Mass Spectroscopy
ICP-OES	- Inductively Coupled Plasma Optical Emission Spectroscopy
Fe	- Iron
Pb	- Lead
Mn	- Manganese
4-MBA	- 4-Mercaprobenzoic Acid
MUA	- Mercaptoundecanoic Acid
MA	- Melamine
Hg	- Mercury
µg/L	- Micro grams per litre
µM	- Micro molar
MDL	- Minimum Detection Limit
M^n	- Mixed ions
Ni	- Nickel
NMR	- Nuclear Magnetic Resonance
TRPIDA_CH_3	-3-(p-tolyl)-2,3-dihydropyrazolo[3,4-b] indole-1(4H) carbothioamide
TRPIDA_V	- 3-(4-hydroxy-3-methoxyphenyl)-2, 3-dihydropyrazolo [3, 4-b] indole-1(4H)-carbothioamide
TRPIDB_H	- 1-methyl-6-phenyl-6,7-dihydro-5H-indolo [3, 2-c] [1, 8] naphthyridine
ppb	- Parts per billion
ppm	- Parts per million
PVA	- Polyvinyl Alcohol

PVP	- Polyvinyl Pyrrolidone
^{1}H	- Proton Nuclear Magnetic Resonance
RGB	- Red, Green and Blue
AgNPs	- Silver Nanoparticles
VI	- Six
SPR	- Surface Plasmon Resonance
III	- Three
TOF-MS	- Time of Flight Mass Spectroscopy
$P_3O_{10}^{5-}$	- Tripolyphosphate
II	- Two
US-EPA	- United States Environmental Protection Agency
UV-Vis	- Ultraviolet-Visible Spectroscopy
WHO	- World Health Organization
Zn	- Zinc

PUBLICATIONS AND CONFERENCE CONTRIBUTIONS

Journal Articles Published

1. Fabrication of smartphone-based colorimetric device for detection of water leaks. Zodidi Gcolotela, Stanley Chibuzor Onwubu, Sindisiwe Fortunate Muthwa and Phumlane Selby Mdluli. 2021 “Water SA Journal” 47 (2) 247-252. https://doi.org/10.17159/wsa/2021.v47.i2.10920
2. Synthesis and characterization of 3-(p-tolyl)-2,3-dihydropyrazolo[3,4-b] indole-1, (4H)-carbothiamide functionalized gold nanoparticles for the CIEL*a*b*/Yxy colorimetric detection of Cr (VI). Sindisiwe F. Muthwa, Talent R. Makhanya, Mbuso Mlambo, Nosipho Moloto, Ndivhuwo P. Shumbula, Poslet M. Shumbula, Stanley C. Onwubu, Robert M. Gengan and Phumlane S. Mdluli. 2020 “Journal of Molecular Structure” (1209) 1279-1285. https://doi.org/10.1016/j.molstruc.2020.127985
3. Optimization of CIEL*a*b*/Yxy colour system for the colorimetric devices fabricated with gold nanoparticles. Sibongile E. Magubane, Mbuso Mlambo, Mbongeni H. Mabaso, Sindisiwe F. Muthwa, Hendrik G. Kruger and Phumlane S. Mdluli. 2019 “Journal of Molecular Structure” (1192) 271-277. https://doi.org/10.1016/j.molstruc.2019.04.092

Journal Articles Ready for Submission

1. Development of a smartphone and spectrophotometric based systems for colorimetric detecting chromium using functionalized gold nanoparticles supported by CIEL*a*b* colour space and molecular dynamics.
2. A review of the application of CIEL*a*b*/Yxy chromaticity for the development of Metal nano-enable colorimetric assays for the detection of chromium (Review article).
3. Application of CIEL*a*b*/Yxy colour system for the quantification of Cr (VI) in wastewater effluent using 3-(p-tolyl)-2,3-dihydropyrazolo[3,4-b]indole-1(4H)-carbothioamide functionalized gold nanoparticles.
4. Understanding interaction between 1-methyl-6-phenyl-6, 7-dihydro-5H-indolo [3, 2-c] [1, 8] naphthyridine complex with silver nanoparticles and Pb (II): a CIE lab/Yxy and RGB colour coordinates study.

5. Colorimetric detection of Mn (II) using 3-(4-hydroxy-3-methoxyphenyl)-2, 3-dihydropyrazolo [3, 4-b] indole-1(4H)-carbothioamide modified gold nanoparticles: A CIEL*a*b*/Yxy colour space study.

Conferences Attended

1. 3rd International Women in Science (STEM) Conference, East London, South Africa, 17-20 February 2020 (*Poster Presentation*)
2. Synthesis and characterization of TRPIDA_CH_3 complex for the detection of CIEL*a*b*/Yxy colour system for colorimetric detection of Cr (VI) in wastewater using TRPIDA_CH_3 functionalized gold nanoparticles.**Sindisiwe Muthwa**, Talent Makhanya, Mbuso Mlambo and Phumlane Mdluli
3. 4th BRICS Young Scientist Forum, Rio de Janeiro, 6-8 November 2019 (*oral presentation*). Synthesis and characterization of TRPIDA_CH_3 complex for the optimization of CIEL*a*b*/Yxy colour system for colorimetric detection of Cr (VI) using functionalized gold nanoparticles. **S.F Muthwa (Young Innovator)**

CHAPTER ONE

1.0 INTRODUCTION

1.1 Background

Currently the world is faced with wastewater management challenges and the associated impact in the ecosystem (Hong *et al.* 2017; Odinga 2018), which is due to a gradual increase in the heavy industrialization processes (Akpor and Muchie, 2010). The demand for potable water and environmental degradation could easily be moderated by the reuse of wastewater mainly in the developing countries where quantity rather than quality is preferred (Sheng *et al.* 2010; Jhansi and Mishra 2013).

Wastewater from municipalities and industries is composed predominantly of organic and inorganic and biological components including viruses, bacteria and metal ions (Odinga 2018). Beyond allowable limits in treated wastewater some of these components are probable to cause adverse effects on human and aquatic life (Dunn *et al.* 2014). Normally wastewater is discharged into small and large water bodies, then interacts with the biotic and abiotic factors leading to various forms of environmental changes . Skillful management of water resources is certain in order to sustainably use water for purposes such as crop irrigation, industrial and domestic supply, recreation and commercial fisheries waste disposal (OB, Muchie and Essays 2010; Baysal *et al.* 2013).

Municipal wastewater has been treated using conventional treatment systems over the years. However, some of these systems are not designed to remove pollutants such as heavy metals, pathogens and nitrogenous compounds (Abira 2008; Odinga 2018). These methods are also labour intensive, expensive to manage, prone to system failure and are probable to increase pollution by the generation of sludge as a by-product (Baysal *et al.* 2013; Hamadeh *et al.* 2014; Odinga 2018). The overall treatment efficiency is eventually lowered by the conventional systems retaining large amounts of suspended solids and environmentally toxic agents such as some algae (Hamadeh *et al.* 2014). Proficient disposal of wastewater, reuse and management of treatment systems remains one of the major challenges facing South Africa today (Dungeni and Momba 2010; Odinga 2018).

Heavy metal ions are usually toxic and have harmful effect on human health and welfare. They are considered as environmental pollutants and are recognised with potential life-threatening hazards. Usually these are metals in group 2, 3, 4, and 6 in the periodic table (Odinga 2018). Toxic metals are also naturally occurring elements that are potentially hazardous to both terrestrial and aquatic environments when present above tolerable limits (Krishna, Fulekar and Patakg 2012). According to (Parmar, Thakur and sciences) main sources of metals pollution in the environment arised from mining activities, battery factories, e-waste smelting activities, and automobile emissions (Parmar, Thakur and sciences 2013). Traces of heavy metals usually occur in water where some get immobilized in the sediment and form complexes with oxides and hydroxides of Iron (Fe) and other particulate matter. High concentration of Lead (Pb), Mercury (Hg), Arsenic (As) and Cadmium (Cd) are known to cause cancer, renal and liver damage and even affects the central nervous system (Chai *et al.* 2010; Guo *et al.* 2011; Qi, Shang and Wu 2012). It is, therefore, necessary to effectively treat wastewater suspected of having metal concentration beyond acceptable limits. Therefore, excessive and improper disposal of these heavy metals is a major concern as it is hazardous and affects the normal functioning of ecosystem.

The estimation of these metal contaminants in drinking water and the delay in detection has been the cause of several health issues in humans. Heavy metals enter subsistent wastewater in enormous quantities through various methods leading to a direct or indirect harm to the environment and human because of its wide application in modern industries. When discharged in wastewater they can ultimately have an adverse biological and ecological effects on fauna, flora and humans. Sensitive and selective detection of heavy metal ions in environmental waters has become crucial for controlling the quality of discharged water. Heavy metals such as cobalt, lead, copper, zinc, nickel, iron, chromium, mercury and cadmium are non-biodegradable (Xin *et al.* 2012).

1.2 Gold and Silver Nanoparticles as a colorimetric sensor

Gold nanoparticles (AuNPs) are one of the known effective colorimetric nano-probes for the detection of ions (Wu, Chen and Sung 2011; Tripathy, Woo and Han 2013; Wang *et al.* 2013; Sung and Wu 2014; Zhou *et al.* 2014), drugs (Kong *et al.* 2011; Zheng, Wang and Yang 2011) and biomolecules (Hemmateenejad, Shakerizadeh-shirazi and Samari 2014; Imene *et al.* 2014; Hosseini *et al.* 2015; Shamsipur *et al.* 2016) due to their extremely high extinction coefficient at visible region and strong surface plasmon resonance (SPR) absorption properties (Shahrivari, Faridbod and Ganjali 2018). The SPR absorption of AuNPs can be affected by the distance between particles shape, size, dielectric constant of the environment and presence of other species in the solution (Daniel and Astruc 2004; Chen *et al.* 2013; Oliveira *et al.* 2015).

Turkevich established the first systematic method to synthesize gold and silver nanoparticles (Turkevich 1985). The method involves the reaction of boiling gold (III) chloride tri-hydrate solution with small volume of warm sodium tri-citrate solution under thorough stirring that lead to a series of colour change from light yellow (to purple or black which faded in seconds in solution) and finally changed to wine red. The main principle was that the gold ions (Au(III)) of chloroauric acid in solution were reduced to gold atoms (Au^0) by the reducing agent tri-sodium citrate leading to the formation of well-dispersed spherical nanoparticles (Lin *et al.* 2016). The mechanism for stepwise formation of AuNPs was reported to be based on three stages after citrate reduction: Nucleation, gold adsorption growth and aggregation as can be observed in Figure 1.1 (Doyen, Bartik and Bruylants 2013; Kim *et al.* 2017). This by far is the most used method to produce highly stable mono dispersed nanoparticles ranging from 5-30 nm in average diameter in the aqueous phase (Sivaraman, Kumar and Santhanam 2011). This method has an advantage of flexibility to modify the concentration ranges for the reagents used in the synthesis to produce even bigger stable nanoparticles without changing the spherical morphology of the particles. Figure 1.1 shows the preparation of metal nanoparticles by the Turkevich method.

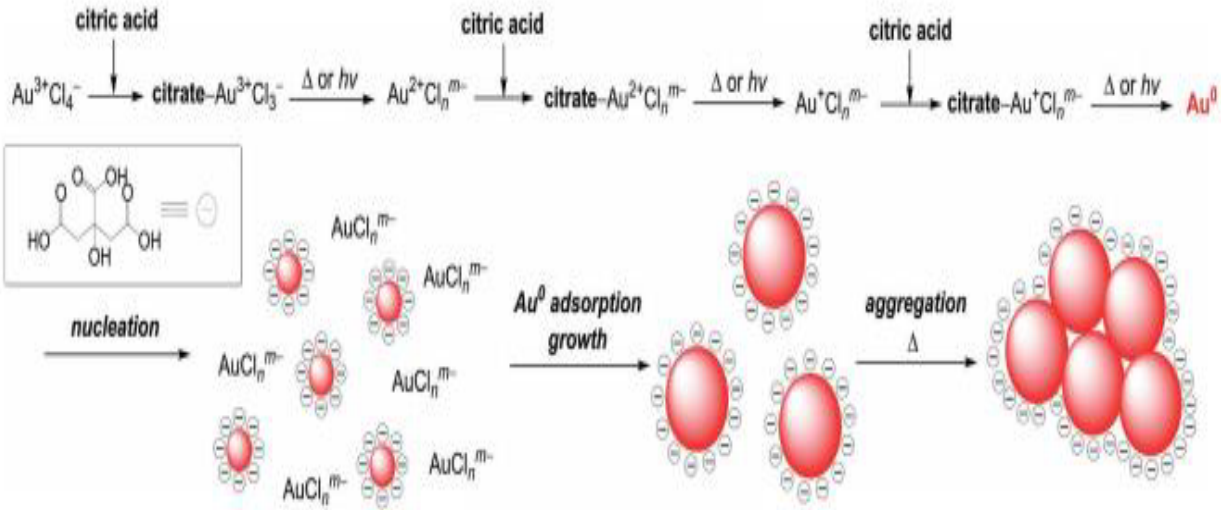

Figure 1.1: Schematic representation of the synthesis of citrate-stabilized AuNPs by Turkevich method (Shiraishi et al. 2017).

A search for environmentally sustainable synthetic process of silver nanoparticles has led to a few biomimetic approaches (Liang *et al.* 2014). This approach must be evaluated based on a green chemistry perspective which includes (i) selection of a suitable solvent medium, (ii) selection of environmentally benign reducing and capping agent which comprises extracts from plants or bio organisms or a combination of biomolecules found in these extracts such as enzymes/proteins amino acids, polysaccharides, and vitamins and (iii) selection of non-toxic substances to stabilize the particles (Xing *et al.* 2011). The surface plasmon resonance properties of AgNPs have recently been examined for agglomeration, uptake and interaction in a variety of live cells with a high illumination system (Xing *et al.* 2011). Silver is safe for human cells in small concentrations but lethal for the majority of bacteria and viruses and hence it was widely used in disinfection of water and food in everyday life and in the infection control in medicine (Lee and El-Sayed 2006). Optical properties of AgNPs have also received much attention due to their potential in advanced photonic and sensor applications (Liang *et al.* 2014).

Numerous methods for the synthesis of AgNPs have been reported which includes chemical reduction (Balavigneswaran *et al.* 2014), thermal decomposition (Campbell and Compton 2010), laser ablation (Sharif *et al.* 2015), and sonochemical synthesis (Welch and Compton 2006). Chemical reduction method and laser ablation method are the most employed synthetic methods. The chemical reduction method involved the reduction of metal salt like silver nitrate in an appropriate medium using various reducing agents like citrate, borohydride, etc. to produce colloidal suspensions integrated by NPs (Turkevich 1985). Lee and Meisel reported citrate reduction method where silver nitrate (90 mg) was dissolved in 500 mL of distilled water

and brought to boiling. A solution of 1% sodium citrate (10 mL) was added and the solution was kept on boiling for 1 h. The resulting colloid was greenish yellow and had absorption maximum at 420 nm (Lee and Meisel 1982). The effect of polyvinyl pyrrolidone (PVP) and polyvinyl alcohol (PVA) on the stabilization of obtained colloids was investigated by Zielinska *et. al* in Figure 1.2.

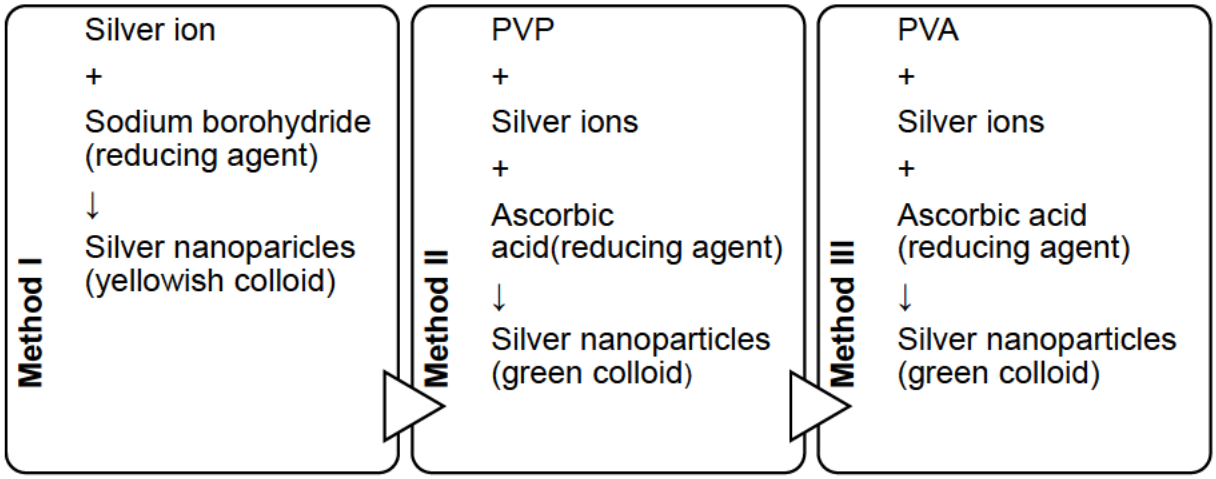

Figure 1.2: Diagram of preparation methods of silver nanoparticles obtained in aqueous solutions (Zielińska et al. 2009)

1.3 The properties of light

Light is an electromagnetic wave in a narrow band of the electromagnetic spectrum (Hearn and Baker 2004). In the spectrum, the different lights correspond to difference in either frequency *f* or wavelength λ. The speed of light (*c*) of the wave is directly proportional to the wavelength and frequency. While the wavelength and frequency are inversely proportional to each other as shown in Equation 1-1.

$$c = \lambda f \qquad \text{Equation 1-1}$$

The wavelength is measured in nano-meters (nm). The visible wavelengths are from 400 nm to 700 nm in Figure 1.3. A distinct colour within the spectrum corresponds to each frequency value. There is a steady transition from one colour to another so that no colour in the spectrum ends abruptly. However, each colour blends efficiently into the next (Gonzalez and Woods 2002; Beebe 2019). The main spectral and their approximate wavelength ranges are listed in Table 1.1.

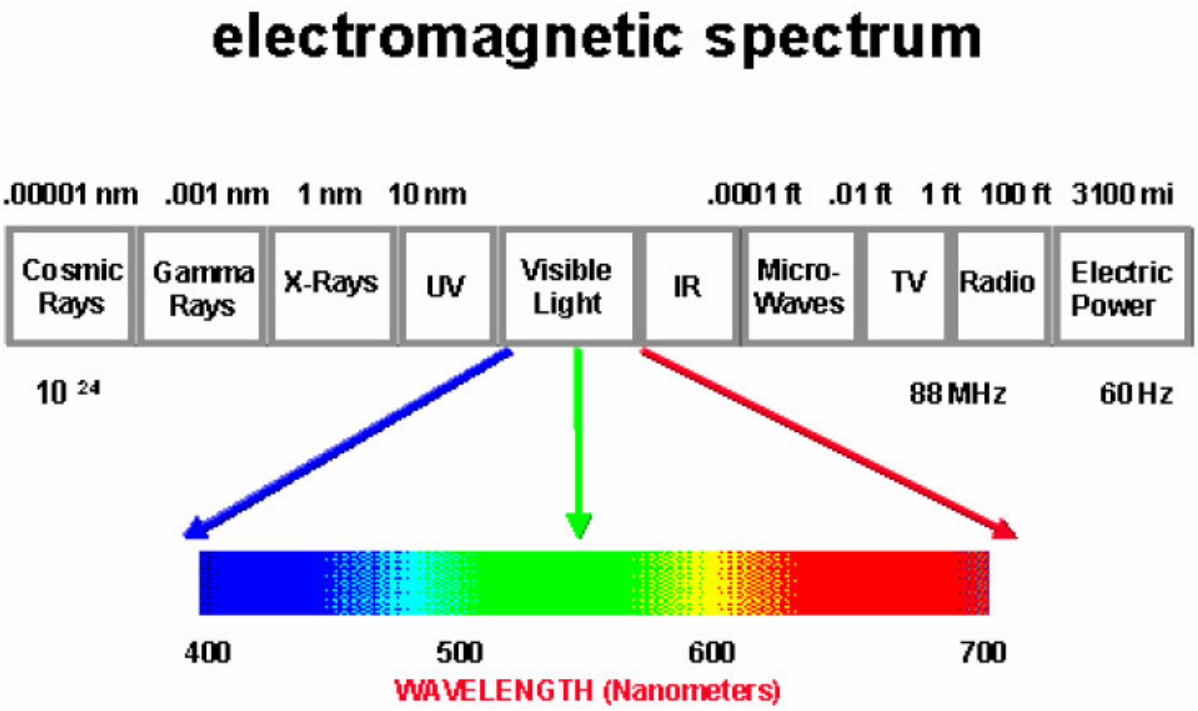

Figure 1.3: Electromagnetic spectrum (Shen 2003)

Table 1.1: Colour appearance and corresponding wavelengths (Shen 2003)

Colour Appearance	**Wavelength (nm)**
Violet	≥450
Blue	450-480
Blue-Green	480-510
Green	510-550
Yellow-Green	550-570
Yellow	570-590
Orange	590-630
Red	≤630

1.4 Colorimetric Assays

The simplest physical property of a reaction to visualize directly is perhaps by colour or to quantify using a camera or UV-Vis spectrometer. However, colour is underexploited as a molecular method for determining local sequence, structure, and base composition. Colorimetry is a favourable detection method because it involves simple apparatus that can be used for qualitative and quantitative experimental measurements. A wide array of situations where the visual, qualitative determination of colour change is the sole determinant of a colorimetric assay's results has been reported (Wyszecki and Stiles 1982; Shen 2003; Sharma 2018). Vaitukaitis reported tests for pregnancy (Vaitukaitis 2004), system for measuring pH was reported by (Myers 2009), whereas determination of soil and water components was reported by (Cenens and Schoonheydt 1988) and lastly (Maunder 1974) reported narcotics, to name a few.

Colorimetric assays have characteristically used UV-Vis spectroscopy to quantify the reflectance, transmittance, or relative irradiance of colour generated from a chromophore. These colorimetric measurements produce accurate and precise data on the intensity of reflection or transmission of a light source as a function of a specific wavelength to quantify colour change. However, spectroscopy analysis has been widely used in colorimetric assays, the technique does not typically output a numerical representation of a sample colour (Sharma, Wu and Dalal 2005).

Colour grab is a typical colour picker that is used to select and adjust colour values. It is a simple method for measuring the different colour intensities produced when colours are mixed (Montangero 2015). Colour grab version 3.6.1 is used for images or to practically measure colour variation. For solution evaluation, colours are selected *via* an interface with a visual representation of a colour pre-arranged with perception relevant to lightness and saturation of objects (Hossain *et al.* 2015). Colour appearance depends on comparison of neighbouring colours, therefore, many interfaces attempt to clarify the intensity relationship between colours prior red green blue (RGB) colour model.

The RGB colour model is used for sensing representation and display of images in an electronic system (Ford and Roberts 1998). A comparison is done between computer colour space using appropriate applications and software (i.e. ImageJ) which are based on naked eye perception (Kumar and Verma 2010). The RGB values can be used as a colour reference in the fabrication of colorimetric sensors. These RGB values produce clear colour relations to the optimised

standard ranges. RGB colour model is easy to use with the reliability to produce highly efficient colorimetric schemes. RGB measurements from metal nanoparticle colorimetric assays are used to interpret the distinguishable colour signals given by that particular metal nanoparticle in reaction solutions (Cheng *et al.* 2014).

There are numerous choices of colour-space models that can be utilized to quantify colours, including CIELAB, CMYK, RGB, HSL and XYZ, among others (Sharma, Wu and Dalal 2005). CIELAB colour space has the following advantages: i) it is simple to understand, ii) it is simple to determine result from images, iii) the data obtained through different methods can be directly compared, iv) it is the standard colour space model used in colour industries like paints and textiles, v) it is simple to calculate and compare changes in colour (*ΔE)* and vi) the colour change equations are continually being easily improved (Sharma, Wu and Dalal 2005). Colours are numerically identified by a set of 3-dimensions in the CIELAB colour space model, relating lightness (L*), red verses green (a*), and yellow verses blue (b*), which defines a colour space in Figure 1.4. In 1976 CIE created L*, a*, b* colour space. CIELAB was based on a system introduced by Richard Hunter in 1942 using L, a, b values prior to this (Sharma 2018). The L, a, b coordinates are based on a square root transformation of colour whereas L*, a*, b* coordinates are based on a cube root transformation of the colour data (Maunder 1974). Additionally, L*, a*, b* describes all colours visible to the human eye and was created to serve as a device independent model (Choudhury and Chatterjee 1996). The three components of CIELAB are L*, which is the lightness of colour (L = 0 black whereas L = 100 is white), a*, which is the position between red and green (a* negative values is green and positive values is red), and b*, which is the position between yellow and blue (b* negative values indicate blue whereas positive values indicate yellow) in Figure 1.4.

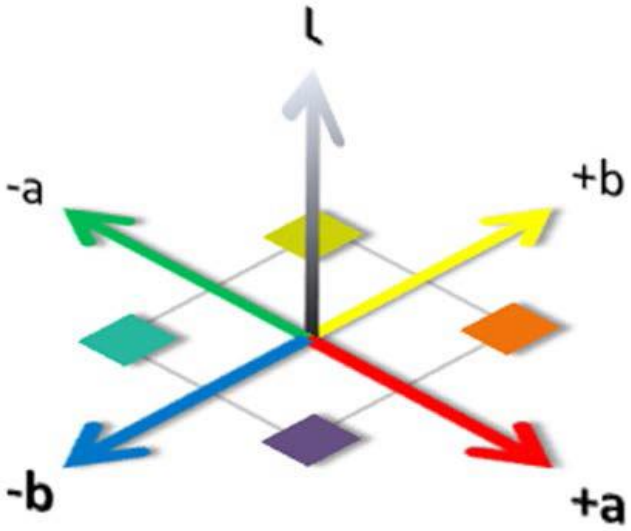

Figure 1.4: The three-dimensional colour space defined by lightness (L), red versus green (a*) and yellow versus blue (b*) (Choudhury and Chatterjee 1996).

The CMY(K) colour space are commonly used for production printer colour and has a disadvantage of the components are pigments or inks not colours. Meanwhile, the RGB colour model has the disadvantages of (i) difficult to determine specific colour, (ii) non useful for objects specification and recognition of colours and (iii) reflects the use of cathode-ray tube (CRT's) since it is hardware-oriented system. Lastly, the disadvantages of the HSL colour space are not uniform, does not supply with insight for colour manipulation and undefined chromatic hue points are sensitive to value deviation of RGB (Cenens and Schoonheydt 1988).

The International Commission on Illumination known as CIE in 1931 referred to the studied human colour perception and developed a standard that is still widely used today (Cenens and Schoonheydt 1988). The CIE colour systems utilize three coordinates to locate colour in a colour space. The spaces include: CIE XYZ, CIE L*a*b* and CIE L*C*h*. The CIE commissioned work in 1931 and 1964 to derive the concept of a standard observer, which is based on the average human response to wavelengths of light in Figure 1.5. Briefly, the standard observer represents how an average person sees colour across the visible spectrum.

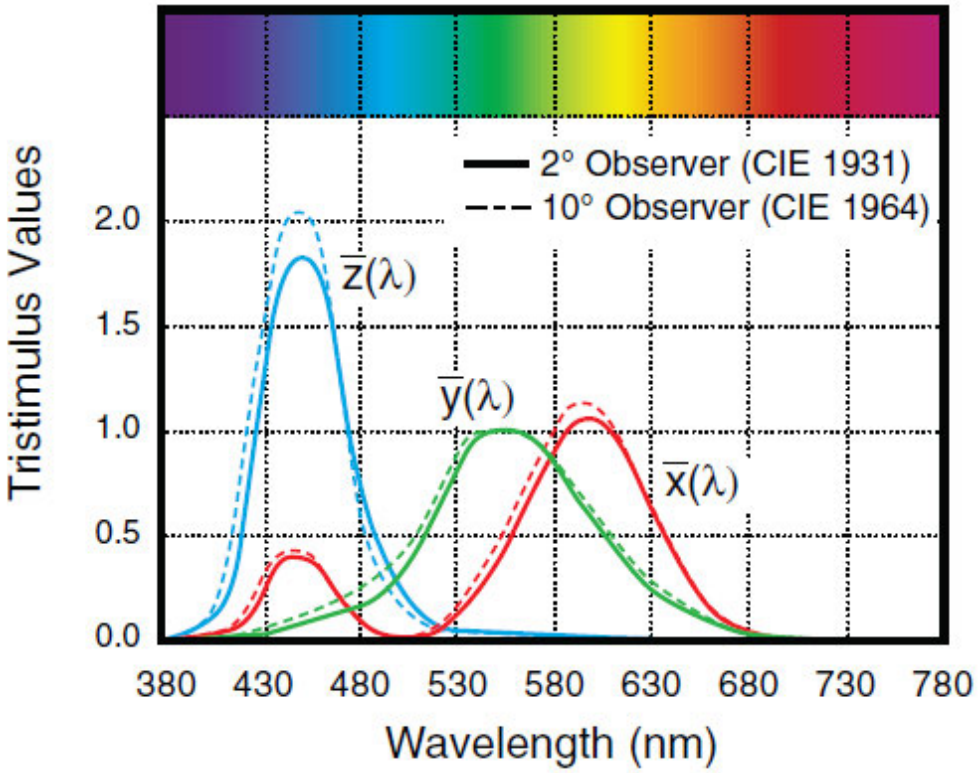

Figure 1.5: CIE 2° and 10° Standard observers (Sharma 2018)

Chromaticity values are tristimulus values, with limited use as colour specifications because they correlate poorly with visual attributes. While Y relates to value (lightness), X and Z do not correlate to hue and chroma. As a result, when the 1931 CIE standard observer was established, the commission recommended using the chromaticity coordinates xyz. These coordinates are used to form the chromaticity diagram in Figure 1.6 (a). The notation Yxy specifies colours by identifying value (Y) and the colour as viewed in the chromaticity diagram (x,y). Hue is represented at all points around the perimeter of the chromaticity diagram in Figure 1.6 (b). Chroma, or saturation, is represented by a movement from the central white (neutral) area out toward the diagram's perimeter, where 100% saturation equals pure hue.

(a) **(b)**

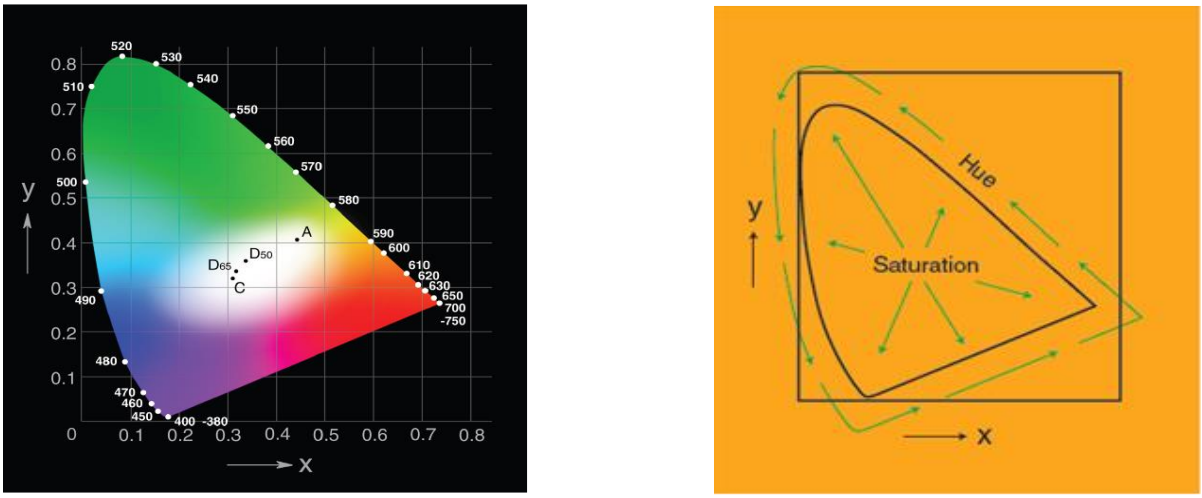

Figure 1.6: (a) CIE 1931 (x,y) chromaticity diagram and (b) Chromaticity diagram (Sharma 2018).

1.5 Problem Statement

Nowadays, chromium has been progressively used in a number of industrial processes including chrome plating, dye and pigment fabrication, leather tanning, and wood preserving and it commonly exists as Cr(III) or (VI) oxidation states (Xin *et al.* 2012). Cr(III) is an essential trace element for mammals considered to have low toxicity while Cr(VI) is approximately 100 times more toxic and is considered a human carcinogen with hostile impact on human skin, stomachs, lung, liver and kidneys (Kotaś and Stasicka 2000; Gomez and Callao 2006; Rakhunde, Deshpande and Juneja 2012; Zhang *et al.* 2013). Cr(VI) ions are abundant in the environment because of their large-scale use in various industries can even be detected in natural water. Based on the growing attention on chromium pollution, the United States Environmental Protection Agency (US-EPA) suggests that the Cr(VI) concentration in drinking water should be under 100 ppb also the World Health Organization (WHO) proposes a guideline value of 50 ppb for total chromium and 16 ppb for Cr(VI) in drinking water (Hashemi and Daryanavard 2012; Zhang *et al.* 2012; Zhang *et al.* 2013). Effluents or slags containing chromium are discharged into the environment immoderately with the global expansion of industrial factories utilizing chromium extensively in industrial processes (Guo *et al.* 2016). Due to the increasing threat of chromium exposure in the environment, there has been a growing interest in the development of highly sensitive and selective assay methods for the determination of chromium over the past few years (Xin *et al.* 2012).

Lead ion (Pb(II)) is considered a major environmental pollutant and a dangerous abundant heavy metal (Ratnarathorn, Chailapakul and Dungchai 2015). Pb(II) is a potent neurotoxin and bio-accumulative that cause potential damage to normal cellular functions, gene expression, affects signal transduction, and calcium mediated cellular processes (Milosevic and Maier 2000; Barciszewska *et al.* 2005; Yoosaf *et al.* 2007). Pb(II) is ranked second in the list of toxic substances that cause renal malfunction and damage to the brain and kidneys (Ratnarathorn, Chailapakul and Dungchai 2015). A number of anthropogenic and industrial activities such as smelting, use of pesticides, battery production, landfill leaching have significantly contributed towards Pb(II) contamination in the environment, in the last decade (Yoosaf *et al.* 2007). Food and drinking water are often contaminated with detrimental substances for humans, either as part of the production process natural or caused by the additives added to it (Priyadarshini and Pradhan 2017b). Moreover, Pb(II) has been classified as carcinogenic agents by the WHO and International Agency for Research on Cancer and the long-term exposure to low concentrations of Pb(II) causes hostile health effects. The maximum acceptable limit of Pb(II) is 0.05–0.10 mg/L in wastewater. Nevertheless, Pb(II) is becoming a major environmental concern as a 250 mg/L concentration has been reported in industrial wastewater (Sağ, Özer and Kutsal 1995). Therefore, there is a massive demand for developing a rapid assay method that would allow detection of Pb (II) ions.

Manganese ion (Mn(II)) plays an important role in the bone and other tissues formations, normal reproductive functions, carbohydrate and lipid metabolism under the normal condition and is considered as one of the essential microelements in human body (Gao *et al.* 2013). Mn(II) deficiency in human body is related to delayed blood coagulation and hypercholesterolemia. Yet, uptake of high concentration of Mn(II) is detrimental. Severe psychiatric abnormalities manifested in the form of hyperirritability, violent acts and hallucinations are signs of toxicity. A permanent crippling neurological disorder of the extrapyramidal system with morphological lesions similar to those of Parkinson disease appears as the diseases progresses (Organization 1996). Mn(II) is well known to exist in water steadily compared to other valence states of Mn. Therefore, low concentrations in samples (such as food stuffs, water and beverages) with high sensitivity and excellent selectivity has attracted much more attention to develop methods for detecting Mn(II) (Gao *et al.* 2013). Additionally, it is necessary to develop methods for detecting it at low concentrations in samples with great precision and accuracy (Zhou *et al.* 2012).

The AuNP-based colorimetric sensors capitalizes on the colour change that arises from the inter-particle plasmon coupling upon the aggregation of AuNPs (colour change from red to purple or blue) (Ly and Joo 2015; Ly, Oh and Joo 2015; Shahrivari, Faridbod and Ganjali 2018). Such phenomenon has been used by many researchers to make sensitive chemical probes for some inorganic cations (Wu, Chen and Sung 2011; Tripathy, Woo and Han 2013; Wang *et al.* 2013; Sung and Wu 2014; Zhou *et al.* 2014) and chromium ions (Cr(III and VI)) (Dang *et al.* 2009; Chen *et al.* 2013; Lo *et al.* 2015; Ly, Oh and Joo 2015; Shahrivari, Faridbod and Ganjali 2018).

Within the laboratory a diode-array instrument or a UV-Vis scanning instrument have been used traditionally for colour analysis. Diode-array instruments take a snapshot of the entire spectrum in less than one second while UV-Vis instruments typically take 20-60 second to perform the same analysis. These spectrophotometers provide necessary colour analysis but are relatively expensive and not always accessible for use outside of the laboratory setting. In contrast, other low cost techniques are available that exploit colour imaging and colour space analysis to measure subtle changes in colour that are more representative of human colour perception (Margulis 2005).

Image processing was conducted using instrument dependent RGB colour coordinates and instrument independent CIE L*a*b*/Yxy which has never been reported in literature using functionalized gold and silver nanoparticles for the colorimetric detection of Cr(VI), Pb(II) and Mn(II) ions. An extensive literature survey revealed that modified and unmodified gold and silver nanoparticles based colorimetric assays are widely used for the colorimetric detection of Cr(VI), Pb(II) and Mn(II) ions. However, in our knowledge no reports were published where they synthesized the capping ligands and employed the RGB colour coordinates and CIE L*a*b* colour space to measure the colour dynamics between the ligands, gold and silver nanoparticles. The results emanating from this work are presented in a case-study method ranging from potential papers for publication.

1.6 Motivation

This study provides the development of a simple, selective, sensitive and rapid colorimetric sensors for the detection of Cr(VI), Pb(II) and Mn(II) using functionalized gold and silver nanoparticles. Synthesis of complex ligands for the functionalization of gold and silver nanoparticles is of utmost importance as there are no studies reported in literature based on our

knowledge that reported the colorimetric detection of these heavy metals using synthesis ligands. The optical sensors developed herein presents a cost-effective tool for monitoring Cr(VI), Pb(II) and Mn(II) in environmental water samples. Due to the increasing threat of chromium exposure in the environment, there has been a growing interest in the development of highly sensitive and selective assay methods for the determination of chromium over the past few years (Xin et al. 2012). The importance of monitoring the toxic metal ions in the aquatic ecosystems remains an issue due to the hostile effects on ecological environment and human health by means of the food chain (Wang *et al.* 2015). Sensitive and selective detection of heavy metal ions in environmental waters has become crucial for controlling the quality of discharged water.

Various techniques for determination of Cr(III), Cr(VI), Pb(II) and Mn(II) have been developed over the past decades, including High-Performance Liquid Chromatography (HPLC) (Wang *et al.* 2010), Electro-Thermal Atomic Absorption Spectroscopy (ETAAS) (Chen *et al.* 2010; Zhang *et al.* 2012), ICP-MS (Guerrero *et al.* 2012), SPE (Ma, Yang and Byrne 2012), Inductively Coupled Plasma Optical Emission Spectrometry (ICP-OES) (Meeravali, Madhavi and Kumar 2011; Cheng *et al.* 2012) and AAS (Milosevic and Maier 2000; Barciszewska *et al.* 2005; Yoosaf *et al.* 2007), ICP-MS (Sağ, Özer and Kutsal 1995; Priyadarshini and Pradhan 2017b), ICP-AES (Yu *et al.* 2017), and XRF spectrometry(Liu, Jiang and Liu 1999). However, these methods involve sample pre-treatment procedures, are time consuming and can only directly detect one valence state. Additionally, instruments such as ICP-OES and ICP-MS are bulky and expensive with high operating cost. Therefore, developing simple methods for selective and sensitive determination of Cr(III) and Cr(VI) is still a great challenge (Zhang *et al.* 2013). The development of a simple and practical method for the determination of Cr(VI) is of significant importance (Guo *et al.* 2016). While, these methods can detect Pb(II) sensitively and accurately, but there are limits in their complicated sample preparation processes, expensive, and required any specialized as well as sophisticated instrumentation (Ratnarathorn, Chailapakul and Dungchai 2015). (Chai *et al.*) reported a viable colorimetric detection of Pb(II) ions using glutathione conjugated AuNPs showing a MDL of 100 nM (Chai *et al.* 2010; Priyadarshini and Pradhan 2017a). High affinity of GSH to bind to Pb(II) ions was suggested by a negative result yielded by a control sets treated with other metal cations. Moreover, many dynamic methods have been reported for Mn(II) determination based on its catalytic effect on the oxidation of organic compounds. Although some of these methods have

extremely low detection limitation, most of them lack sufficient sensitivity for detecting Mn(II) and are cockamamie or uneconomical (Mutaftchiev 2001; Wei *et al.* 2003; Gao *et al.* 2013).

1.7 Aim and Objectives

This project is based on the development of CIELAB colour system for the detection of Cr(VI), Pb(II) and Mn(II) using functionalized gold and silver nanoparticles.

Objectives are:

- To synthesize citrate capped AuNPs and AgNPs optical enabled sensors.
- To synthesize 3-(p-tolyl)-2,3-dihydropyrazolo[3,4-b] indole-1(4H)-carbothioamide (TRPIDA_CH_3) complex, 1-methyl-6-phenyl-6, 7-dihydro-5H-indolo [3, 2-c] [1, 8] naphthyridine (TRPIDB_H) complex and 3-(4-hydroxy-3-methoxyphenyl)-2, 3-dihydropyrazolo [3, 4-b] indole-1(4H)-carbothioamide (TRPIDA_V) complex.
- To characterize citrate capped AuNPs and AgNPs using UV-Vis, TEM and DLS.
- To characterize fully the synthesized TRPIDA_CH_3, TRPIDB_H and TRPIDA_V complexes using FT-IR, ^{1}H and ^{13}C NMR, TOF-MS and elemental analysis.
- To fabricate the AuNPs with TRPIDA_CH_3, DPC and TRPIDA_V complexes for the selective detection of Cr(VI) and Mn(II), respectively.
- To fabricate AgNPs with TRPIDB_H complex for the selective detection of Pb(II).
- To optimize RGB colour coordinates and CIE L*a*b*/Yxy colour system using Cr(VI), Pb(II) and Mn(II) standard solutions.
- To quantify Cr(VI) in wastewater effluent using TRPIDA_CH_3 functionalized AuNPs spectrophotometrically and optimized RGB colour coordinates and CIE L*a*b*/Yxy colour system.
- To spectrophotometrically analyse the DPC-AuNPs and image processing of Cr(VI) standard solutions.
- To analyse intensity of colours using a smartphone.
- To study computationally, the adsorption of Cr(VI) on the surface of DPC-AuNPs.

1.8 Research Hypothesis

This study is aimed at presenting the development of affordable, sensitive, specific, user-friendly, reliable and instrument free colorimetric assays to detect heavy metals in

environmental water samples using functionalized metal nanoparticles. The presence of these environmental pollutants poses a great threat to humans and the development of highly selective and sensitive colorimetric methods poses a challenge. Synthesis of complex ligands for the modification of AuNPs and AgNPs is important and according to our knowledge no studies have been reported in literature. The developed optical enabled colorimetric sensors are a suitable alternative quantification tool for detecting trace levels of Cr(VI), Pb(II) and Mn(II).

1.9 Thesis Outline

The outcome of this research study is outlined in seven chapters as presented below:

Chapter 1 provides a detailed general introductory background information, problem statement, motivation, aims and objectives of this study.

Chapter 2 reports an in-depth literature review of the metal nanoparticles preparation, functionalization of metal nanoparticles, detection of heavy metals using functionalized AuNPs, colorimetric detection of target metals and reports on limits of detection and quantification of target metals which are namely: Cr(VI), Pb(II) and Mn(II).

Chapter 3 describes the chemicals and reagents used in this study. Additionally, the experimental methodologies for all studies are also reported which are the synthesis of the citrate capped AuNPs and AgNPs, synthesis of TRPIDA_CH_3, TRPIDB_H, and TRPIDA_V complexes, characterization of functionalization ligand complexes and the functionalization of citrate capped AuNPs and AgNPs. Furthermore, preparation of metal ion standard solutions and their treatment with AuNPs and AgNPs and selectivity studies are described. The experimental and computational methodologies for all the case studies are also defined.

Chapter 4 – Case Study I – results of the synthesis and characterization of 3-(p-tolyl)-2,3-dihydropyrazolo [3,4-b] indole-1 (4H)-carbothioamide functionalized gold nanoparticles for the CIE L*a*b*/Yxy colorimetric detection of Cr(VI) are presented and discussed in this chapter.

Chapter 5 – Case Study II – this chapter discusses the results of the development of a smartphone and spectrophotometric based systems for colorimetric detection of Cr(VI) using 1,5-diphenylcarbazide functionalized gold nanoparticles supported by CIE L*a*b*/Yxy colour space and molecular dynamics.

Chapter 6 – Case Study III – this chapter elaborates the results of understanding interaction between 1-methyl-6-phenyl-6, 7-dihydro-5H-indolo [3, 2-c] [1, 8] naphthyridine complex with silver nanoparticles and Pb(II): a CIE Lab/Yxy and RGB colour coordinates study.

Chapter 7 – Case Study III – the colorimetric detection of Mn(II) using 3-(4-hydroxy-3-methoxyphenyl)-2, 3-dihydropyrazolo [3, 4-b] indole-1(4H)-carbothioamide capped gold nanoparticles: A CIE L*a*b*/Yxy colour space study results and discussion are presented in this chapter.

Chapter 8- Conclusions- this chapter discussed the conclusions based on the work conducted for this dissertation.

CHAPTER TWO

2.0 LITERATURE REVIEW

2.1 Heavy metals of interest

Effluents or slags containing chromium are discharged into the environment immoderately with the global expansion of industrial factories utilizing chromium extensively in industrial processes (Guo *et al.* 2016). Due to the increasing threat of chromium exposure in the environment, there has been a growing interest in the development of highly sensitive and selective assay methods for the determination of chromium over the past few years (Xin *et al*. 2012). The importance of monitoring the toxic metal ions in the aquatic ecosystems remains an issue due to the hostile effects on ecological environment and human health by means of the food chain (Wang *et al.* 2015). Sensitive and selective detection of heavy metal ions in environmental waters has become crucial for controlling the quality of discharged water. Chromium has been increasingly used in a number of industrial processes nowadays including chrome plating, dye and pigment fabrication, leather tanning, and wood preserving and it commonly exists in chromium(III) and (VI) oxidation states (Xin *et al.* 2012).

Various strategies have been reported previously to detect Cr(VI), those reports include methods based on large equipment's such as Inductively Coupled Plasma Mass Spectrometry (ICP-MS) (Wen, Shan and Lian 2002), Atomic Absorption Spectroscopy (AAS) (Chwastowska *et al.* 2005), X-ray Fluorescence (XRF) and Solid Phase Extraction (SPE) (Tsuyumoto and Maruyama 2011; Ma, Yang and Byrne 2012). Additionally, those large equipment-based methods usually have superior accuracy and stability. However, they usually suffer from disadvantages such as sophisticated pre-treatment, requirement of professional operation and also high cost, which render them unsuitable for real-time field monitoring. While, colorimetric assay based on metal nanoparticles have attracted increasing attentions in recent years because they require no complex instrumentations and signal recognition can be achieved by just naked eye in the form of colour change (Chen *et al.* 2015; Ratnarathorn, Chailapakul and Dungchai 2015; Wang *et al.* 2015).

Gold nanoparticles (AuNPs) are those of particular interest, as they have strong surface plasmon resonance (SPR) absorption with extremely high extinction coefficients (10^8–10^{10} M^{-1} cm^{-1}) in the visible region (Guo *et al.* 2016). Various techniques for determination of Cr(III) and Cr(VI) have been developed over the past decades, including High-Performance Liquid Chromatography (HPLC) (Wang *et al.* 2010), Electro-Thermal Atomic Absorption Spectroscopy (ETAAS) (Chen *et al.* 2010; Zhang *et al.* 2012), ICP-MS (Guerrero *et al.* 2012), SPE (Ma, Yang and Byrne 2012) and Inductively Coupled Plasma Optical Emission Spectrometry (ICP-OES) (Meeravali, Madhavi and Kumar 2011; Cheng *et al.* 2012). However, these methods involve sample pre-treatment procedures, are time consuming and can only directly detect one valence state. Additionally, instruments such as ICP-OES and ICP-MS are bulky and expensive with high operating cost. Therefore, developing simple methods for selective and sensitive determination of Cr(III) and Cr(VI) is still a great challenge (Zhang *et al.* 2013). The development of a simple and practical method for the determination of Cr (VI) is of significant importance (Guo *et al.* 2016).

Even a low concentration of Cr(VI) exposure might generally cause haemolysis, renal and liver failure and even various types of cancer (Guo *et al.* 2016). Cr(III) is a vital mineral which has been shown to lower oxidative stress, maintaining normal physiological function and improves metabolism by activating certain enzymes (Guo *et al.* 2016; Shaikh *et al.* 2017). Trivalent chromium ion, Cr(III), is considered an essential transition metal ion that regulates insulin action on the control of blood sugar in humans (Lo *et al.* 2015; Guo *et al.* 2016; Shaikh *et al.* 2017). Deficiency of chromium has been linked to insulin resistance or glucose intolerance. However, overload of chromium ion would induce oxidative damage to some cellular components, such as lipids, proteins, and Deoxyribonucleic Acid (DNA) (Lo *et al.* 2015; Guo *et al.* 2016). Unfortunately, Cr(VI) is widely distributed in wastewater all over the world, which was a persistent great threat to the environment and human health (Dang *et al.* 2009; Lo *et al.* 2015). Cr(VI) may be easily reduced to Cr(III) with the formation of reactive free radicals within the cell, leading to the inhibition of the metallo-enzyme system (Kotaś and Stasicka 2000; Jin, Wu and Chen 2014). Furthermore, Cr(VI) compounds are highly soluble and mobile in both biological and natural ambient systems (Lee and El-Sayed 2006). As specified by World Health Organization (WHO), US Environmental Protection Agency (EPA) standard and European Community (EC), the MAL (maximum allowable level) of Cr(III) in drinking water are 50 μg/L, 100 μg/L, and 50 μg/L, respectively (Chen *et al.* 2014; Shiraishi *et al.* 2017). The

two oxidation states, Cr(VI) and Cr(III) are exchangeable. Thus, there is a pressing need to explore an accurate and reliable method for the detection and monitor of chromium ions.

Numerous methods have been used for the detection of Pb(II) such as AAS (Milosevic and Maier 2000; Barciszewska *et al.* 2005; Yoosaf *et al.* 2007), ICP-MS (Sağ, Özer and Kutsal 1995; Priyadarshini and Pradhan 2017b), ICP-AES (Yu *et al.* 2017), electrochemical method (Jian-feng *et al.* 2016) and XRF spectrometry(Liu, Jiang and Liu 1999). While, these methods can detect Pb(II) sensitively and accurately, but there are limits in their complicated sample preparation processes, expensive, and required any specialized as well as sophisticated instrumentation (Ratnarathorn, Chailapakul and Dungchai 2015). (Chai *et al.* 2010) reported a viable colorimetric detection of Pb(II) ions using glutathione conjugated AuNPs showing a MDL of 100 nM (Chai *et al.* 2010; Priyadarshini and Pradhan 2017a). High affinity of GSH to bind to Pb(II) ions was suggested by a negative result yielded by a control sets treated with other metal cations.

In recent years, various methods have been reported for Mn(II) detection, including atomic absorption spectrometry (AAS) (Nascentes *et al.* 2005), inductively coupled plasma mass spectroscopy (ICP-MS) (Beauchemin and Berman 1989), and inductively coupled plasma-atomic emission spectrometry (ICP-AES) (Dahlquist and Knoll 1978). However, these methods need costly instruments or complicated procedures, making them inconvenient and time consuming. Moreover, many dynamic methods have been reported for Mn(II) determination based on its catalytic effect on the oxidation of organic compounds. Although some of these methods have extremely low detection limitation, most of them lack sufficient sensitivity for detecting Mn(II) and are cockamamie or uneconomical (Mutaftchiev 2001; Wei *et al.* 2003; Gao *et al.* 2013). Recently, many colorimetric assay methods have been reported for detection of heavy metal ions based on gold or silver nanoparticles due to their high extinction coefficient and strong surface plasmon resonance properties (Boisselier and Astruc 2009; Tolaymat *et al.* 2010; Liu, Wang and Jiang 2011; Gao *et al.* 2013). Various methods for the determination of manganese have been reported, including electron spectroscopy (Zaw and Chiswell 1999). Diphenylphosphine (DPP) (Luther III, Nuzzio and Wu 1994), chemical modifer-Electrothermal Atomic Absorption Spectrometry (ETAAS) (Zhou *et al.* 2012) and crosslinked chitosan-Flame Atomic Absorption Spectrometry (FAAS) (Kargosha and Noroozifar 2000). (Soto-Neira, Zhu and Aller) proposed a spectrophotometric method to quantify dissolved manganese in marine pore waters, using Cadmium(II) meso-Tetrakis(4-

sulfophenyl)porphyrin (Cd-TSPP) complex as an indicator (Soto-Neira, Zhu and Aller 2011). However, most of these techniques need costly instruments or complex procedures, making them in convenient and time-consuming (Zhou *et al.* 2012).

Pyrazoles are five-membered aromatic heterocycles containing two nitrogen atoms adjacent to each other. This skeleton is an important template for designing and developing diverse therapeutic drugs (Kale, Pawar and Kale 2016; Makhanya 2019) since they display several biological properties such as analgesic, antipyretic, anti-hyperglycemic, anti-inflammatory, antibacterial, hypoglycemic and sedative-hypnotic activities (Dadiboyena and Nefzi 2011; Makhanya 2019). While pyrazoles are available from natural sources, the synthetic molecules dominate the pharmaceutical industry because they can be synthesized from simple substrates although different methodologies are described. Obtaining pyrazoles from living organisms poses a problem because of their limited ability to metabolize molecules which possess two nitrogen atoms next to each other (Makhanya 2019). Researchers are focusing on increasing the library of pyrazoles due to the lack of sufficient natural products by designing new synthetic routes to produce novel molecules which have potential bio-activity (Kumar *et al.* 2013; Tewari *et al.* 2014; Makhanya 2019). The chemistry of fused pyrazoles have attracted massive attention because of their pharmacological significance in treating various health issues.

2.2 Gold and Silver Nanoparticles as an optical sensor for

2.2.1 Chromium

Although a number of analytical methods support chromium ions estimation, recently AuNPs based colorimetric sensors have been widely investigated for the detection of chromium in real environmental samples. The basis of these sensors is formed by the chromium induced cross-linking of functionalized AuNPs or chelation reaction. (Zhao *et al.* 2012) reported the development a highly sensitive probe for Cr(III) ions based on a chelation reaction. The AuNPs functionalized with dithiocarbamate-modified N-benzyl-4-(pyridin-4-ylmethyl) aniline (BP-DTC) ligand was used in their study. The ligand molecule binds to AuNPs *via* carbodithioate (CS_2) group while the free pyridine group of ligand binds to Cr(III) ions. In these assay methods, the introduction of ligands onto the surfaces of AuNPs not only stabilize AuNPs in solution, but also can interact with metal ions through a coordination reaction. Furthermore, analyte-triggered aggregation of these functionalized AuNPs leads to a red shift in the SPR absorption band resulting in a red-to-gray colour change. Above all, the distance-dependent

SPR absorption of AuNPs has become a useful tool for the development of colorimetric sensing with various analytes (Xin *et al.* 2012). Table 2.1 shows the preparation of gold nanoparticles by the Turkevich method. Functionalization is the process of modifying the surface of metal NPs. The use of AuNPs and AgNPs as colorimetric probes requires a modification step where they are conjugated with target specific ligand molecules that facilitate specific binding to the target analyte of interest. The metal NPs surface are conjugated with functionalizing molecule such that it chemically anchors to surface while the other end remains free. The free functional groups of the molecule can thus bind to or interact with the target molecule of interest (Priyadarshini and Pradhan 2017a).

2.2.2 Lead

A report by (Kim *et al.*) employed mercaptoundecanoic acid (MUA) functionalized AuNPs as an effective colorimetric probe to detect Pb (II) ions. They established that the Pb(II) ions bind to the free acidic groups of MUA resulting in aggregation and change in colour of assay solution from red to blue (Kim *et al.* 2017). A red shift in SPR peak with decreasing intensity was observed with increasing Pb(II) ion concentration. Additionally, they proposed the reaction was reversible since the addition of EDTA resulted in chelation of Pb(II) ions and successive disassembly of AuNPs and restoration of original red colour of AuNPs (Ratnarathorn, Chailapakul and Dungchai 2015). The Minimum detection limit (MDL) of the assay was 0.5 µg/L by naked eye and was also used for Pb(II) detection in real water samples (Wei *et al.* 2003). An observation was made that the AuNPs aggregates formed by hydrogen bonds between carboxylic acid residues in methanol/water system get disrupted in presence of Pb(II) ions leading to electronic repulsion among AuNPs which results in colour change from initial blue to red (Wang *et al.* 2013). Another unique feature of the sensor was ease of varying the detection range and hence allows accurate quantification of analytes. (Wang, Lee and Lu 2008; Wei *et al.* 2008) studied the fact that single-stranded Deoxyribonucleic Acid (ssDNA) can bind to and efficiently stabilize citrate capped AuNPs while anti-double stranded Deoxyribonucleic Acid (dsDNA) could not. They used a high specific Deoxyribozyme (DNAzyme) containing eight bases substrate strand at 5'end and eight complimentary bases at the 3' end that constituted the enzyme strand. In presence of Pb (II) ion, cleavage of the hybridized complimentary strand occurs resulting in release of single-stranded Deoxyribonucleic Acid (ssDNA) strands. The generated single-stranded Deoxyribonucleic Acid (ssDNA) strands bind to AuNP surface stabilizing them. Though, in absence of Pb(II) ions cleavage does not occur

leading to destabilization and aggregation of AuNPs and resultant change in colour from red to purple to blue colour (Wang, Lee and Lu 2008). On the contrary, (Wei *et al.* 2008)carried out substrate specific cleavage by 17E Deoxyribozyme (DNAzyme) leading to release of single-stranded Deoxyribonucleic Acid (ssDNA) which attach to AuNP surface preventing their aggregation in a high salt concentration. In absence of Pb(II) ion, anti-double stranded Deoxyribonucleic Acid (dsDNA) structure formed cannot stabilize AuNPs leading to aggregation and change in colour from red to blue. The results therefore suggest that the biochemistry of Deoxyribozyme (DNAzyme) structure and nanoparticle size play an integral role in development of a superior quality colorimetric sensor.

2.2.3 Manganese

Colorimetric sensors have attracted increasing consideration for their convenience of visual observation and simple operations in recent years (Luther III, Nuzzio and Wu 1994; Cao *et al.* 2005; Zhou *et al.* 2012). Compared with other assays, they allow direct and on-site analysis of the samples with the naked eye. Among colorimetric sensors, silver nanoparticles-based colorimetric sensors have many advantages over gold nanoparticles-based ones, such as higher extinction coefficients and lower prices, allowing detection with minimal material consumption (Lee and El-Sayed 2006). A small number of researchers have been starting to explore Mn(II) detection method based on gold or silver nanoparticles (Huang *et al.* 2007). However, some of them used organic reagents as the functional selective reagents, which are instability and easily oxidized. (Zhou *et al.*) proposed a new facile and rapid colorimetric detection method of Mn(II) with high sensitivity and excellent selectivity using tripolyphosphate stabilized silver nanoparticles ($P_3O_{10}^{5-}$–AgNPs) (Zhou *et al.* 2012). The sodium polyphosphate is inorganic reagent which is stability, non-toxic and biocompatible. The $P_3O_{10}^{5-}$–AgNPs aggregate quickly in the presence of Mn(II), which leads to colour change of the nanoparticle dispersion from yellow to reddish brown and decrease of the surface plasmon absorption intensity. The Mn(II) is attracted to the surrounding of $P_3O_{10}^{5-}$–AgNPs via the electrostatic interaction and then can form a six-coordinated structure with $P_3O_{10}^{5-}$ coating on the AgNPs, which leads to formation of large particles aggregation. Due to the aggregation mechanism, this $P_3O_{10}^{5-}$–AgNPs detection system is very sensitive for Mn(II) detection (Gao *et al.* 2013). (Ratnarathorn, Chailapakul and Dungchai) reported AgNPs modified with 4-mercaptobenzoic acid and melamine as selective colorimetric sensors for Mn(II). Seemingly, both –SH of 4-Mercaptobenzoicacid and $–NH_2$ of melamine can interact with AgNPs and the

–COOH group of 4-Mercaptobenzoicacid and $–NH_2$ of melamine were modified on the surface of AgNPs together as a result. Both 4-MBA and MA have been reported to have strong affinity to metal ions (Ratnarathorn, Chailapakul and Dungchai 2015).

Table 2.1 shows chromium, lead and manganese sensing based on gold and silver nanoparticles aggregation functionalized with different capping ligands. However, the process of functionalization is associated with disadvantages of protracted and costly two-step procedure of synthesis and conjugation of target specific ligand molecule which sometimes affects the inherent reactivity of metal nanoparticles. Furthermore, AuNPs synthesized by the classical Turkevich citrate reduction method show a high affinity for positively charged metal ions as the AuNP surface is negatively charged because of the citrate molecule.

Table 2.1: Showing the preparation of AuNPs by Turkevich method

Capping Ligand	Preparation	Reference
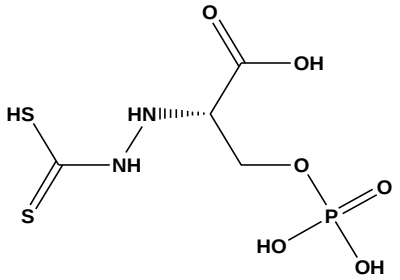 O-phospho-L-serinedithiocarbamic acid	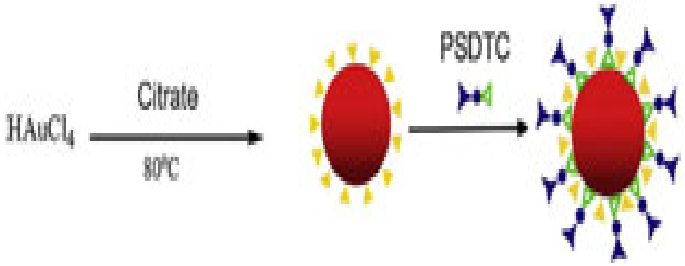	(Lo *et al.* 2015)
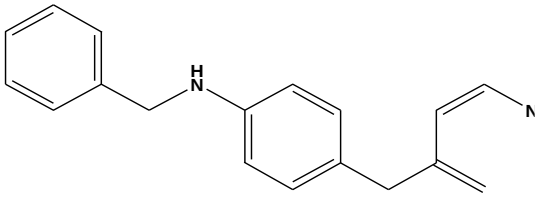 N-benzyl-4-(pyridin-4-ylmethyl)aniline	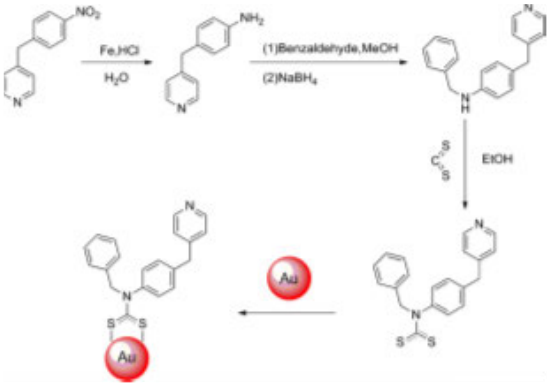	(Zhao *et al.* 2012)
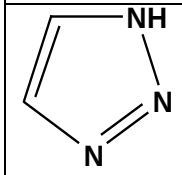 triazole	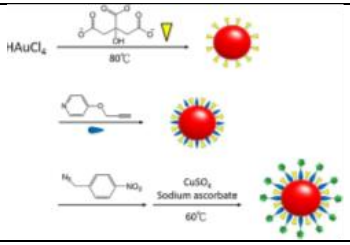	(Chen *et al.* 2013)

Table 2.2: Showing chromium, lead and manganese sensing based on AuNPs aggregation using different capping ligands.

Capping ligand	Aggregation	References
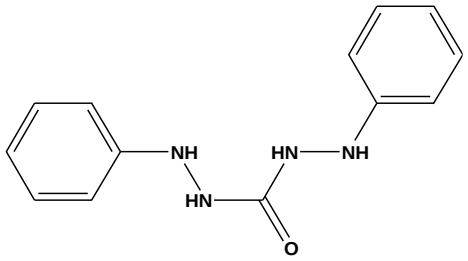 1,5-diphenylcarbazide	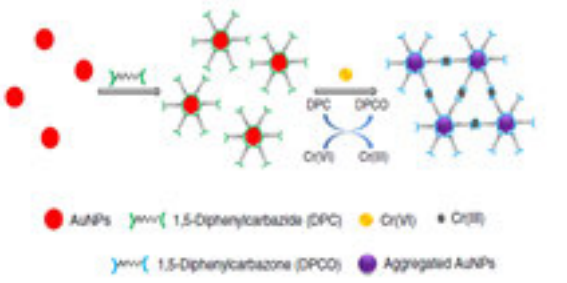	(Liu, Leng and Lin 2016)
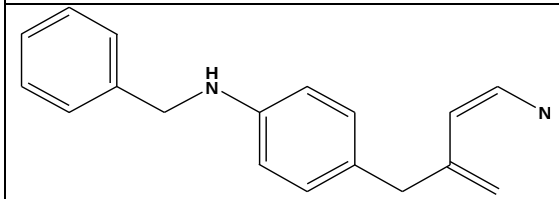 N-benzyl-4-(pyridin-4-ylmethyl)aniline	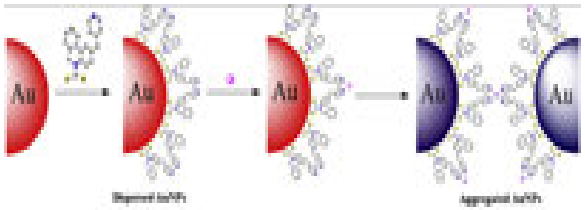	(Zhao *et al.* 2012)
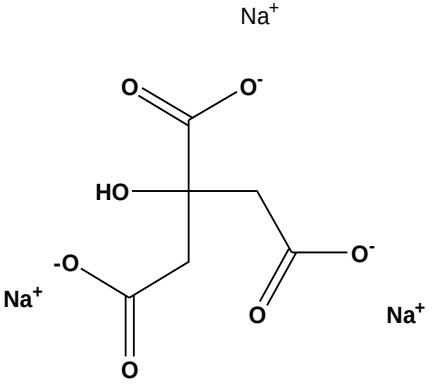 sodium citrate	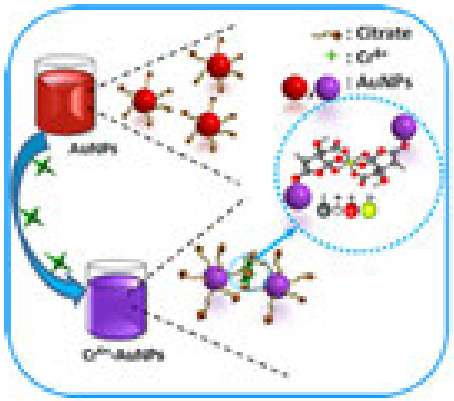	(Kanagaraj *et al.* 2017)

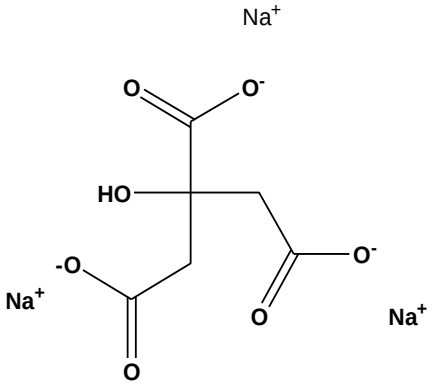 **sodium citrate**	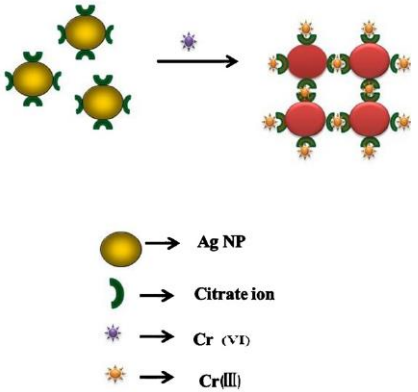	(Ravindran *et al.* 2012)
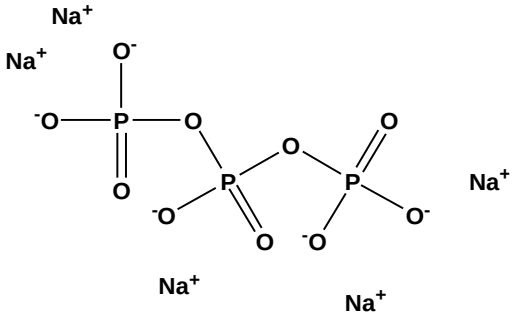 **sodium triphosphate**	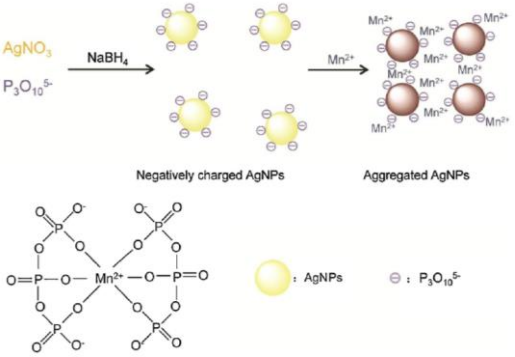	(Gao *et al.* 2013)
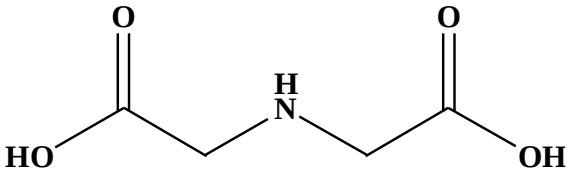 **iminodiacetic acid**	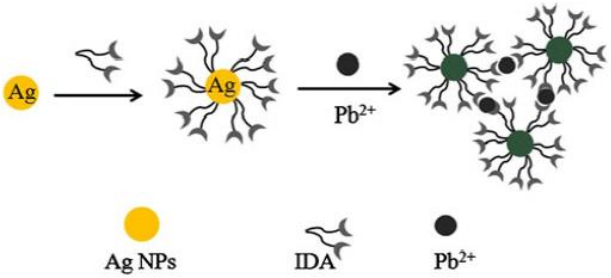	(Qi, Shang and Wu 2012)

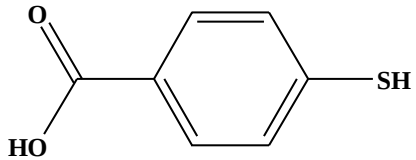 **4-mercaptobenzoic acid** and 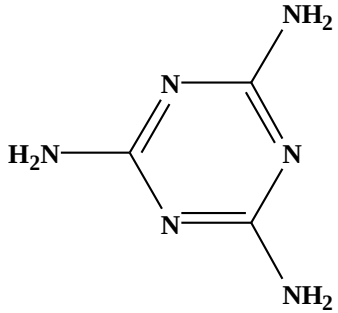 **melamine**	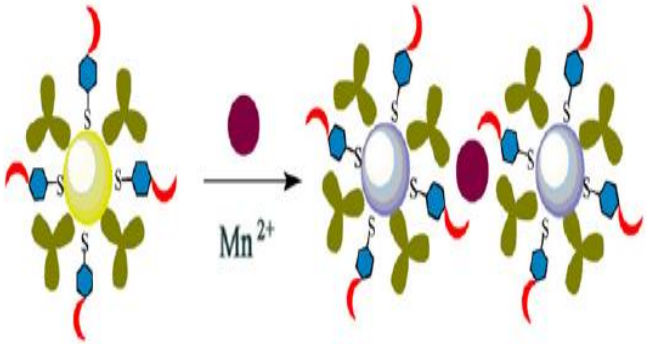	(Zhou *et al.* 2012)
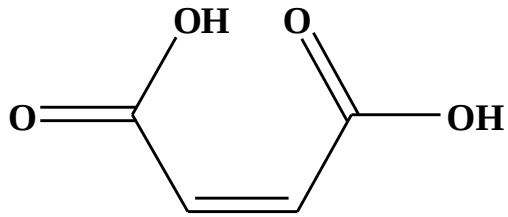 **maleic acid**	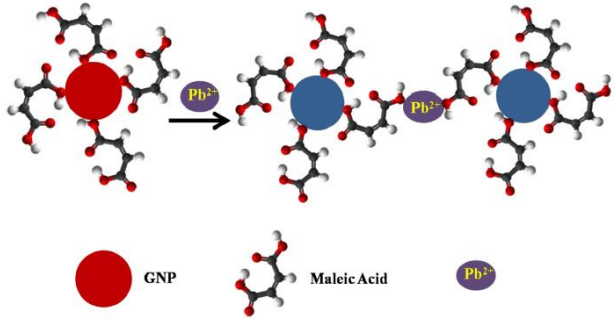	(Ratnarathorn, Chailapakul and Dungchai 2015)

2.3 Detection of chromium using functionalized AuNPs

Photographs images of chromium, lead and manganese standards previously reported in literature were analysed using ImageJ software (National Institute of Health USA, http://imagej.nih.gov./ij) as shown in Table 2.3. The pictures were processed by firstly eliminating the background light effect to highlight the actual colours of solutions. The RGB values output were measured for each colour and recorded. The RGB values were then transferred into the "More fill" colour tab on the computer for further processing. Image processing was done in triplicate for mean RGB values. The RGB colour model values for each photograph were converted to L, a* and b* (Yxy) values using website conversions (http://colormine.org/convert/rgb-to-hunterlab). The obtained L, a* and b* values were then used to calculate the colour difference *(*ΔE*),* hue angle and chroma using the following equations.

$$\Delta E = \sqrt{(\Delta L)^2 + (\Delta a)^2 + (\Delta b)^2} \qquad \text{Equation 2-1}$$

where: ΔL is the difference in lightness/darkness value, Δa is the difference on the red/green axis and Δb is the difference of the yellow/blue axis. Colour differences based on *(*ΔE*)* calculations for a standard observer can be quantified as follows, when:

- $0 < \Delta E < 1$ - observer does not notice the difference,
- $1 < \Delta E < 2$ - only experienced observer can notice the difference,
- $2 < \Delta E < 3{:}5$ - unexperienced observer also notices the difference,
- $3{:}5 < \Delta E < 5$ - clear difference in colour is noticed,
- $5 < \Delta E$ - observer notices two different colours.

chroma: $C^* = \sqrt{(a^*)^2 + (b^*)^2}$ Equation 2-2

Chromaticity increases as a colour becomes more intense and decreases as colour becomes dull. Chroma is the vividness or saturation of colour.

hue angle: $h = tan^{-1}(\frac{b^*}{a^*})$ Equation 2-3

Hue angle is the basic unit of colour. Hue is represented by the angle around the vertical axis, with starting red at 0º, then yellow, green, cyan, blue, and magenta respectively, each interval is 60º. Any two colours with 180º difference are complementary colours.

In graph (a) it was observed that the DPC-AuNPs dispersion turned from wine red to gray upon the addition of 10 and 20 µM Cr(VI) standard solution. Meanwhile, the colour difference graph (a) red line increased as the Cr(VI) standards concentration increased and the hue angle graph (a) blue line increased from the blank to 1 µM followed by a rapid decrease from 5-10 µM. Chroma increased from 0.5-5 µM then decreased from 5-10 µM. In Photograph image (b) the synthesized colloidal AgNPs were yellow in colour. However, upon interaction with Cr(VI) standard solution the particles immediately aggregated with an intense colour change from yellow to purple as shown in Photograph image (b). A rapid decrease in colour difference graph (b) red line of AgNPs in the presence of Cr(VI) was observed from (1×10^{-3})-(1×10^{-9}) M, a significant decrease in hue angle graph (b) blue line was observed as the Cr(VI) concentration increased followed by an increase from (1×10^{-5})-(1×10^{-9}) and no significant trend was observed in chroma graph (a). Silver nanoparticles functionalized with iminodiacetic acid (IDA-AgNPs) in photograph (c) changed colour from yellow to green on exposure to Pb(II) which was assumed to result from the aggregation of IDA-AgNPs induced by Pb(II). The colour difference increased as the Pb(II) concentration increased in graph (c) red line, a significant increase was observed in hue angle 6×10^{-6} M Pb(II) in blue line and chroma decreased significantly as the Pb(II) concentration increased. In photograph image (d) silver nanoparticles functionalized with tripolyphosphate ($P_3O_{10}^{5-}$-AgNPs) aggregated in the presence of Mn(II) which led to colour change from yellow to reddish brown. The colour difference red line increased significantly in as the Mn(II) concentration increased, no significant trend was observed in hue angle blue line and a rapid decrease in chroma was observed from 0.5-20 µM. In Photograph image (e) silver nanoparticles co-functionalized with 4-mercaptobenzoic acid (4-MBA) and melamine (MA) (4-MBA-MA-AgNPs) aggregated in the presence of Mn(II) through cooperative metal-ligand interaction resulting in colour change from bright yellow to purple. The colour difference red line increased significantly in as the Mn(II) concentration increased, no significant trend was observed in hue angle blue line and a rapid decrease in chroma was observed from (5×10^{-6})-(2.5×10^{-6}) M.

Table 2.3: Showing the image analysis of standard solutions for the detection of Cr(VI), Pb(II) and Mn(II).

Photograph images	**References**	**Image analysis**	
		ΔE and hue vs concentration graphs	**Chroma vs concentration graphs**
(a) 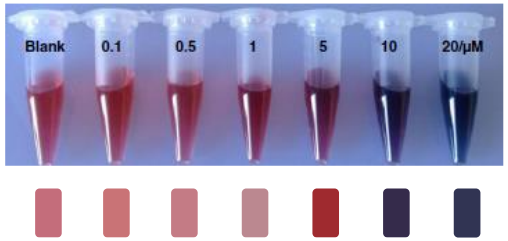	(Liu, Leng and Lin 2016)	(a) 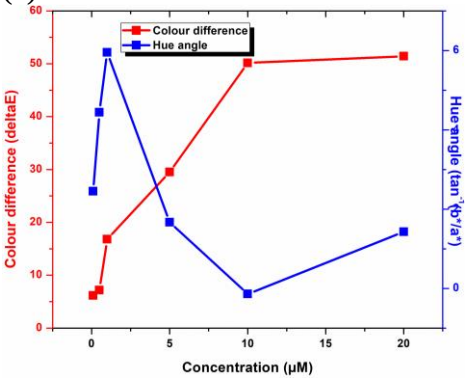	(a) 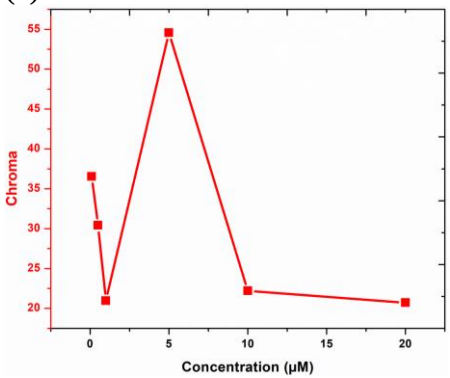
(b) 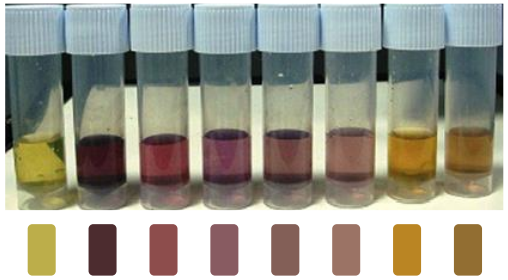	(Ravindran *et al.* 2012)	(b) 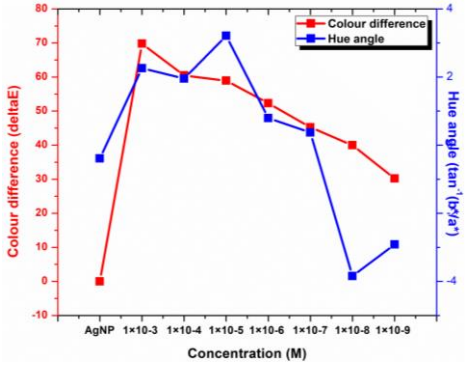	(b) 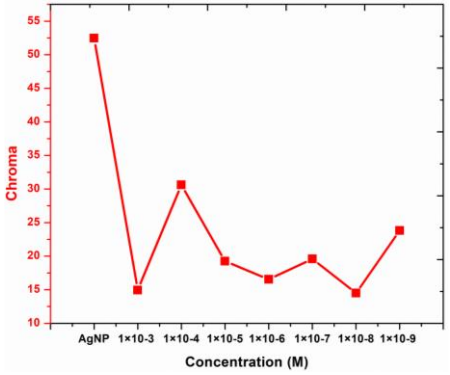

(c) 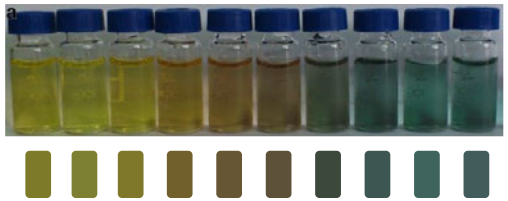	(Qi, Shang and Wu 2012)	(c) 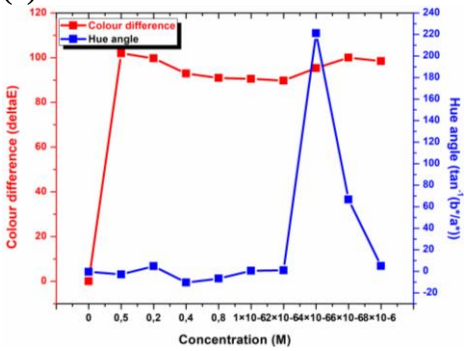	(c) 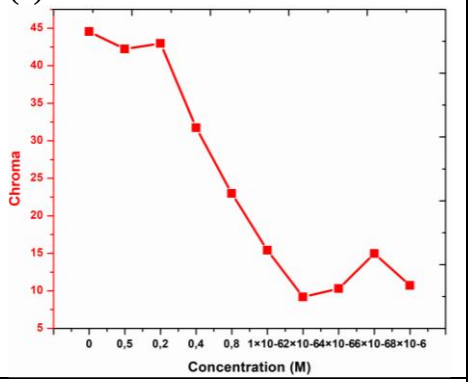
(d) 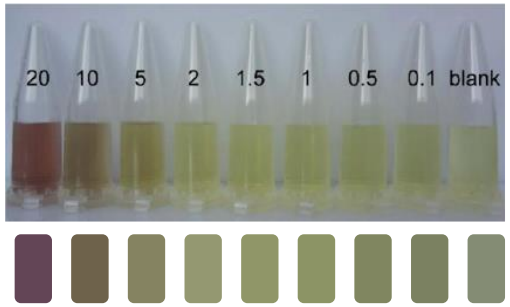	(Gao *et al.* 2013)	(d) 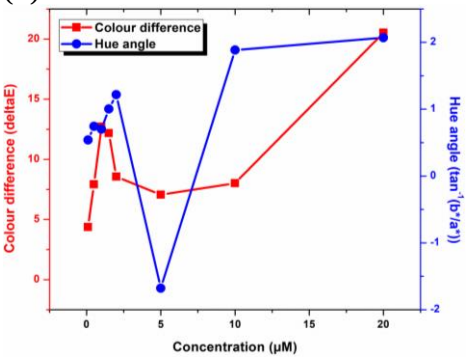	(d) 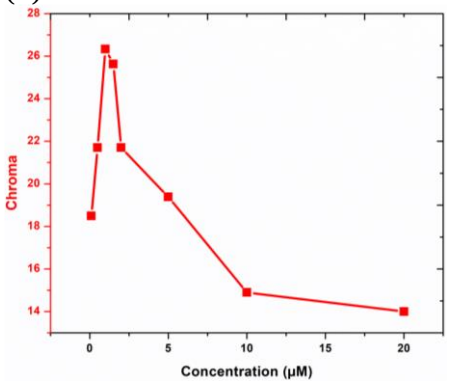

(e) 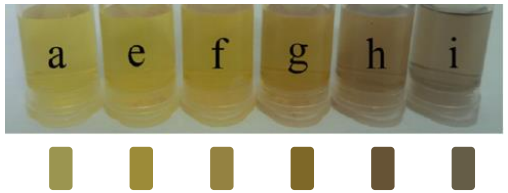 	(Zhou *et al.* 2012)	(e) 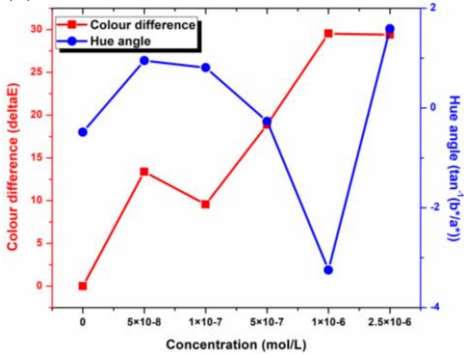 	(e) 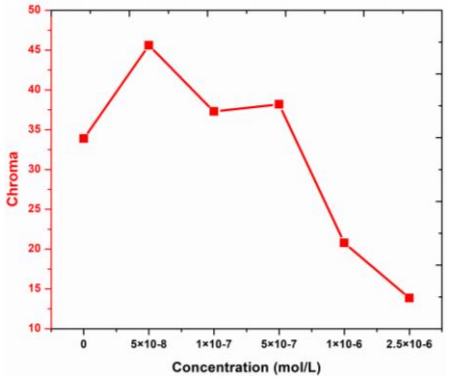

2.4 Selectivity studies of Cr(VI), Pb(II) and Mn(II) using CIE L*a*b*/Yxy chromaticity analysis.

Chromaticity values depend only on dominant wavelength and saturation and are independent of the amount of luminous energy. The CIE chromaticity diagram is a horseshoe-shaped diagram that can be drawn using x and y values for all visible colours. The center point of the diagram represents a standard white light which estimates sunlight. The chromaticity diagram is useful for comparing colour gamut for different sets of primaries, determining the dominant wavelength and purity of a given colour and identifying complementary colours. The red, green and blue primaries can only generate colours inside or on the bounding edges of the triangle in a CIE chromaticity diagram. The CIE chromaticity diagram can never be filled by a single triangle which completely fills. That is why no set of three primaries can be additively combined to generate all visible colours. Colorimetric detection using gold nanoparticles for the detection of Cr(VI) and Pb(II) is presented in photographic image (a) and (e), respectively. The AuNPs solutions changed from wine-red to blue upon addition of Cr(VI) and Pb(II) in both photographic images (a) and (e) and the chromaticity diagrams corresponded to the colours depicted in the photographic images and the points representing Cr(V) and Pb(VI) were observed in the blue region. Meanwhile, the RGB curves followed the same trend with for all the investigated metal ions with GB curves almost identical. The investigated metal ions in photographic image (b) yielded yellow coloured AgNPs and the AgNPs solution changed to orange-brown after the addition of Cr(III) and (VI). No significant changes were observed were observed in the chromaticity diagram. No apparent trend was observed in the RGB curves. A reddish brown and blue colours were observed upon addition of Cr(VI) and Mn(II) in AgNPs yellow solutions in photographic images (c) and (d), respectively. This was further confirmed by the corresponding shift to the red region for the Cr(VI) point in the chromaticity diagram , while all the other points were observed in the yellow region in chromaticity diagram (c). The blue coloured solution observed in photographic image (d) yielded a point in the blue region corresponding to Mn(II) in chromaticity diagram (d). Additionally, a rapid decrease in the R and G curves was observed in photographic images (c) and (d) for Cr(VI) and Mn(II), respectively.

Table 2.4: Showing the CIE L*a*b* chromaticity and RGB colour models of interfering ions for the detection of Cr(VI), Pb(II) and Mn(II).

Photograph images	Ref	Chromaticity analysis	
		CIE_{Lab} Chromaticity	RGB colour model graphs
(a) 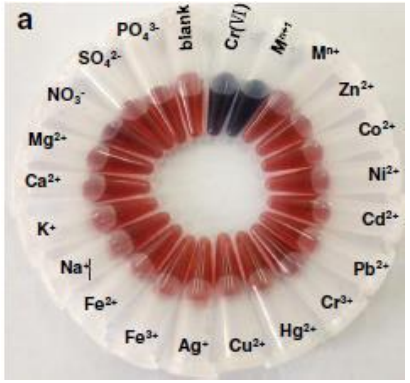	(Liu, Leng and Lin 2016)	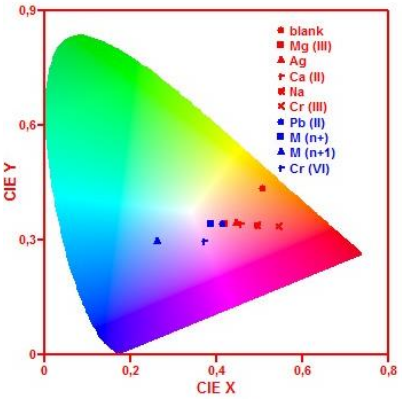	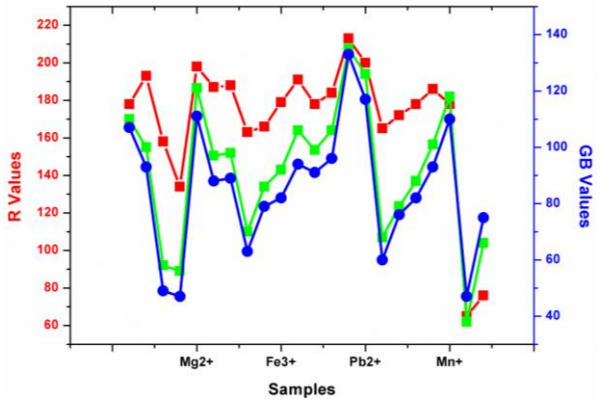
(b) 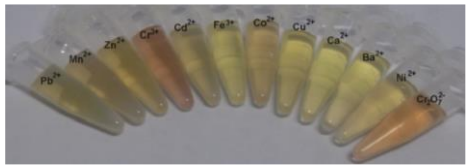	(Wu *et al.* 2013)	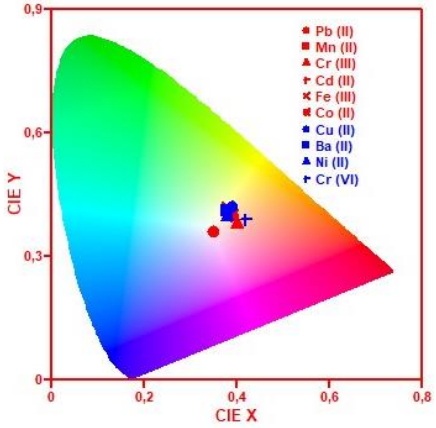	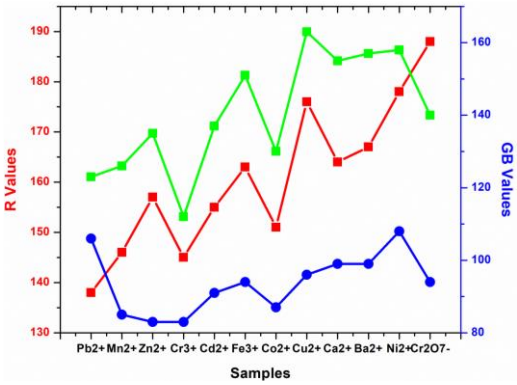

(c) 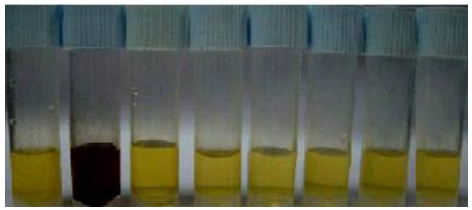	(Ravindran *et al.* 2012)	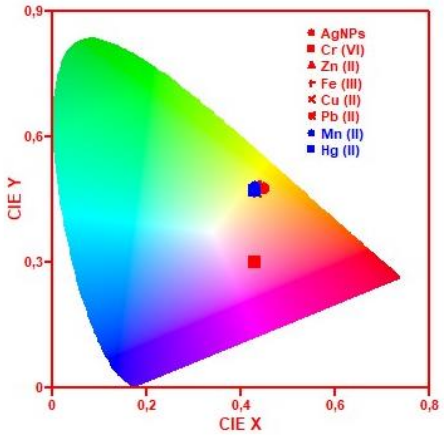	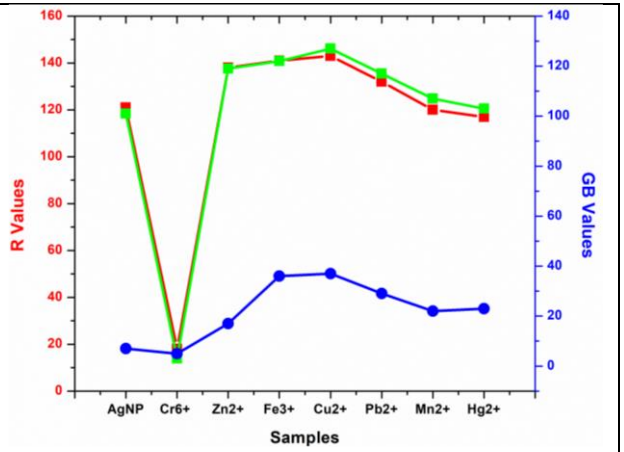
(d) 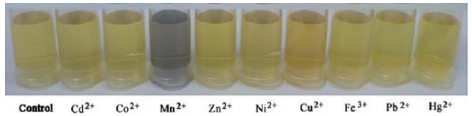	(Zhou *et al.* 2012)	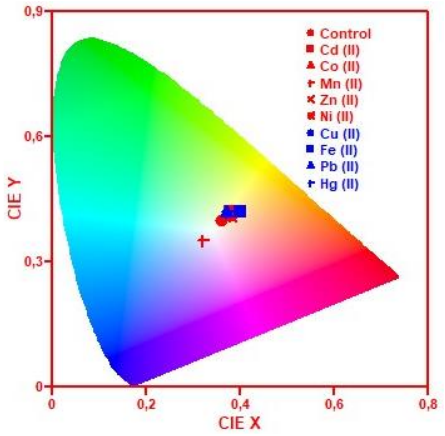	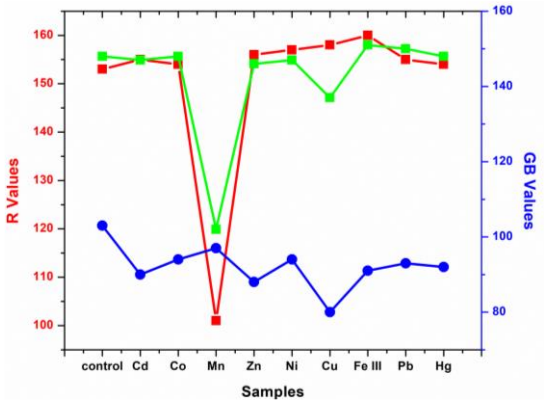

(e) 	(Ratnarathorn, Chailapakul and Dungchai 2015)	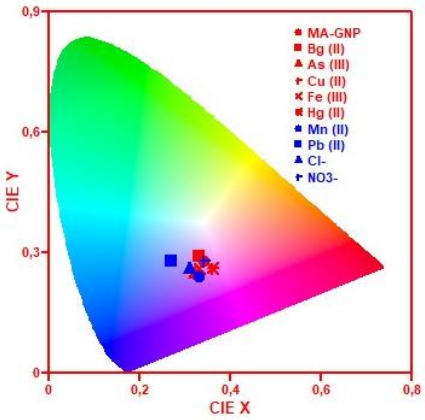	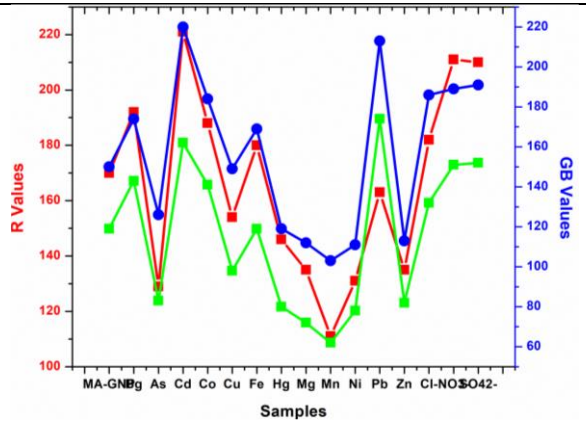

2.5 Detection limits of Cr(VI), Pb(II) and Mn(II)

The detection limits of citrate capped gold and silver nanoparticles, functionalized gold and silver nanoparticles for the colorimetric detection of Cr(VI), Pb(II) and Mn(II) reported in literature are represented below in Table 2.5.

Table 2.5: Showing reported LOD's of functionalized AuNPs and AgNPs for the detection of Cr(VI), Pb(VI) and Mn(II).

Analyte	Capping ligand	LOD	Reference
Cr(VI)	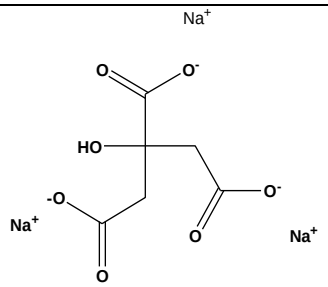 sodium citrate	0.4 nM	(Kanagaraj *et al.* 2017)
	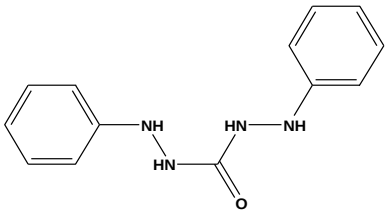 1,5-diphenylcarbazide	0.3 µM	(Liu, Leng and Lin 2016)
	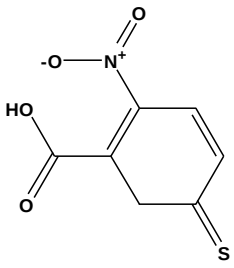 5-thio-(2-nitrobenzoic acid)	1 µM	(Lai and Tseng 2011)
	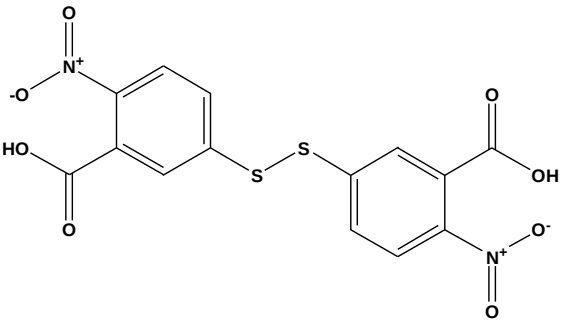 5,5-dithiobis(2-nitrobenzoic acid)	25 ppt	(Hughes *et al.* 2013)

Mn(II)	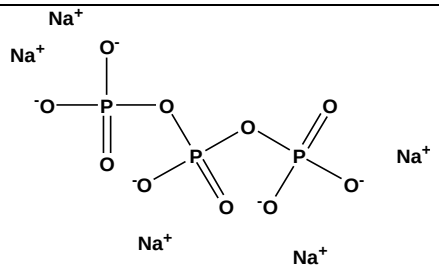 sodium triphosphate	0.1 µM	(Gao *et al.* 2013)
Mn(II)	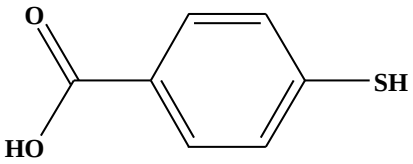 **4-mercaptobenzoic acid** and 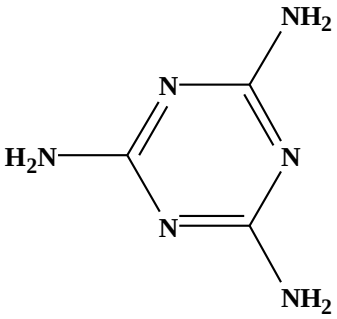 **melamine**	5×10^{-8} M	(Zhou *et al.* 2012)
Pb(II)	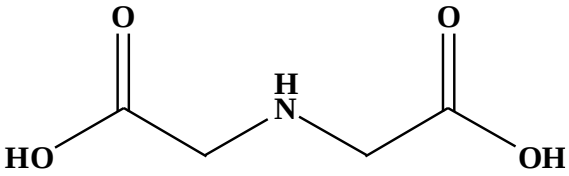 **iminodiacetic acid**	13 nM	(Qi, Shang and Wu 2012)

CHAPTER THREE

3.0 MATERIALS AND METHODS

3.1 Experimental

3.1.1 Chemicals and Reagents

Gold chloride trihydrate (>99.9%) ($AuCl_4H_7O$) was purchased from Leap Chem (Hangzhou, China) through DLD Scientific (Durban, South Africa). Tri-sodium citrate dihydrate (>99%) ($Na_3C_6H_5O_7$) was purchased from Merck (Pty) Ltd (Durban, South Africa) and Potassium dichromate ($K_2Cr_2O_7$) from Associated Chemical Enterprises (Johannesburg, South Africa). All solutions were prepared using deionized water (18.2 MΩcm specific resistance). All chemicals that were used for synthesis of functionalization ligand complexes were purchased from Sigma-Aldrich and Merck (St. Louis, Missouri United States) and used without further purification. Solvents used were of synthesis grade.

3.1.2 Characterization of AuNPs, AgNPs and ligand complexes

UV-Vis spectrophotometer Cary UV 50 from Varian was used to investigate the optical properties. All spectra were recorded from 350 to 800 nm. Particles size and shape were investigated using Transmission Electron Microscope (TEM) carried out on a TEM CM 120 model from Philips operated at an acceleration voltage of 120kv. The melting point was determined by Stuart SMP 10. The IR spectra were recorded on Varian Scimitar 1000 FT-IR using KBr pellets and the absorption frequencies were expressed in reciprocal centimeters (cm^{-1}). The NMR spectra were recorded on a BRUKER 400 MHz spectrometer. The chemical shifts values were recorded on δ scale and the coupling constants (*J*) in Hertz. A TOF-MS analyzer for mass measurement was used. The progress of the reaction was monitored by TLC using aluminium plates with silica gel. The elemental analysis (C, H, N) were obtained from a Perkin Elmer (Waltham, Massachusetts, United States) precisely 2400 analyzer. Dynamic light scattering (DLS) measurements of the AgNPs solution were measured using a Malvern Zetasizer Nano instrument (Zetasize Nano S90).

3.1.3 Synthesis of gold and silver nanoparticles.

3.1.3.1 Synthesis of citrate capped gold nanoparticles

The standard method, reported in literature (Turkevich, Stevenson and Hillier 1951) was adopted for the synthesis of AuNPs with slight modifications. Prior to synthesis, stock solutions of trisodium citrate dihydrate (1 g in 100 mL deionized water) and $HAuCl_4.3H_2O$ (1.14 g in 100 mL deionized water) were prepared separately. In a typical reaction, 961 mL deionized water was transferred in a conical flask and heated to boil. While stirring at 1200 rpm, 10 ml of $HAuCl_4.3H_2O$ stock solution was added and the solution was allowed to boil, followed by the quick addition of 28.9 mL tri-sodium citrate dehydrate solution. The solution turned grey in 1 - 2 min, and then dark purple to red, and finally reddish-orange. To maintain the size and shape of the particles already formed, and making sure that the reaction is complete, the flask was then removed from the hot plate and transferred to another plate where stirring was continued for 2 h at room temperature.

3.1.3.2 Synthesis of silver nanoparticles

A standard method reported in literature (Balavigneswaran *et al.* 2014) was adopted and slightly adjusted. sodium citrate was used as a modifier and $NaBH_4$ as a reducing agent for the preparation of citrate-capped silver nanoparticles. Briefly, 2.0 mL of sodium citrate (58.80 mM) solution was added into the reaction flask that contained 78.0 mL of $AgNO_3$ (2.04 mM) solution under vigorous stirring. After 20 min, 20 mL of $NaBH_4$ (2.65 mM) was added into the above solution at room temperature and stirred for 1 h. The dark colloidal solution colour then changed to bright yellow, confirming that the formation of citrate-capped AgNPs. The citrate-capped AgNPs solution was stored in the dark at 4.0 ± 2.0 ^oC to remain stable for several weeks.

3.1.4 Synthesis of functionalization complex ligands

3.1.4.1 Synthesis of 3-(p-tolyl)-2,3-dihydropyrazolo[3,4-b] indole-1(4H)-carbothioamide (TRPIDA_CH3)

Compound **(4)** scheme 3.1 was prepared by adding toluidine **(1)**, thio-semi-carbazide **(2)**, and indole **(3)**, in the presence of indium chloride as catalyst, with acetonitrile acting as a solvent. The reaction was refluxed for 12 hours at room temperature. Upon reaction completion, column chromatography was employed for product purification. Finally, 80% yield of pure red-brown solid was obtained.

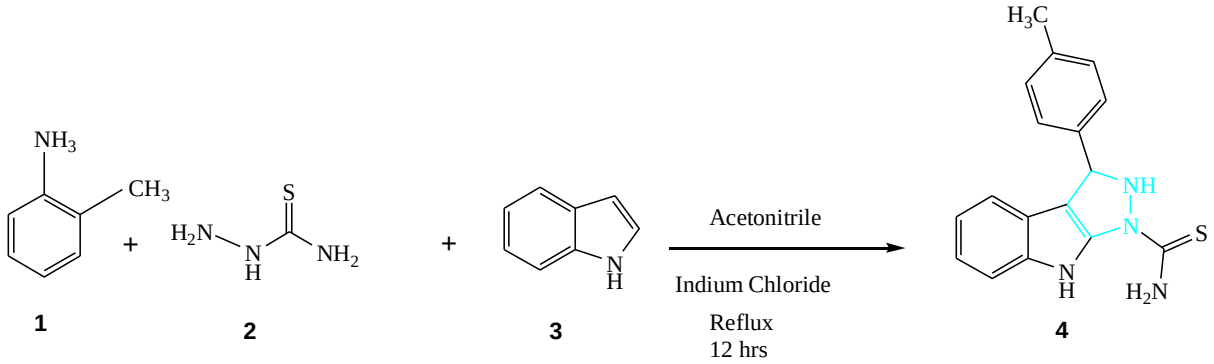

Scheme 3.1: Outline synthesis of TRPIDA_CH3 complex

3.1.4.2 Synthesis of 1-methyl-6-phenyl-6, 7-dihydro-5H-indolo [3, 2-c] [1, 8] naphthyridine (TRPIDB_H)

The synthesis of TRPIDB_H compound **iv** was successfully prepared through the Povarov reaction by [4+2] cycloaddition. In this reaction, an electron-rich dienophile **i** reacted with a diene (N-aryl aldimines) which was produced by a reaction between 2-amino-4-picoline **ii** with benzaldehyde **iii**. Indium chloride was used as a catalyst for this reaction to produce the target compound TRPIDB_H **iv** Scheme 1 as shown in Scheme 3.3. The reaction produced a yield of 88 %.

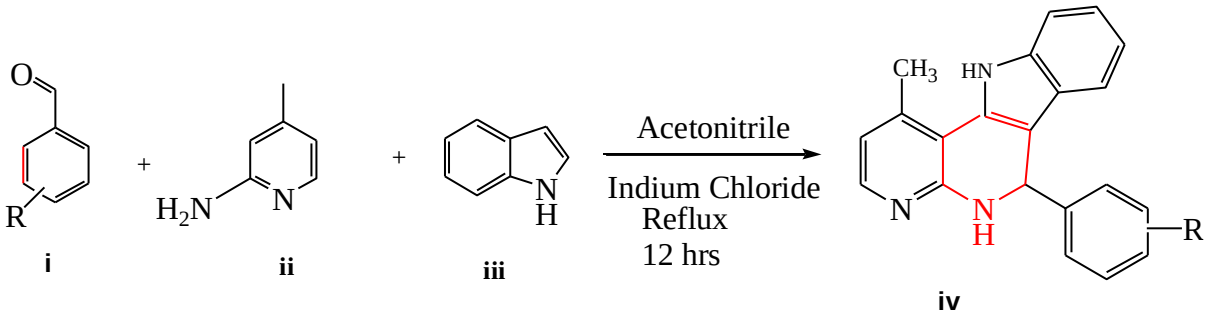

Scheme 3.2: Outline synthesis of TRPIDB_H

3.1.4.3 Synthesis of 3-(4-hydroxy-3-methoxyphenyl)-2, 3-dihydropyrazolo [3, 4-b] indole-1(4H)-carbothioamide

Preparation of TRPIDA_V (**d**) in Scheme 3.3 was conducted by adding a mixture of benzaldehyde derivative (**a**) (1 mmol), thio-semicarbazide derivative (**b**) (1 mmol) and indole (**c**) (1 mmol) in acetonitrile (20 mL), was refluxed for 12 hours. The reaction product was poured into an ice-bath and the precipitate was collected by filtration, washed with deionized water and dried. The resulting crude product was purified by column chromatography using a solvent system of hexane: ethyl acetate (88:12) to isolate a reddish-brown compound (**d**) with a yield of 88 %.

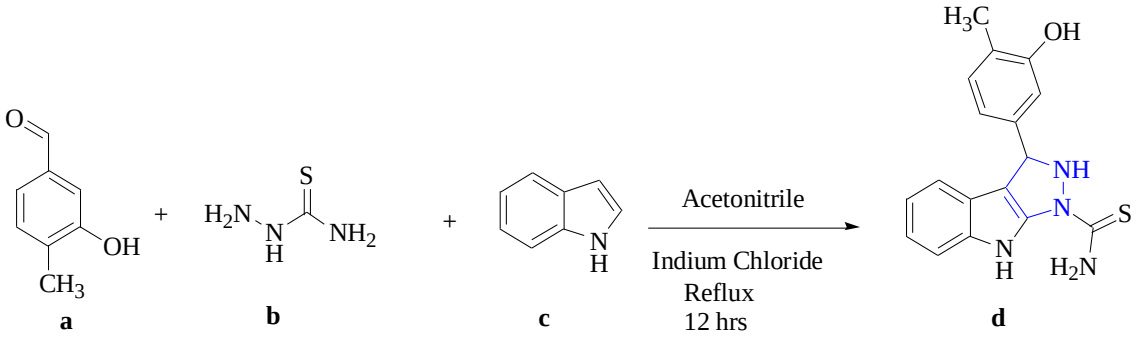

Scheme 3.3: Outline synthesis of TRPIDA_V complex.

3.1.5 Fabrication of AuNPs and AgNPs with complex ligands

3.1.5.1 Fabrication of gold nanoparticles with TRPIDA_CH_3 complex

Initially, a 2.0 mM TRPIDA_CH_3 solution was prepared by dissolving 0.0031 g in 10% dimethyl sulfoxide (DMSO). To a solution of 50 mL AuNPs, 500 μL of TRPIDA_CH_3 solution was added and stirred at room temperature for 90 min. The mechanistic assay showing the dispersion of AuNPs with TRPIDA_CH_3 ligand is shown in Scheme 3.4 forming TRPIDA_CH_3-AuNPs.

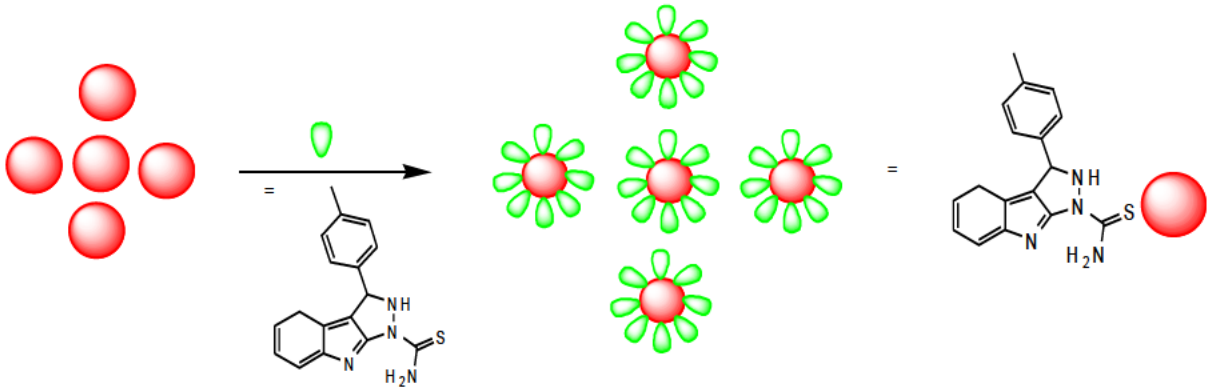

Scheme 3.4: Proposed mechanism for the modification of AuNPs with TRPIDA_CH_3

3.1.5.2 Fabrication of gold nanoparticles with 1,5-diphenyl carbazide

A 2.0 mM 1,5-diphenylcarbazide (DPC) solution was firstly prepared in ethanol. An aliquot of DPC solution (2 mM, 500 µL) was added with stirring to a solution of citrate capped AuNPs (0.01 mM, 50 mL). The mechanistic assay showing the dispersion of AuNPs with DPC is shown in Scheme 3.5 forming DPC-AuNPs.

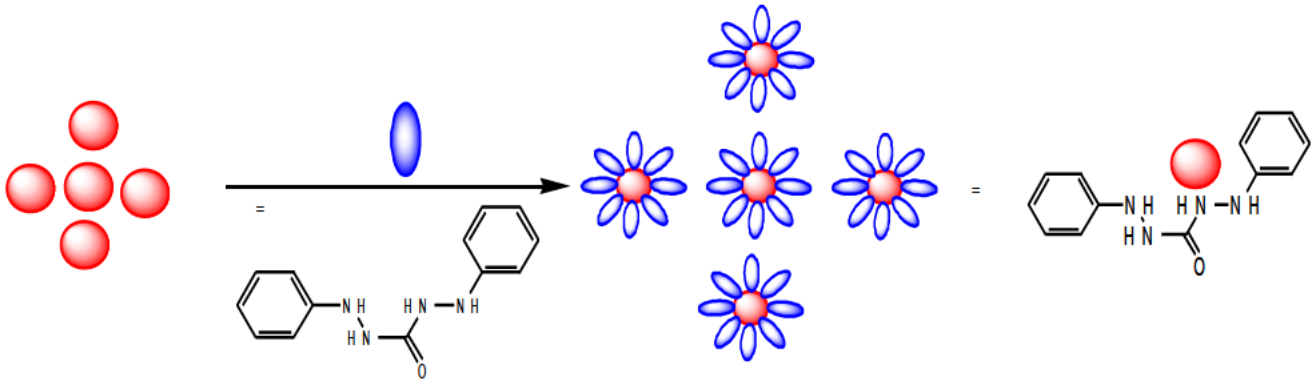

Scheme 3.5: Proposed mechanism for the modification of AuNPs with DPC

3.1.5.3 Fabrication of silver nitrate with TRPIDB_H complex

A 2.0 mM TRPIDB_H solution was prepared by dissolving 0.0036 g in 10% dimethyl sulfoxide (DMSO). To a solution of 50 mL AgNPs, 500 µL of TRPIDB_H solution was added and stirred at room temperature for 90 min. The mechanistic assay showing the dispersion of AgNPs with TRPIDB_H ligand is shown in Scheme 3.6 forming TRPIDB_H-AgNPs.

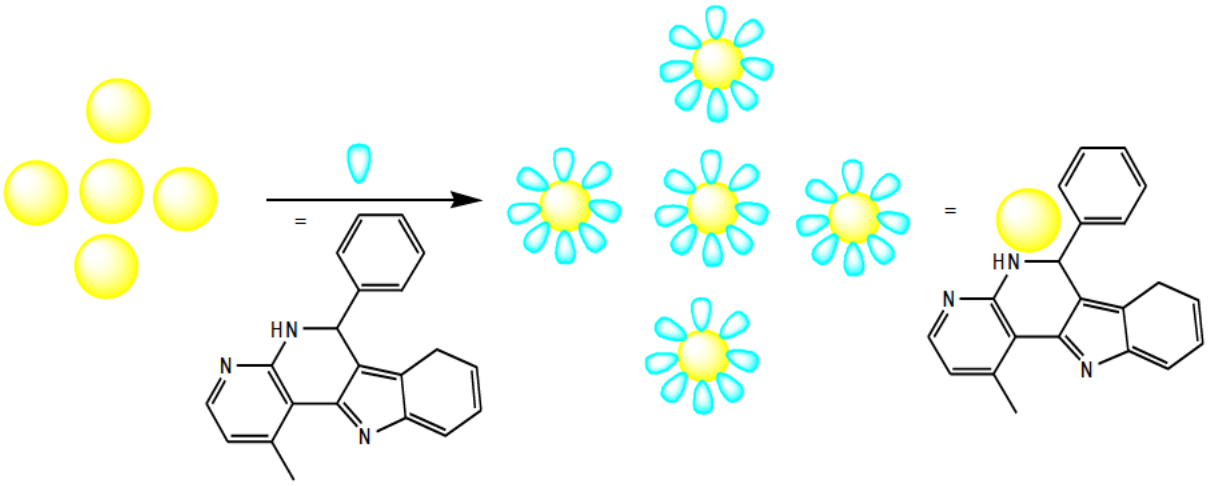

Scheme 3.6: Fabrication of gold nanoparticles with TRPIDB_H

A 2.0 mM TRPIDA-V solution was prepared by dissolving 0.0032 g in 10% dimethyl sulfoxide (DMSO). To a solution of 50 mL AuNPs, 500 µL of TRPIDA_V solution was added and stirred at room temperature for 90 min. The mechanistic assay showing the dispersion of AuNPs with TRPIDA_V ligand is shown in Scheme 3.7 forming TRPIDA_V-AuNPs.

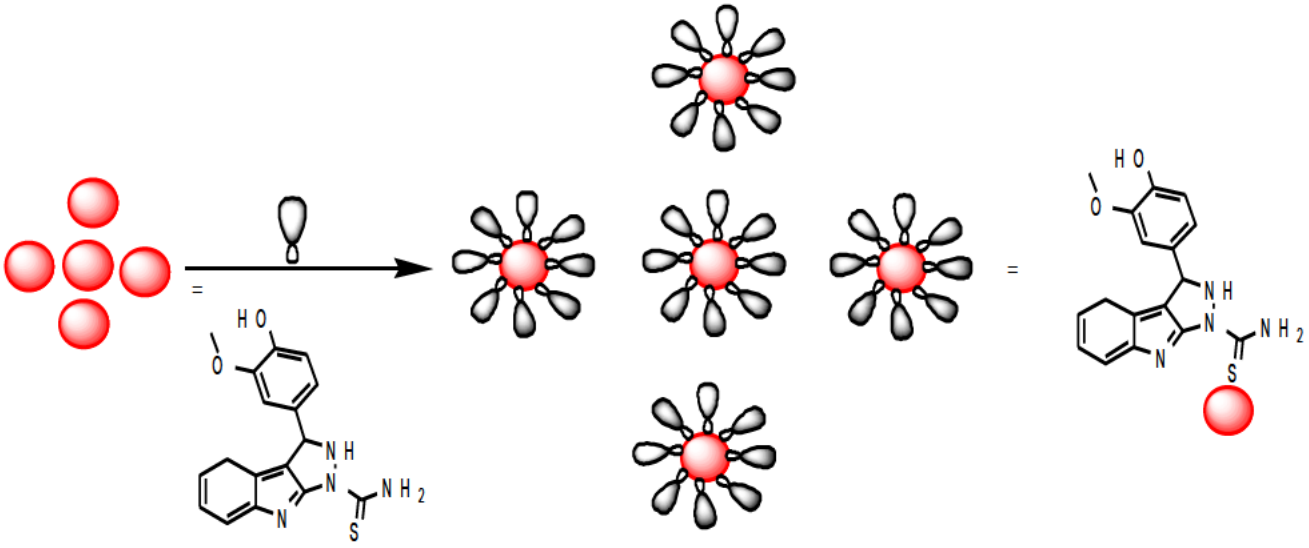

Scheme 3.7: Proposed mechanism for the modification of AuNPs with TRPIDA_V

3.1.6 Preparation of working standards

3.1.6.1 Preparation of Cr(VI) standard solutions and their treatment with gold nanoparticles (Case study I)

For the UV-Vis spectrophotometric analysis and image processing, stock solution of 1000 µM of Cr(VI) was prepared from 1000 mg/L stock solution and made to mark (50 mL) with deionised water. The working standard solutions were prepared by dilution of the stock solution with deionised water to get a concentration range of 0.5 to 100 µM. To separate cuvettes containing 700 µL TRPIDA_CH_3 capped AuNPs solution and 300 µL of each Cr(VI) standard solution was added.

3.1.6.2 Preparation of Cr(VI) standard solutions and their treatment with gold nanoparticles (Case study II)

A stock solution of 1000 µM of Cr(VI) was prepared from 1000 mg/L stock solution and made to mark in 50 mL with deionised water. The working standard solutions were prepared by dilution of the stock solution with deionised water to get a concentration range of 0.5 to 50 µM. In a 600 µL AuNPs solution, 100 µL HEPES buffer (50 mM, pH 7) and 300 µL of each Cr(VI) standard solution was added.

3.1.6.3 Preparation of Pb(II) standard solutions and their treatment with gold nanoparticles (Case Study III)

The working standards of Pb(II) were prepared from a 1000 mg/L stock solution and made to mark in 50 mL with deionised water. The working standard solutions were prepared by dilution of the stock solution with deionised water to get a concentration range of 1 to 100 mg/L. In a 700 µL AuNPs solution, 300 µL of each Pb(II) standard solution was added.

3.1.6.4 Preparation of Mn(II) standard solutions and their treatment with gold nanoparticles (Case Study IV)

The working standards of Mn(II) were prepared from a 1000 mg/L stock solution and made to mark in 50 mL with deionised water. The working standard solutions were prepared by dilution of the stock solution with deionised water to get a concentration range of 0.5 to 10 mg/L. In a 800 µL AuNPs solution, 200 µL of each Mn(II) standard solution was added.

3.1.7 Selectivity Studies

In case of selectivity studies, all samples were prepared in the similar way, under the same optimized conditions. We investigated the selectivity of our methods for our target metal over other metal ions, i.e. Cr(III), Cu(II), Cd(II), Fe(III), Ni(II), Zn(II), Pb(II), Mn(II) and M^n (mixed ions)

3.1.8 Analysis of the intensity of colours using a smartphone

A Mobicel R6 smartphone was used to capture the intensity of each gold standard. The Color Grab app version 3.8.1 developed by Loomatix Ltd was installed and used to analyse the intensity of gold nanoparticles. The RBG values that were obtained from Color Grab app were converted to XYZ chromaticity diagram.

3.1.9 Computational simulations

The relative surface-to-molecule orientation on gold nanoclusters were modelled following our published work with minor alteration (Harris, Mlambo and Mdluli 2016). In this case AuNPs with diameters of 0.5 nm (cluster sizes Au43) were constructed and surfactant adsorption was simulated (*via* a simulated annealing Monte Carlo scheme) and surfactants were allowed to be adsorbed onto the AuNP surfaces. Since a trade-off exists between simulation accuracy and computational time it becomes increasingly more difficult to accurately execute molecular mechanics and dynamics calculations on large gold clusters. Therefore, the aforementioned nanocluster sizes were selected and simulated to reduce simulating cost and time. It was found that for the largest nanocluster, the computational time (wall-clock time) became too large to continue with even larger sizes. However, although these simulated nanocluster sizes were not having the same size as those used in experimental investigation because of the cost of

calculation, the same trends can still be observed as discussed below. Molecular mechanics were used to determine the optimum geometries for each of the resulting DPC, DPC–AuNP systems, and molecular dynamics simulations were performed on each of the systems to arrive at the energy-optimized configurations. The molecular dynamics simulation in canonical ensemble (constant atom number, volume and temperature (NVT)) was utilized to fully understand the adsorption of PVP on the surface of three silver crystal facets i.e. Ag(100) , Ag(110) and Ag(111). The interaction energies between PVP and silver crystal facets were calculated. All simulations were executed using the Accelrys Discovery Moduleof Materials Studio (version 7.01.100) [Accelrys: Materials Studio is a Software Environment for Molecular Modelling (Version 7.01.100). Accelrys Inc. (2013)]. The COMPASS force field was used to calculate the intermolecular potential energy of DPC-AuNP complexes. The models indicating the absorption of DPC were generated using absorption locator of Material Studio using COMPASS force field. All systems were subjected to energy minimization for geometry optimization before molecular dynamics simulations were conducted. The molecular dynamic simulation using NVT lasted for 50 ps with a time step of 1 fs and all atomic density profiles were collected in the last 50 ps simulated molecular dynamics results for each model.

3.1.10 Conversion of RGB colour coordinates to XYZ and CIE L*a*b* colour space

The RGB and CMYK colour models are viewer/device dependent because the range (gamut) of each is dependent on the colour capturing or rendering capabilities of the respective viewer or device. The CIE models/systems are unambiguous, absolute, and device independent-i.e., not tied to, influenced by, or dependent on, the characteristics or capabilities of any colour capturing or rendering device. RGB values were estimated using frequency histogram tool in ImageJ software. The solution to convert digital images from the RGB space to the CIE XYZ colour space is as follows (Zhang and Wandell 1996):

$$X = 0{,}4303R + 0{,}3416G + 0{,}1784B$$

$$Y = 0{,}2219R + 0{,}7068G + 0{,}0713B \qquad \text{Equation 3-1}$$

$$Z = 0{,}0202R + 0{,}1296G + 0{,}9393B$$

The CIE L*a*b* colour space is based on the so-called opponent colour model which are colours lying opposite each other on both sides of the plane (along L) and on the a*b* plane cannot be seen simultaneously. This means that either dark or bright is seen, either red or green

and either yellow or blue (L*=black/white, a*=red/green and b*=yellow/blue). The CIE L*a*b* colour space is a mathematical transformation of the CIE XYZ space, defined as follows (Hunt and Pointer 2011):

$$L^* = 116\,(Y/Y_0)^{1/3} - 16$$

$$a^* = 500\,((X/X_0)^{1/3} - (Y/Y_0)^{1/3}) \qquad \text{Equation 3-2}$$

$$b^* = 200\,((Y/Y_0)^{1/3} - (Z/Z_0)^{1/3})$$

X, Y, Z, X_0, Y_0, and *Z_0* are the coordinates of CIE XYZ colour space where *X_0, Y_0,* and *Z_0* are values of reference (TRPIDA_V-AuNPs).

3.1.11 Optical properties and image processing

The photograph images of the capped TRPIDA_V-AuNPs with different concentrations of Mn(II) and different metal ions for selectivity studies were captured with a Samsung A71 smartphone. The photograph images were then transferred to a HP laptop for further processing using ImageJ software. The RGB values were obtained using the software Histogram analysis. The segmentation method of the CIEL*a*b*/Yxy optimization is presented in Scheme 3.8.

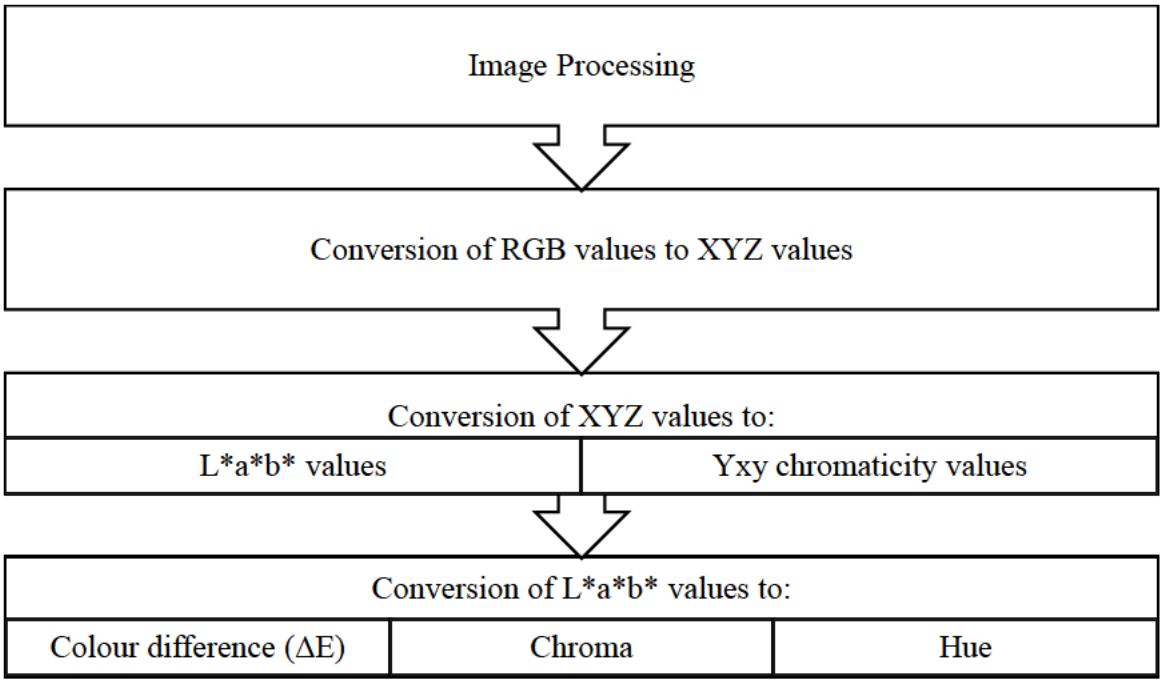

Scheme 3.8: Segmentation method of image processing

CHAPTER FOUR

CASE STUDY I

4.1 Synthesis and characterization of 3-(p-tolyl)-2,3-dihydropyrazolo[3,4-b] indole-1 (4H)-carbothioamide functionalized gold nanoparticles for the CIEL*a*b*/Yxy colorimetric detection of Cr(VI)

4.1.1 Characterization of synthesized citrate capped AuNPs

The characterization of AuNPs by UV-Vis and TEM is presented in Figure 4.1. A clear and significant peak due to the successful formation of citrate-AuNPs was observed around 520 nm, represented as AuNPs in Figure 4.1 (a). Figure 4.1 (b) shows the TEM image of the synthesized AuNPs, together with its corresponding particle size distribution (insert). Spherical nanoparticles with an average diameter of 13 ± 0.9 nm were observed as witnessed by the TEM image.

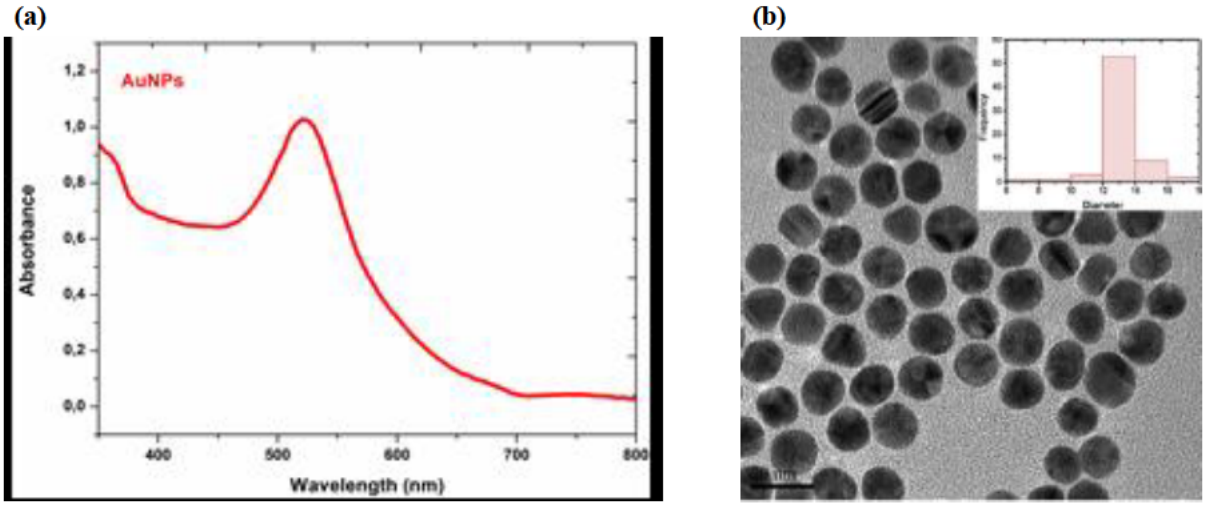

Figure 4.1: (a) UV-Vis spectra of the citrate capped AuNPs and (b) TEM image of AuNPs sample at 20 nm scale (insert of corresponding particle size distribution).

4.1.2 Characterization of the synthesized TRPIDA_CH_3

TRPIDA_CH_3 was successfully synthesized (Scheme 3.1), 80% of pure reddish product was obtained with a measured melting point ranging from 111 to 113 °C. The complex was fully characterized using FT-IR, ^{1}H, ^{13}C NMR, TOF-MS and elemental analysis, Figure 4.2. The characteristic absorption bands in the FT-IR spectrum (Figure 4.2 (a)) showed stretching

absorptions (cm $^{-1}$) at 3456-3383, 1009-1100, 1334 and 726, due to secondary amine N-H stretching, C=S stretching, C-N stretching and secondary amine N-H out of plane bend, respectively. The numbers for peripheral atoms depicted in Figure 4.2 (b) were used to facilitate the assigning of proton and carbon for NMR spectral interpretation.

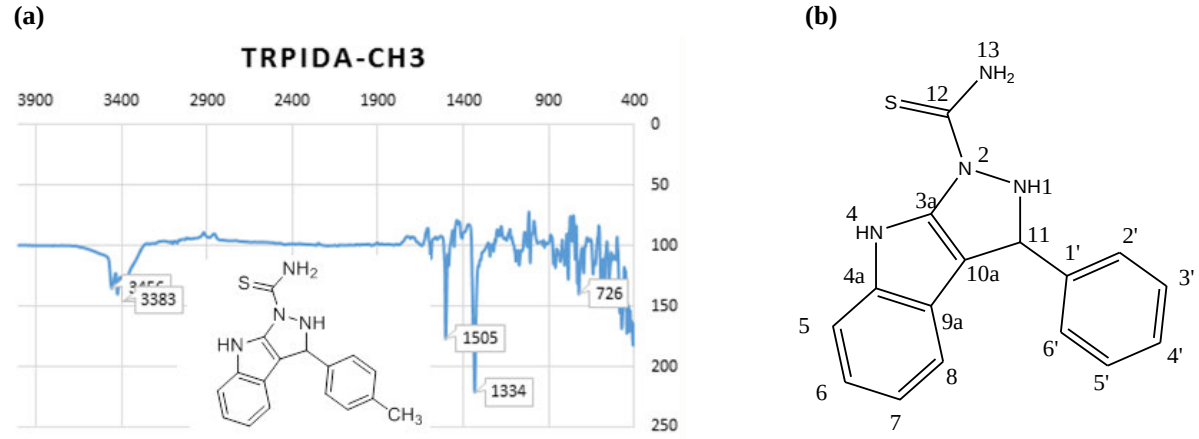

Figure 4.2: (a) IR spectrum of TRPIDA_CH_3 and (b) numbers for peripheral atoms of TRPIDA_CH_3

The ^{1}H NMR spectrum Figure 4.3 (a) displayed a well distinct signals at δ 10.9 for overlapping secondary amine of indole and pyrazole whilst at δ 2.0 exhibited signal for thio-amide. The aromatic protons at δ 7.50 (1H, d, *J* = 7.6 Hz, H-5), 7.40 (1H, d, *J* = 7.6 Hz, H-8), 7.11 (1H, t, *J* = 7.6 Hz, H-6) and 6.92 (1H, t, *J* = 8.0 Hz, H-7) corresponded to indole –CH. The aliphatic singlets at δ 5.80 (s, H-11) exhibited the presence of –CH (sp^3) proton which indorse the formation of a new pyrazole ring. The phenyl ring exhibited protons as doublets at δ 7.30 (2H, d, *J* = 7.6 Hz, H-3' & H-5') whilst another doublets appeared at δ 7.10 (2H, d, *J* = 7.6 Hz, H-2'& H-6') and an aliphatic broad singlets for methyl group resonated at δ 2.3 (s, CH_3) ppm. The ^{13}C NMR Figure 4.3 (b) displayed the presence of ten CH carbons at δ 39.7 (C11), 111.1 (C5), 118.1 (C7), 120.9 (C6), 123.6 (C8), 125.8 (4'), 126.7 (C2' & C6') and 128.0 (3' & C5'). Whilst six quaternary carbons resonated at δ 118.2 (C10a), 119.2 (C9a), 136.7 (C3a & C4a), 144.9 (C1') and 170.4 (C12).

(a) (b)

Figure 4.3: (a) ^{1}H NMR spectrum for TRPIDA_CH_3 and (b) ^{13}C NMR spectrum for TRPIDA_CH_3

The molecular ion peak at *m/z* 333.1 [M^+ + Na] in its mass spectrum Figure 4.4 and calculated molecular ion peak is 308.4 [M^+] which corresponded to molecular formula $C_{17}H_{16}N_4S$. Elemental analysis also confirmed the structure of TRPIDA_CH_3 with chemical composition calculated for $C_{17}H_{16}N_4$ to be: C, 66.21; H, 5.23; N, 18.17; which correlate with the one found experimentally: C, 66.18; H, 5.18; N, 18.15.

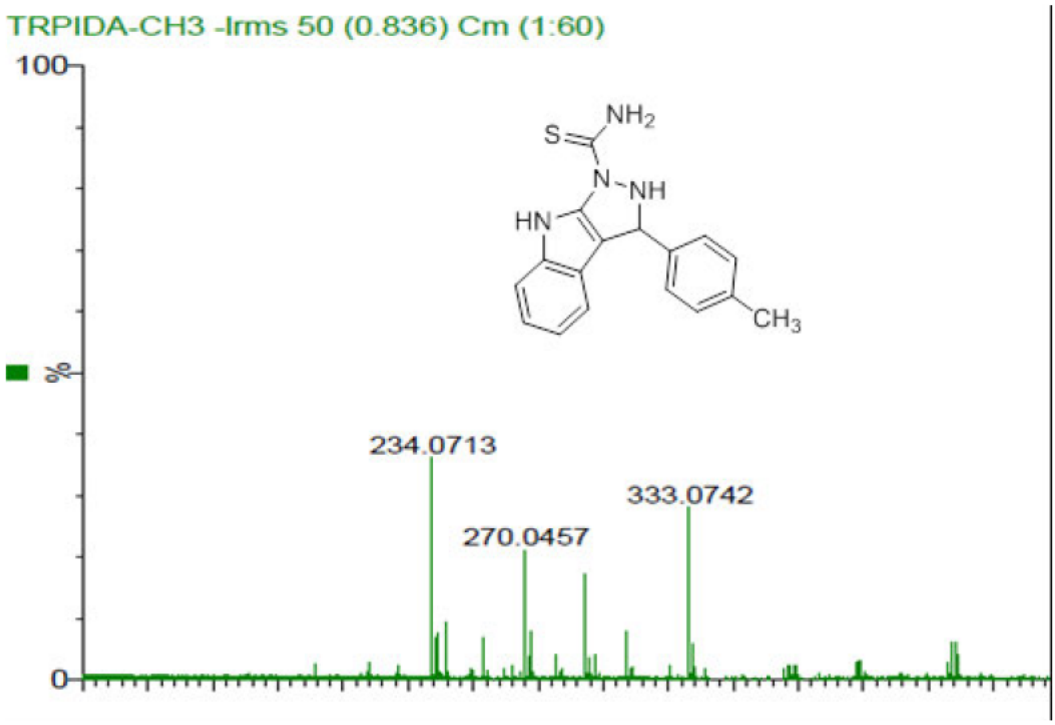

Figure 4.4: TOF-MS spectrum for TRPIDA_CH_3

4.1.3 Optimization of RGB colour coordinates and CIE L*a*b* colour system

A major contributor of systematic errors during the application of colorimetric devices is the limited observation of colours using our eyes. Hence, such limitations can be reduced by using CIE L*a*b*/Yxy. ImageJ software was used to measure the colour dynamics between the reaction of TRPIDA_CH_3-AuNPs and Cr(VI) for image processing. A photograph of standards Figure 4.5 was uploaded to the ImageJ application software to properly expose the colour shades and their corresponding intensities visually in the form of RGB values. Each of the three colours, i.e. red, green and the blue region are represented by the whole numbers in the standard RGB scale ranging from 0 to 255 in the computer desktop colour application (More fill).

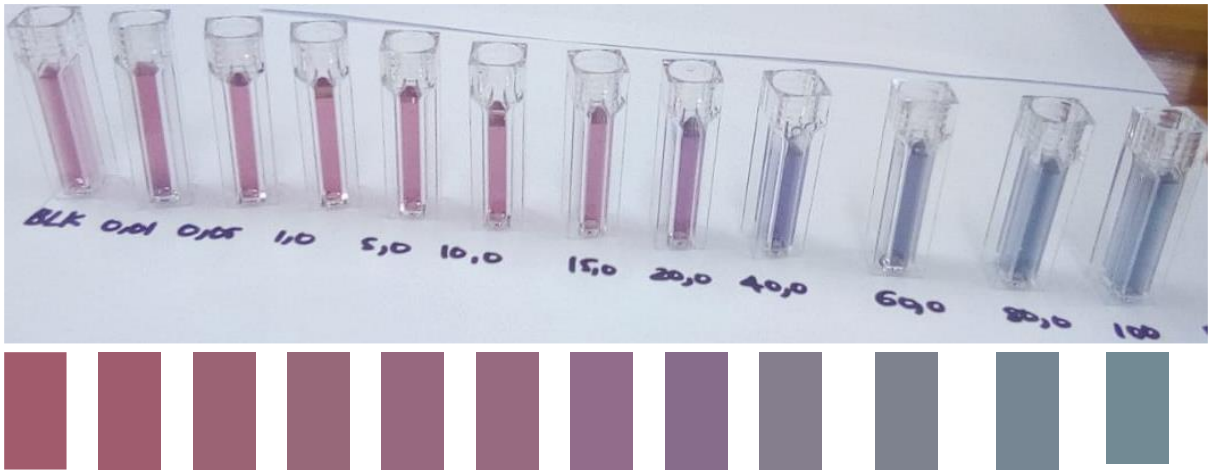

Figure 4.5: Photograph of the TRPIDA_CH_3-AuNPs in the presence of Cr(VI), the volume ratio of TRPIDA_CH_3-AuNPs and Cr(VI) was 700 µL:300 µL.

The colorimetric method of detection of Cr(VI) has constantly been upgraded, retested and renewed to allow the exploitation of the most accurate method (Nxumalo 2019). This allows subjective studies (information which depends on perception and understanding) and quantitative analysis (information which can be estimated numerically) to be explored (Gonzalez and Woods 2002). The use of digital results allows a numerical value to be calculated from the results. It is of great importance to seek for a practical method that is sensitive and efficient for the quantification of Cr(VI) in wastewater effluent. The CIE L*a*b* approach was analysed by the addition of TRPIDA_CH_3-AuNPs and Cr(VI) standards. The reaction resulted in the change of colour which was captured by a Samsung A71 smartphone then transferred to a computer for image analysis using ImageJ software. The change in colour was observed upon the addition of Cr(VI) at 20-100 µM. The intensity of the colour is directly

proportional to the Cr(VI) concentration in the sample (Bower and Holm-Hansen 1980). The colour intensity was obtained by drawing a 10 mm circle in each cuvette clear spot and measure analysis was selected from ImageJ toolbar to get the intensity value. The colour grayscale or intensity gave the amount of Cr(VI) on the basis of the relationship between the colour information and the Cr(VI) concentration. The data obtained was transferred to Origin Pro 8 to interpret the results obtained graphically. The results obtained for the colour intensity are shown in Figure 4.6 (a) and a linear regression fitted to the standard concentration. Furthermore, the obtained intensity results were then converted to absorbance using Equation 4-1

$$A = -log\ (\frac{I}{I0}) \qquad \text{Equation 4-1}$$

Where I is the intensity of light transmitted through the Cr(VI) standard and I_o is the intensity of light transmitted through a blank (TRPIDA_CH_3-AuNPs). This was conducted to quantify the amount of Cr(VI) in the standards using Beer's Law analysis a cell phone camera. The plot of absorbance of Cr(VI) standards vs concentration yielded a straight line relationship Figure 4.6 (b).

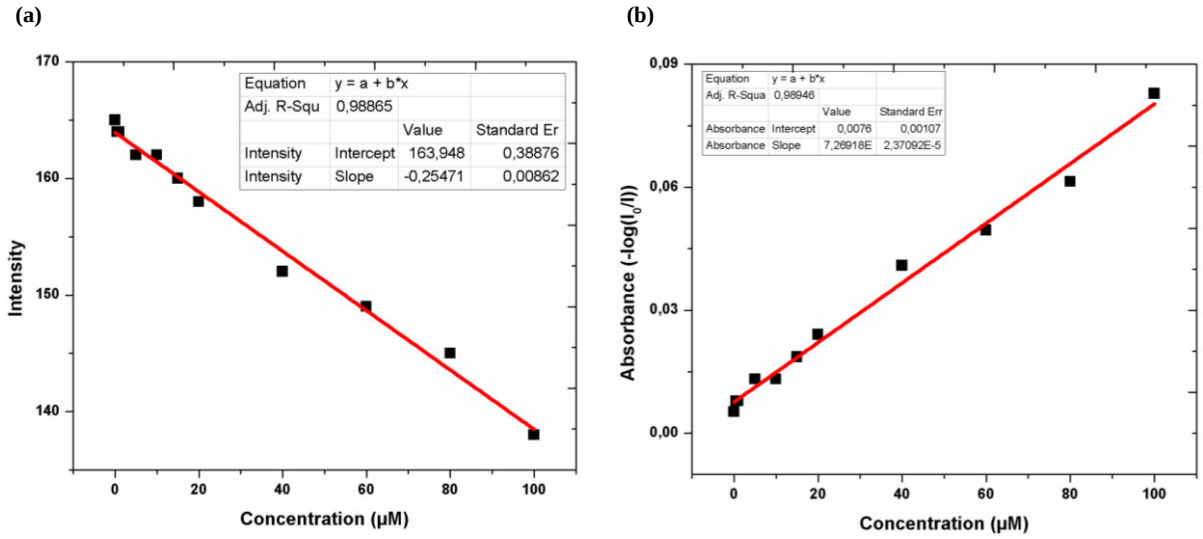

Figure 4.6: (a) Graph of intensity vs. concentration of Cr(VI) TRPIDA_CH_3-AuNPs (blank) 0.01-100 µM and (b) representative plots of absorbance vs concentration of Cr(VI) TRPIDA_CH_3-AuNPs (blank) 0.01-100 µM.

The colour scheme represented by the photograph image in Figure 4.5 was created by incorporating the resultant mean RGB values recorded for each calibration standard into the colour developer using the computer desktop colour application. The created colour pattern for the Cr(VI) calibration standards matched the colours of the solutions. The mean RGB values of the colour insert were measured in ImageJ by analysing each solid colour square separately to get the red, green and blue colour coordinates, the table of all data are provided in Table 4.1.

Table 4.1: Showing RGB values, CIE L*a*b/Yxy colour space, colour difference, hue angle and chroma of Cr(VI) standards

Concentration (µM)	R	G	B	x	Y	L	a*	b*	ΔE_{Lab}	Hue	Chroma
0	161	91	108	0.40	0.30	47.16	30.73	2.94	0.00	0.10	30.87
0.1	159	92	110	0.39	0.30	47.17	29.69	1.72	1.60	0.06	29.74
0.5	155	99	116	0.37	0.30	48.45	25.09	-0.09	6.53	0.00	25.09
1	151	104	121	0.36	0.30	49.33	21.48	-1.85	10.64	-0.09	21.56
5	151	104	127	0.35	0.29	49.51	22.48	-5.15	11.79	-0.23	23.06
10	151	106	128	0.35	0.29	50.03	21.50	-4.97	12.49	-0.23	22.07
15	146	108	138	0.33	0.28	50.30	20.30	-1.56	17.34	-0.48	22.89
20	135	108	139	0.31	0.25	49.18	16.52	-12.95	21.42	-0.67	20.99
40	133	126	141	0.31	0.30	53.85	5.66	-7.14	27.84	-0.90	9.11
60	126	130	142	0.30	0.31	54.40	1.06	-6.97	32.11	-0.92	7.04
80	118	134	147	0.29	0.32	55.09	-2.86	-8.91	36.49	-1.26	9.36
100	116	138	148	0.28	0.31	55.98	-6.21	-8.91	39.78	-1.42	10.86

The green and blue colours of the colour model combined at different concentration levels are almost parallel to each other to form various strong blue shades which were depending on the intensity of the solution for accurate determination of colour. An observation was noted in Figure 4.7 (a) that the green and blue curves followed the same trend suggesting that the colour changed to blue as the Cr(VI) concentration increased. The obtained RGB values were converted to Yxy values using the (http://colormine.org/convert/rgb-to-Yxy). Additional analysis of CIE chromaticity was investigated as shown in Figure 4.7 (b) and were calculated using CIE coordinates using the GoCIE software (Magubane *et al.* 2019). This analysis was based on defining the three standard primary colours *X*, *Y* and *Z* which were combined to produce possible perceived colours and were referred to as imaginary colours (Wyszecki and Stiles 1982). The horseshoe-shaped CIEL Yxy shown in Figure 4.7 (a) confirmed the aggregation of gold nanoparticles by shifting from wine-red colour of gold nanoparticles to blue. The chromaticity diagram colour representations were in agreement with colours observed in Figure 4.5 where the wine-red colours from 0-10 µM represented by the blue symbols in Figure 4.7 (b) are on the red region and the blue colours from 40-100 µM represented by red symbols are on the blue region.

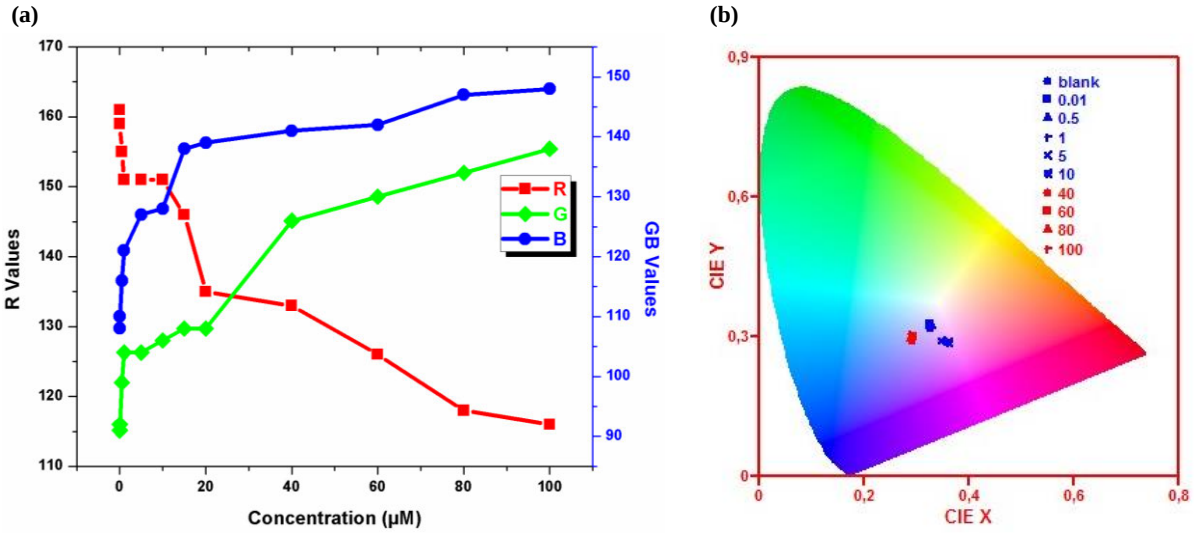

Figure 4.7: (a) Illustration of the R, G, and B colour combination dynamics for the corresponding to Cr(VI) concentration and (b) chromaticity diagram of TRPIDA_CH_3-AuNPs and Cr(VI) standards 0-100 µM.

The images were converted from the RGB colour space to the CIE L*a*b* colour space for measurement of CIE L*a*b* colour system coordinates. Based on the results obtained in Figure 4.8 (a) it was observed that L curve followed the same trend as curve G in Figure 4.7 (b). This is an indication that the standards changed from darkness to lightness, hence, the increasing values. Curve a* followed the same trend as curve R, indicating that standards changed from red to green region (changing from +a to -a), explaining the phenomenon of decrease in a* values. Curve b* is in agreement with what was observed in photograph image Figure 4.5, showing that the standards changed from red to blue as the Cr(VI) concentration increased. This is witnessed by the -b* values from 20 to 100 µM. Colour difference was calculated using Equations 2-1.

The values obtained from the colour difference analysis Figure 4.8 (b) increased as the concentration of Cr(VI) increased indicating that colour difference is directly proportional to the concentration of analyte. Hue angle and chroma were calculated using equation 2-3 and 2-4, respectively. Both hue angle and chroma decreased as the concentration increased Figure 4.8 (c), suggesting that they are inversely proportional to concentration of Cr(VI). The chroma suggested that the standards moved from vivid to dull. Hence, the decrease in values, depicting that as chromaticity increases, colour becomes more intense.

(a)

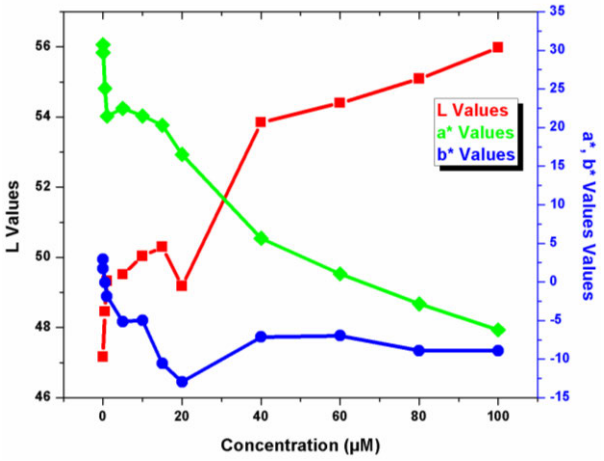

(b)

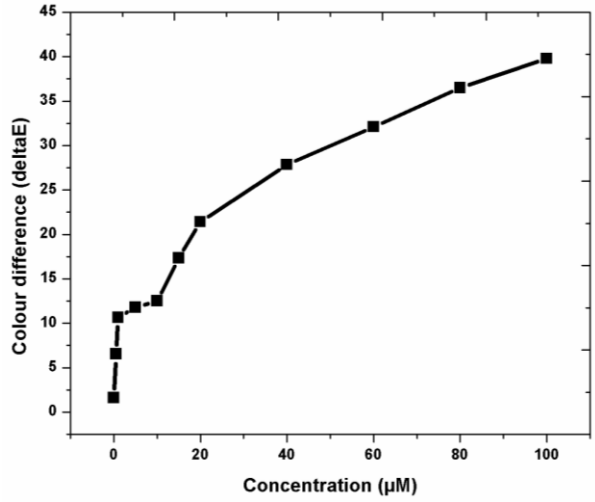

(c)

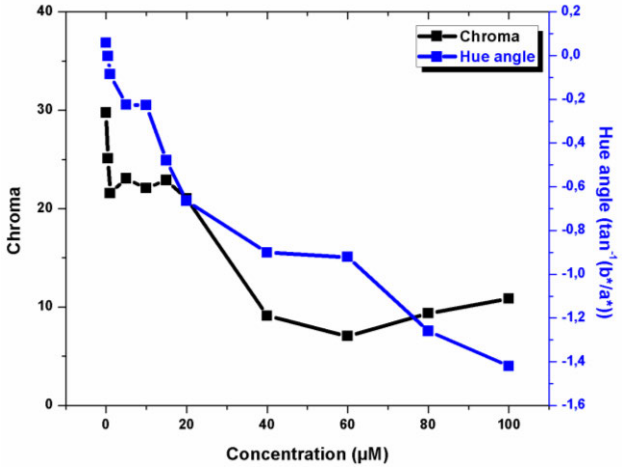

Figure 4.8: (a) Plots of L*a*b* values against concentration, (b) plot of colour difference against concentration and (c) plot of chroma and hue angle *vs.* concentration.

4.1.4 Colorimetric sensing of Cr(VI)

A clear and significant peak due to the successful formation of AuNPs functionalized with TRPIDA_CH_3 was observed around 520 nm, represented as blank in Figure 4.9 (a). No significant change was observed upon addition of Cr(VI) solutions to TRPIDA_CH_3-AuNPs solutions, when the concentration range was 0.01-20 µM. Upon increasing the Cr(VI) solution concentration to 40, 60, 80 and 100 µM, a new broad peak appearing at approximately 645 nm was observed, in addition to the one at 520 nm. The addition of Cr(VI) solutions at different concentrations into TRPIDA_CH_3-AuNPs solutions resulted in a decrease of SPR intensity at 520 nm, whilst the peak intensity at 645 nm increased Figure 4.9 (a). It was also clear that the peak at 520 nm became broader as the concentration of Cr(VI) solution was increased. A significant shift to higher wavelength was also observed as the concentration increased. This was due to the aggregation of AuNPs functionalized with TRPIDA_CH_3 that occurred during the addition of Cr(VI) solutions at higher concentrations. The addition of Cr(VI) induced changes to the surface of the TRPIDA_CH_3-AuNPs causing alterations of particle SPR properties resulting in the red shift from 520 nm to 645 nm. The UV-Vis spectra correlated with the colorimetric assay given in Scheme 4.1. The colour of TRPIDA_CH_3-AuNPs solution changed from wine red to blue, hence the SPR peak shifted to longer wavelengths. Furthermore, it was observed that when Cr(VI) concentration was around 75 µM the variance to the intensity started to reach maximum, indicating aggregation of TRPIDA_CH_3-AuNPs Figure 4.9 (b). This transformation behaviour of TRPIDA_CH_3-AuNPs, demonstrated by LSPR absorption peaks displayed in Figure 4.9 (a), showed that the developed sensor works efficiently in the concentration range of 0.01-100.0 µM. Also, the red colour decreased as Cr(VI) concentration increased suggesting a shift of the LSPR peak of the TRPIDA_CH_3-AuNPs to longer wavelengths due to aggregation.

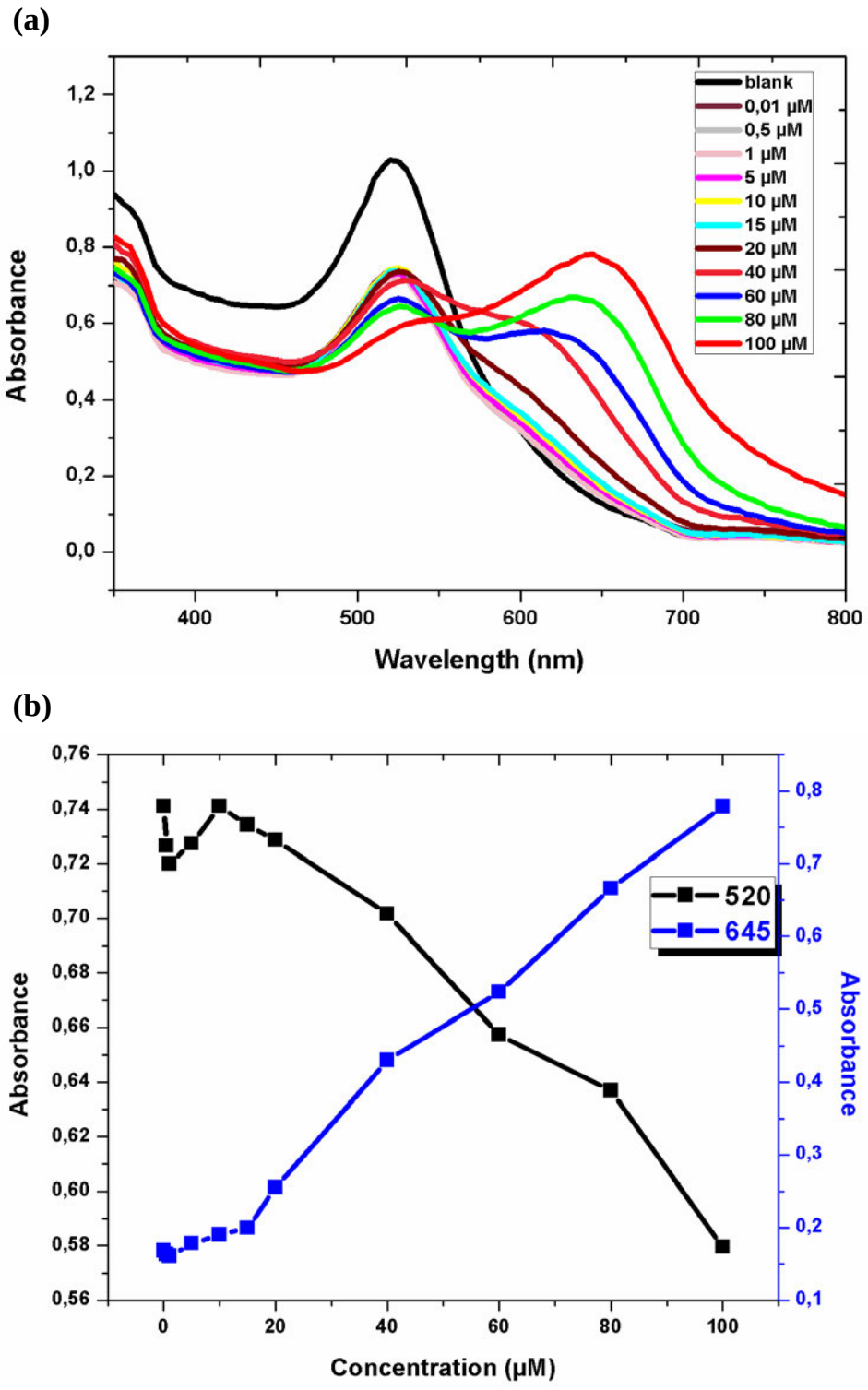

Figure 4.9: (a) UV-Vis spectra of the TRPIDA_CH_3-AuNPs (blank) and after addition of different concentrations of Cr(VI) ranging from 0.01 to 100.0 µM, (b) UV-Vis analysis resultant plot for the evaluation of ionic strength on the performance of TRPIDA_CH_3-AuNPs as efficient sensors for the detection of Cr(VI), measured at 520 nm and 645 nm.

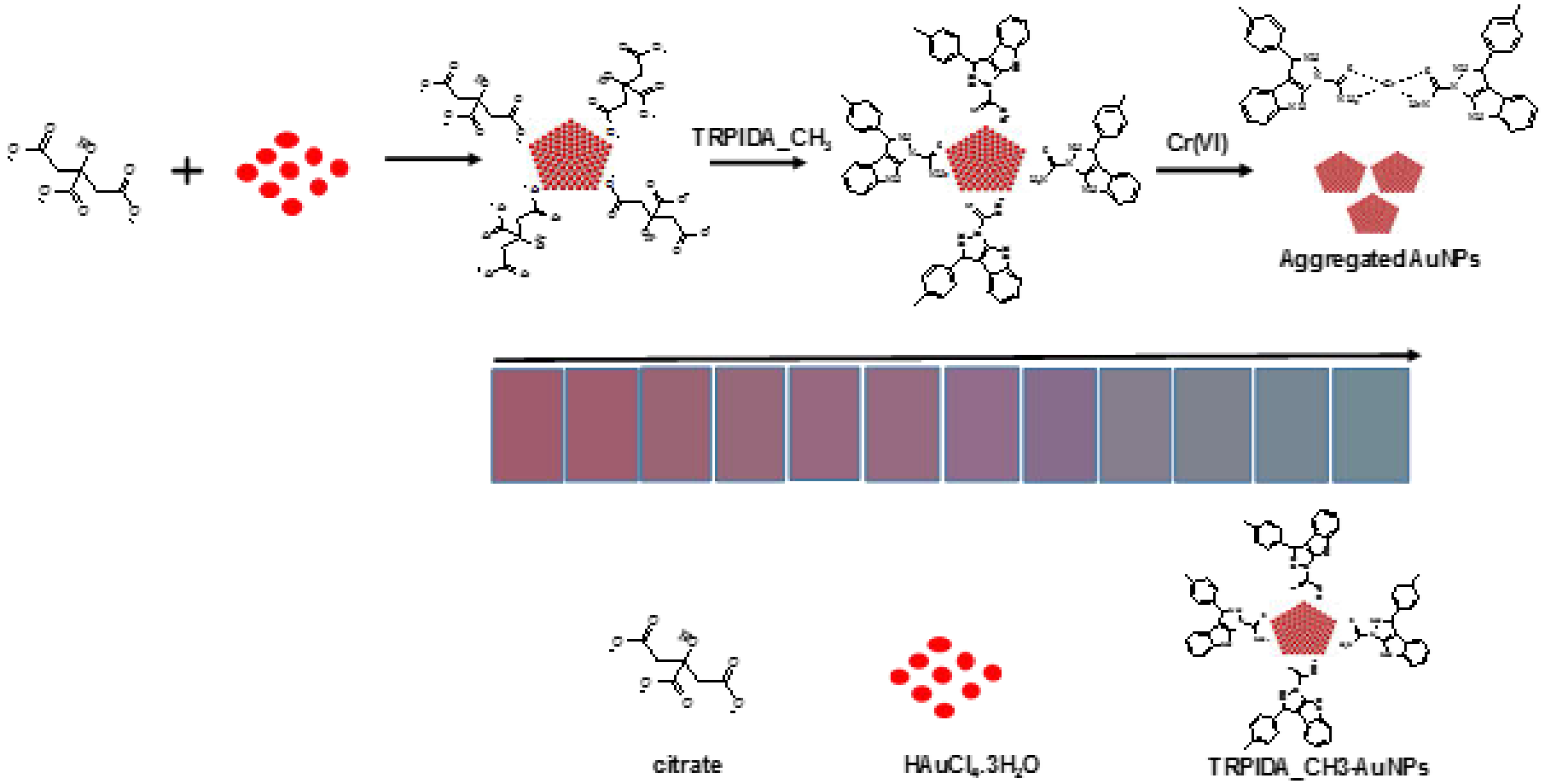

Scheme 4.1: Pathway for colorimetric colour change of TRPIDA_CH_3 AuNPs upon the addition of chromium(VI) (Muthwa et al. 2020).

Due to the availability of the functional groups that can bind to the surface of AuNPs, the water soluble TRPIDA_CH_3 was synthesized and used in functionalization. TRPIDA_CH_3 is a ligand comprising a thio-amide groups which creates a high affinity for its reactivity with metal. In Figure 4.9, the synthesized AuNPs are first capped with citrate molecules via the electrostatic attraction of the positive AuNPs surface with the negative end of citrate to create a stable layer thus preventing aggregation. However, the citrate can easily be replaced on the surface of AuNPs by a thio-amide group of the TRPIDA_CH_3 ligand as shown in Scheme 4.1. Though the TRPIDA_CH_3-AuNPs are very stable at room temperature, upon the addition of highly labile Cr(VI), TRPIDA_CH_3 is picked up by chromium cation leaving less capping on the surface of AuNPs, leading to aggregation. The change in UV-Vis spectra of the TRPIDA_CH_3-AuNPs upon addition of different concentrations of Cr(VI) solutions ranging from 0.01 to 100.0 µM are depicted in Scheme 4.1.

4.1.5 Selectivity and sensitivity of the sensor

4.1.5.1 The CIE approach

Nine possible interfering ions (Cr, Cu, Fe, Ni, Zn, Pb and Mn) were investigated. Other metal ions were tested using the same optimal conditions to understand the selectivity of the colorimetric method toward Cr(VI). The investigated interfering metal ions with the concentration of 40 µM did not interfere with the detection process as shown in Figure 4.10 (a and b). An apparent change in colour occurred for Cr(VI) detection. All the metal ions could not induce the aggregation of TRPIDA_CH_3-AuNPs except for Cr(VI), meaning that the sensor is only selective to Cr(VI). In the presence of all the metal ions (mixed ions, as seen in Figure 4.10 (a and b) TRPIDA_CH_3-AuNPs remained stable. However, significant change was observed when 40 µM was added to a solution of TRPIDA_CH_3-AuNP. Therefore, a conclusion was drawn that even at high concentration of 40 µM, the metal ions had no interference on the detection of Cr(VI).

(a)

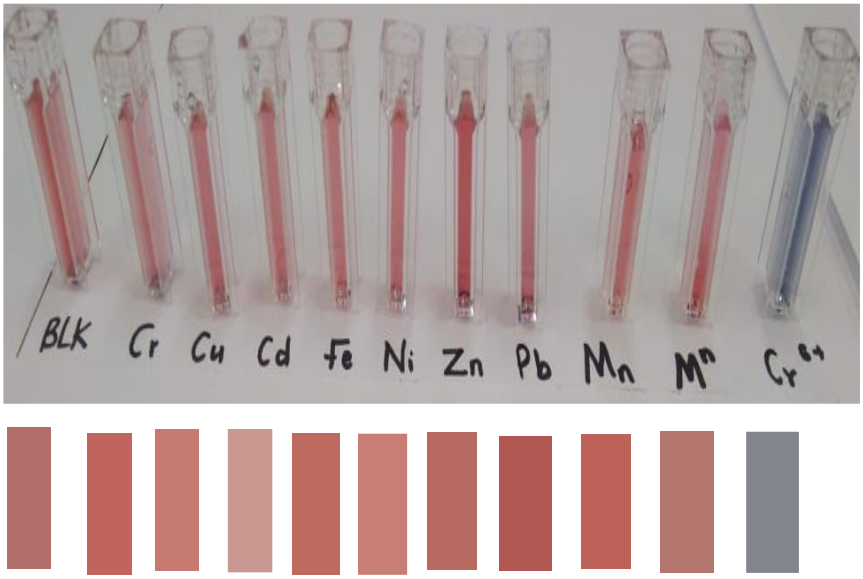

(b)

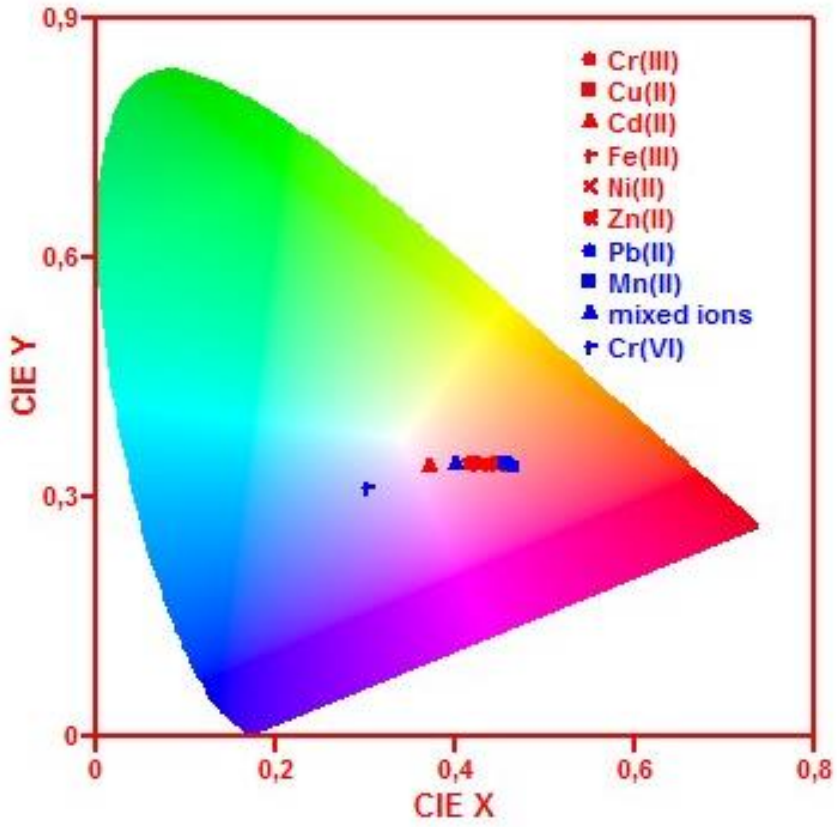

Figure 4.10: (a) Photograph image of colorimetric response of interfering metal ions and Cr(VI) at different concentrations and (b) chromaticity image of interfering metals and Cr(VI).

4.1.5.2 The Spectrophotometric approach

An apparent change in the absorption peak was observed for Cr(VI) detection system as shown in Figure 4.11 (a). The investigated interfering metal ions did could not induce the aggregation of TRPIDA_CH_3-AuNPs except for Cr(VI), meaning that the sensor is only selective to Cr(VI) hence only a single absorption peak at 520 nm was observed for the interfering metal ions. A peak at 645 nm wavelength was observed when 40 µM Cr(VI) was added to the TRPIDA_CH_3-AuNPs representing the aggregation of the TRPIDA_CH_3-AuNPs. Furthermore, the absorbances recorded at 520 and 645 nm wavelength for each metal ion was represented graphically Figure 4.11 (b) to compare the selectivity of the TRPIDA_CH_3-AuNPs sensor. A conclusion was drawn that the sensor is only selective to Cr(VI) due to the high absorbance observed only on Cr(VI).

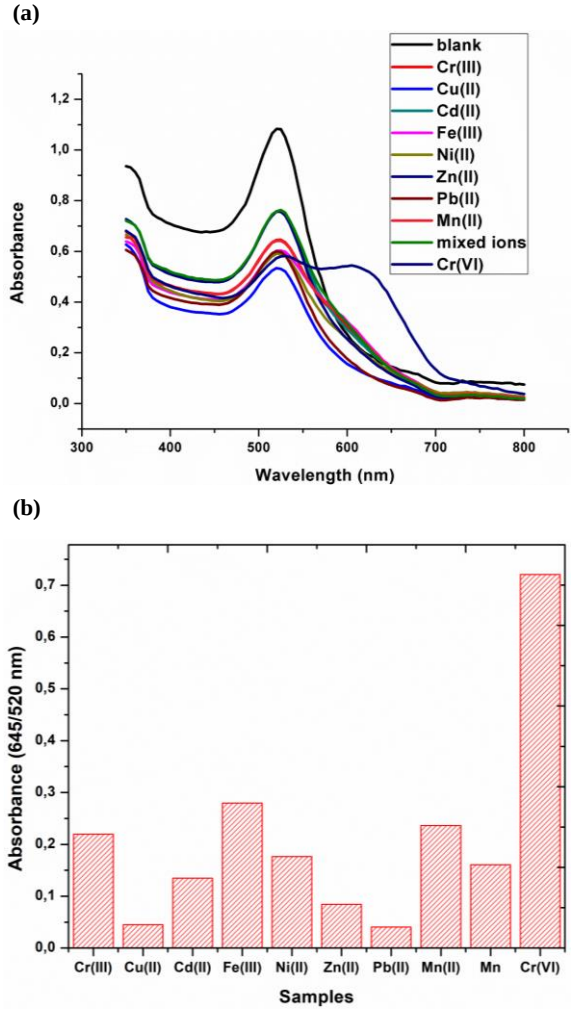

Figure 4.11: (a) UV-Vis spectra of the blank of the proposed sensor in the presence of interfering metal ions and Cr(VI) and (b) bar graph showing responses of interfering metal ions.

Over the range of 0.01-100 µM a satisfying linear relationship y = 0.0111 x + 0.1748 with the correlation coefficient of 0.987 was obtained Figure 4.12 (a). The limit of detection was 0.1423 µM, calculated by 3σ/S (where σ= standard deviation of the response; S= slope of the calibration curve). This confirmed that the sensor had excellent sensitivity. Based on the results above, it is apparent that the employed colorimetric method exhibited satisfying results in the selectivity of Cr(VI). Additionally, a comparison between the spectrophotometric approach and a CIE approach was conducted to validate if the CIE approach is reliable. The measured absorbances obtained were used to calculate the exact molarity of each Cr(VI) standard using the linear equations. The exact molarity was then represented graphically against the prepared concentration of Cr(VI) Figure 4.12 (b). A slight difference was noted for each method approach, but they were almost the same. Therefore, a conclusion was drawn that both method approaches are sensitive on the detection of Cr(VI).

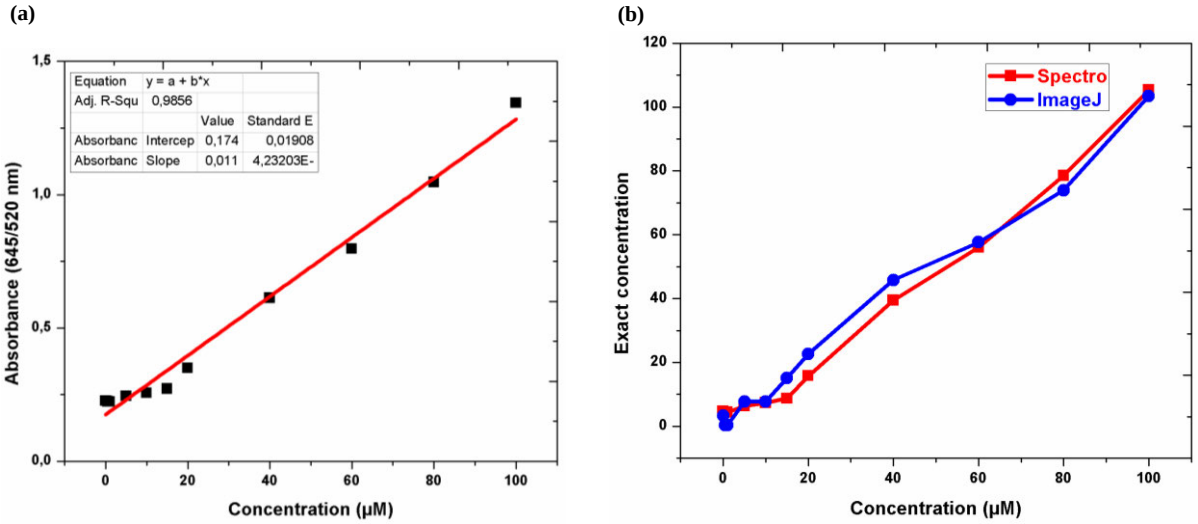

Figure 4.12: (a) Graph of absorbance at 645/520 nm wavelength *vs.* concentration of Cr(VI) TRPIDA_CH_3-AuNPs (blank) 0.01-100 µM and (b) representative plots of exact concentration *vs* prepared concentration of Cr(VI) TRPIDA_CH_3-AuNPs (blank) 0.01-100 µM.

4.1.6 Practical application

4.1.6.1 The CIE approach

The image processing was conducted for the recovery studies with real water samples. The colours presented in Figure 4.13 (a) are corresponding with chromaticity results studied at Figure 4.13 (b). At 20 µM a blue colour is observed from the photograph image in Figure 4.13 (a) which is also observed in the chromaticity diagram at the blue region at this particular concentration, thus, a blue colour is noticed in the photograph image at 100 µM for the standard as well as the real water samples, hence, all the points are on the blue region in Figure 4.13 (b).

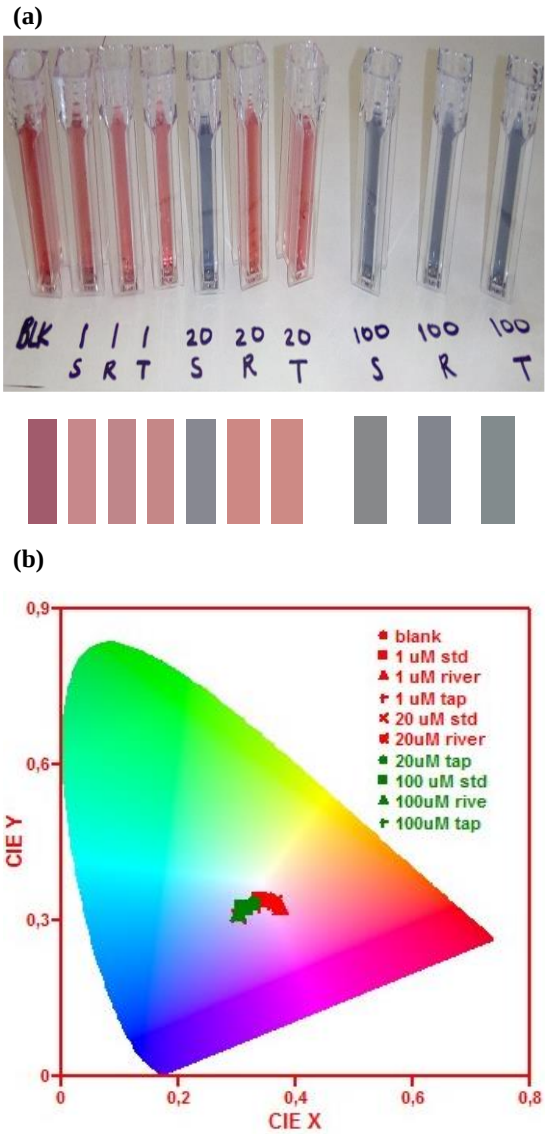

Figure 4.13: (a) Colorimetric scheme with corresponding calculated mean RGB values, (b) chromaticity image of Cr(VI) standards and real water samples

4.1.6.2 The Spectrophotometric approach

The domination of the blue colour at 20 µM standard and 100 µM standard and spiked water samples is depicted by the red shift at 645 nm wavelength in Figure 4.14. Meanwhile, no colour change was observed at the 1 µM standard and spiked water samples and at 20 µM spiked water samples. Hence, a peak absorption at 520 nm. Overall, the results in Figure 4.14 validated the created colorimetric scheme using RGB colour coordinates reported in Figure 4.13 (a and b).

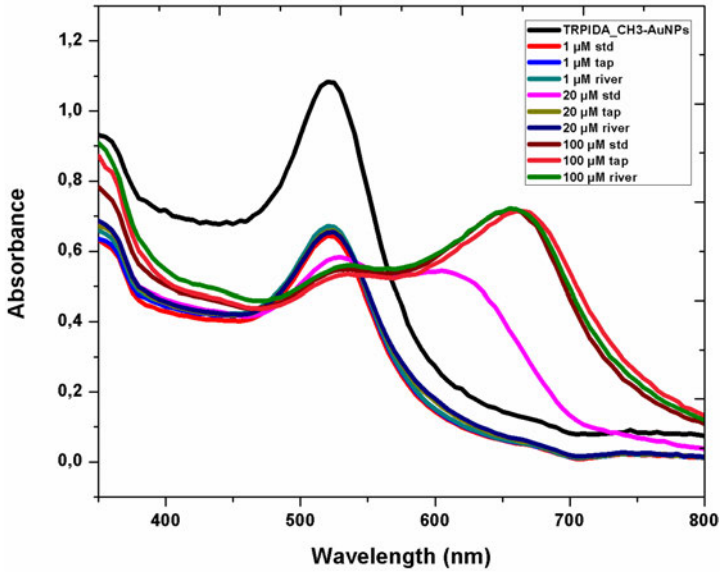

Figure 4.14: UV-Vis spectra of Cr(VI) standards and real water samples.

The method was further tested on tap and river water to evaluate its practical applications. The recovery values of spiked tap water samples with different concentrations, shown in Table 4.2, were in the range of 72.63-100.09 %, with a much lower recovery for the 20 µM spiked sample. Recovery values of 72.13-99.86 % with RSD values of 0.1-0.3 % were obtained for spiked river water samples with three different concentrations of Cr(VI) as presented in Table 4.2. These results clearly demonstrated that the developed colorimetric method was potentially applicable for the detection of Cr(VI) in real water samples.

Table 4.2: Showing recovery values of spiked Cr(VI) in tap and river water samples and the relative standard deviation (RSD) values of each sample (n=3)

Sample	Spiked (µM)	Detected	Recovery (%)	RSD (%)
Tap water	1	1.0009	100.09	0.02
	20	14.5262	72.63	0.01
	100	99.9158	99.92	0.01
River water	1	0.9918	99.18	0.02
	20	14.4266	73.13	0.03
	100	99.8602	99.86	0.02

4.1.7 Application of optimized conditions in wastewater effluent samples

4.1.7.1 The CIE application

The collected wastewater effluent samples photographic images were analyzed for the detection of Cr(VI). The filtered effluent samples and the effluent samples with TRPIDA_CH_3-AuNPs images were analyzed using ImageJ software and the obtained RGB values were used to make the Fills corresponding the colours in Figure 4.15 (a) and (b), respectively. A change in colour from red to blue was observed on day 1,5, 7, 9 and 10 in Figure 4.15 (b). All the colorimetric data obtained is presented below in Table 4.3 and 4.4, respectively. Furthermore, a quantitative analysis of was conducted using the optimized spectrophotometric method to quantify the Cr(VI) content present in each wastewater effluent sample.

(a)

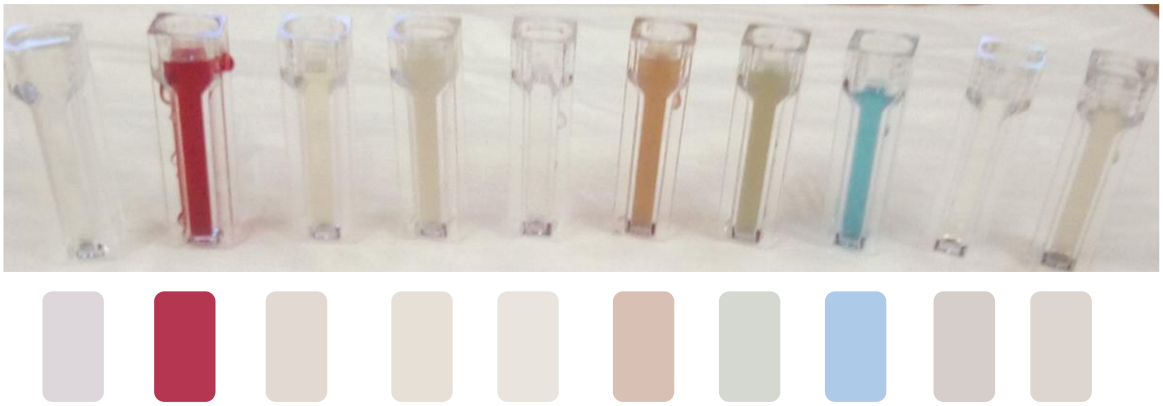

(b)

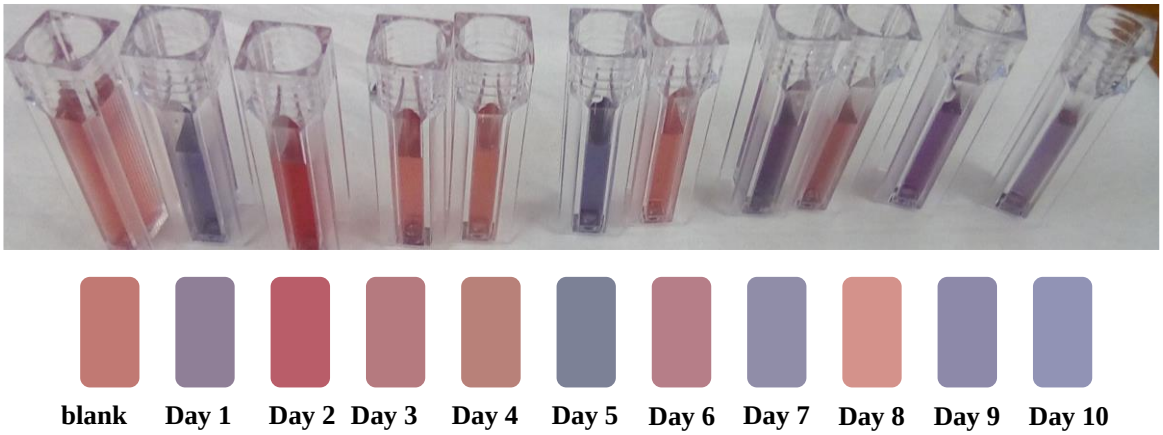

Figure 4.15: (a) Photograph image of filtered wastewater effluent samples from Day 1-10 and (b) photograph image of wastewater effluent from Day 1-10 and TRPIDA_CH_3-AuNPs (700:300 µL) as blank.

4.1.7.2 The spectrophotometric approach (TRPIDA_CH_3-AuNPs method)

Colorimetric assay based on the colour properties of TRPIDA_CH_3-AuNPs was conducted for Cr(VI) in the concentration range of 0.01–100 µM. An observation was made that wine red colour of the TRPIDA_CH_3-AuNPs started to diminish as the Cr(VI) increased in Figure 4.16 (a). A sharp and significant peak due to the successful formation of AuNPs functionalized with TRPIDA_CH_3 was observed at 520 nm, represented as blank in Figure 4.16 (b). A significant change was observed upon addition of 20,40, 60, 80 and 100 µM Cr(VI) solutions to TRPIDA_CH_3-AuNPs solutions. An additional broad peak appeared at 645 nm. The colorimetric assay in Figure 4.16 (a) and the UV–Vis spectra in Figure 4.16 (b) were in corresponding.

(a)

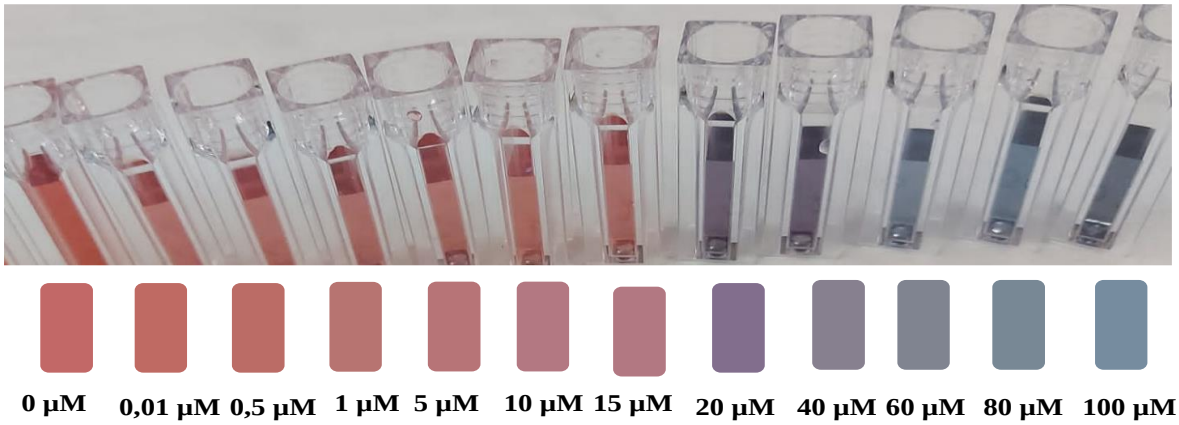

(b)

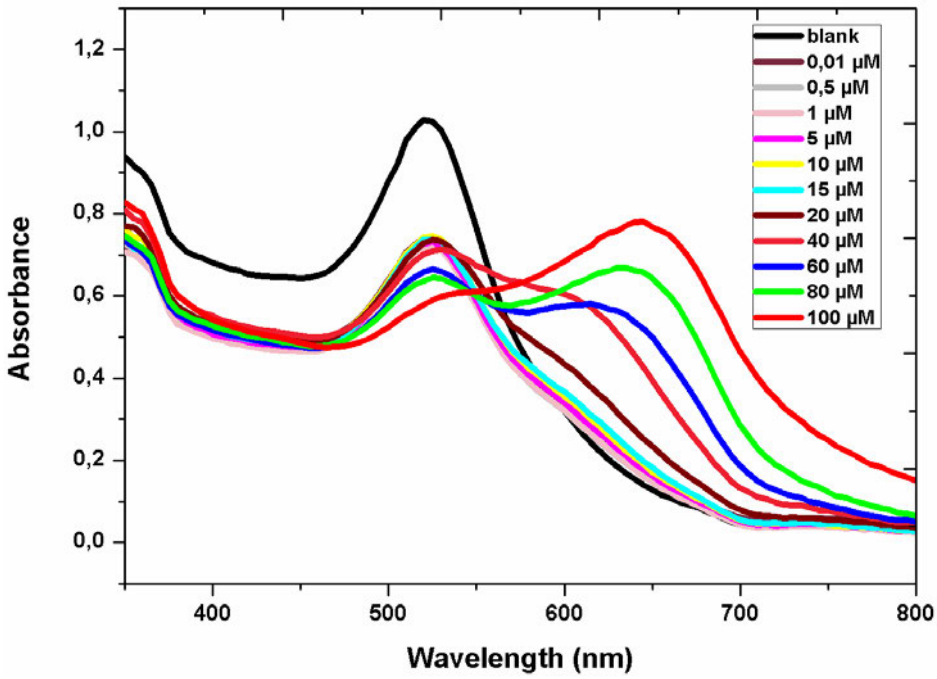

Figure 4.16: a) Photograph images of the TRPIDA_CH_3-AuNPs in the presence of different concentrations of Cr(VI) in the range of 0.01-100 µM and (b) UV–Vis spectra of the TRPIDA_CH_3-AuNPs after the addition of different concentrations of Cr(VI) in the range of 0.01-100 µM.

The calibration curve of the absorbances ratio recorded at 520 and 645 nm gave a linear equation y = 0.01047x + 0.10119 and R^2 = 0.94942 in Figure 4.17 (a). A linear regression analysis was conducted to evaluate the validity of the calibration results using a residual error Figure 4.17 (b). It is evident that the residual errors are randomly distributed with no apparent trend toward either smaller or larger residual errors, suggesting that a weighted straight-line regression is more appropriate. The LSPR absorption bands demonstrated by the transformation behaviour of TRPIDA_CH_3-AuNPs and calibration curve displayed that the developed sensor is efficient in the concentration range of 0.01-100 µM. This equation was then used to calculate the concentration of the collected effluent wastewater samples.

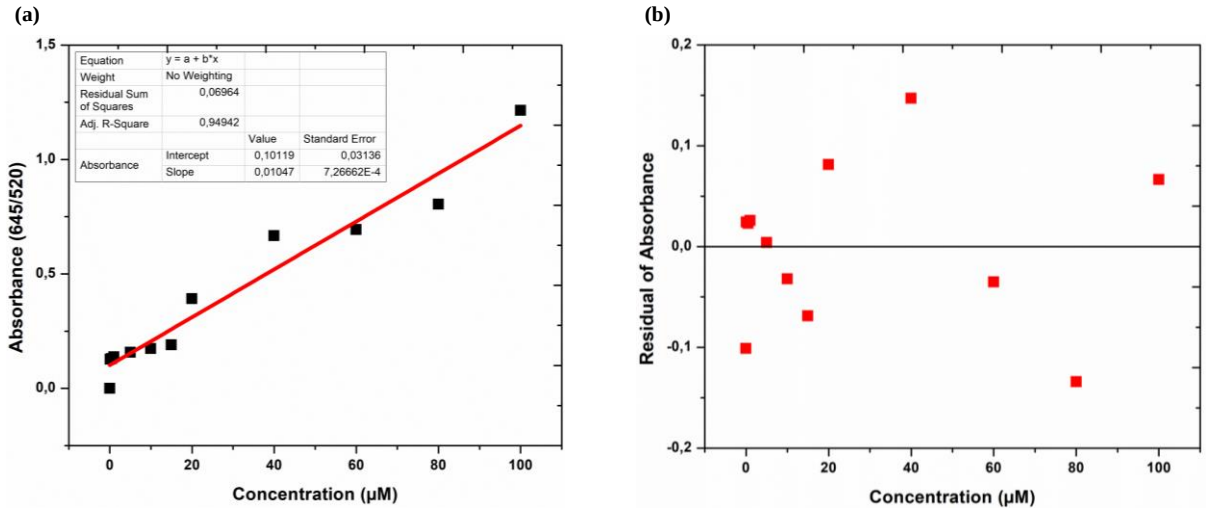

Figure 4.17: (a) Plot of absorbance @ 645/520 nm versus the concentrations of Cr(VI) in the range of 0.01–100 µM and (b) residual plot of absorbance against concentration

4.1.7.3 The Spectrophotometric approach (DPC method)

Colorimetric sensing of hexavalent chromium with DPC produced a pale reddish-violet colour in acidic solutions in Figure 4.18 (a) and the absorbance was measured in triplicate at 540 nm using a UV-Vis Spectrophotometer. Plot of absorbance at 540 nm against concentration in the range of 10-100 µg/L yielded a straight calibration curve with a linear regression equation y = 0.0013x – 0.005 and R^2 = 0.9955 in Figure 4.18 (b). The residual errors are randomly distributed in Figure 4.19 (c) and the effluent samples will be treated likewise. The concentration of Cr(VI) will be calculated using the linear regression equation.

(a)

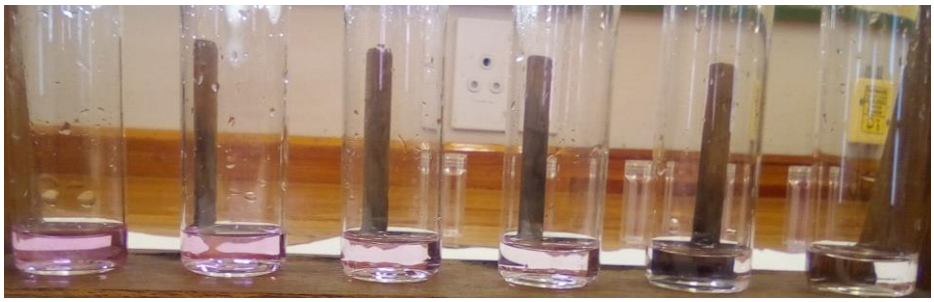

100 µg/L **80 µg/L** **60 µg/L** **40 µg/L** **20 µg/L** **10 µg/L**

(b)

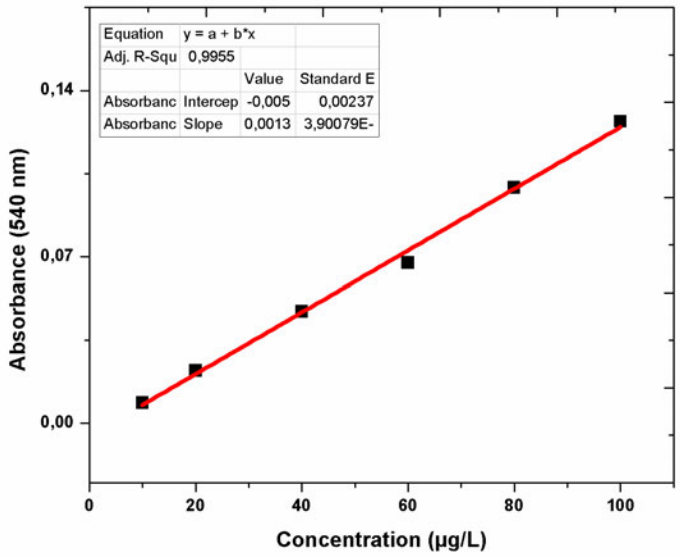

(c)

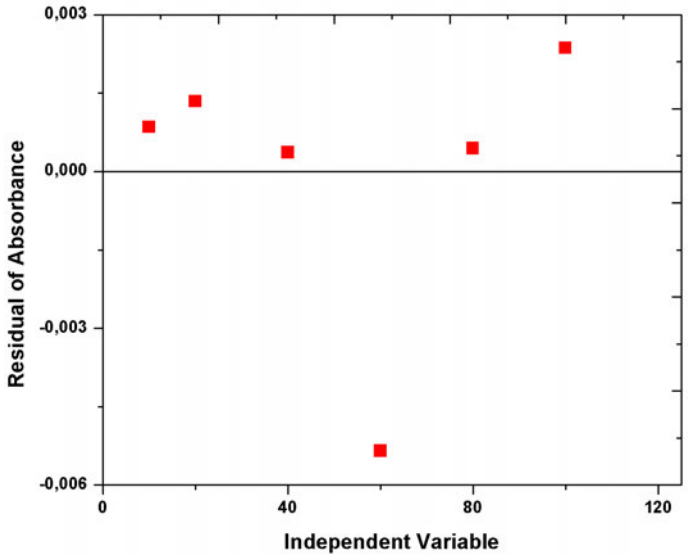

Figure 4.18: (a) Photographs of DPC in the presence of different concentrations of Cr(VI) in the range of 10-100 µg/L, (b) Plot of 540 nm *vs* the concentrations of Cr(VI) in the range of 10–100 µg/L and (c) residual plot of absorbance against concentration.

4.1.8 Colorimetric sensing of wastewater effluent samples

The colorimetric detection of Cr(VI) represented by the photographic image in Figure 4.15 (b) shows that there was a wine red colour of the TRPIDA_CH_3-AuNPs which is the blank to a blue colour for effluent sample Day 1, 5, 7, 9 and 10, respectively. Meanwhile, no apparent colour change was observed on sample Day 3, 4, 6 and 8, respectively. However, a deep red colour was observed only on sample Day 2. Additionally, the photograph image of the real wastewater effluent sample is presented in Figure 4.14 (a) for a clear indication of how the samples were before they were added to the TRPIDA_CH_3-AuNPs colorimetric sensor for further analysis. Furthermore, the above-mentioned results were supported by the UV-Vis LSPR spectra and colorimetric assay detection of Cr(VI) in the samples by TRPIDA_CH_3-AuNPs as presented in Figure 4.19. An intense peak was observed at 520 nm on Day 2 sample which was even higher than the peak intensity of the blank sample in Figure 20. This could be due to the deep intense colour observed in Figure 4.15 (b). A decrease in intensity of LSPR peaks were observed on Day 1, 5, 8 and 9 at 520 nm wavelength and a formation of the new LSPR peaks appeared at 645 nm wavelength.

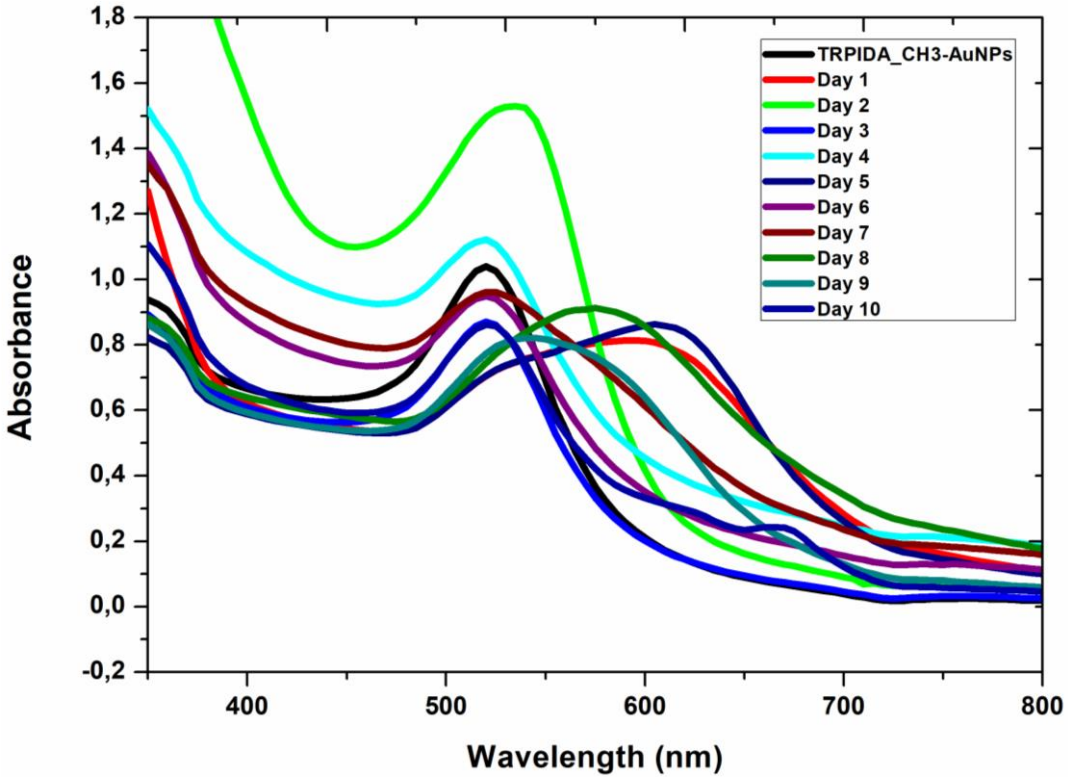

Figure 4.19: UV–Vis absorption spectra of TRPIDA_CH_3-AuNPs after the addition of wastewater effluent samples from Day 1-10.

4.1.9 Application of CIEL*a*b* to wastewater effluent samples

The RGB values for the colorimetric image of Cr(VI) detected in wastewater effluent using TRPIDA_CH_3-AuNPs colorimetric sensor in Table 4.3 were analysed using ImageJ software. The R values decreased in Table 4.3 for the blue coloured samples in Figure 4.16 (a) and almost constant at Day 2, 3 and 4, respectively. The G and B values followed the same trend for almost all the samples with B values higher that G values except for the blank and Day 4 and they were the same value at Day 8.

Table 4.3: Showing colorimetric data obtained from photographic images of effluent wastewater samples.

Days	Actual wastewater									
	R	**G**	**B**	**x**	**y**	**L**	**a***	**b***	**Hue**	**Chroma**
1	221	215	207	0.32	0.34	86.25	0.67	4.66	1.15	4.71
2	181	54	81	0.50	0.30	42.85	52.69	13.85	3.72	54.48
3	226	217	210	0.32	0.34	87.22	1.88	4.53	-1.12	4.90
4	231	224	214	0.32	0.34	89.47	0.67	5.73	-0.87	5.76
5	233	229	222	0.32	0.34	91.07	0.14	2.87	-0.43	2.88
6	217	192	181	0.32	0.34	7.9	7.08	8.77	0.34	11.27
7	213	216	207	0.32	0.34	85.89	-2.62	4.07	-0.02	4.84
8	174	202	233	0.27	0.29	80.25	-2.59	-18.43	0.90	18.61
9	214	206	203	0.32	0.33	83.31	2.24	2.46	0.51	3.33
10	221	214	208	0.32	0.34	86.02	1.36	3.80	-2.82	4.04

Table 4.4: Showing colorimetric data obtained from photographic images of effluent wastewater samples and TRPIDA_CH_3-AuNPs as a blank

Days	Wastewater samples + TRPIDA_CH_3										
	R	**G**	**B**	**x**	**Y**	**L**	**a***	**b***	**ΔE_{Lab}**	**Hue**	**Chroma**
blank	193	121	115	0.41	0.34	58.27	27.42	15.12	0.00	1.63	31.31
1	127	136	156	0.31	0.29	56.61	1.12	-11.75	37.64	-0.55	11.80
2	185	93	105	0.43	0.31	50.88	38.26	10.50	13.92	3.55	39.68
3	181	122	127	0.48	0.32	57.34	23.72	6.68	9.26	3.46	24.64
4	184	129	121	0.39	0.34	59.23	20.18	12.85	7.64	1.35	23.92
5	124	129	150	0.29	0.29	54.23	2.74	-11.89	36.81	-0.40	12.20
6	182	126	136	0.37	0.32	58.64	32.16	3.37	12.68	9.51	32.33
7	144	141	168	0.29	0.29	59.71	6.72	-13.80	35.60	0.53	15.35
8	179	169	168	0.39	0.34	70.03	3.41	1.79	29.87	1.72	3.85
9	141	137	169	0.29	0.28	58.43	8.23	-16.34	36.85	0.44	18.29
10	145	147	181	0.28	0.28	61.85	6.59	-17.94	39.24	2.25	19.11

4.1.10 Analysis of wastewater effluent samples

The developed TRPIDA_CH_3-AuNPs colorimetric sensor by Muthwa *et al.* (2020) was applied in the detection of Cr(VI) in wastewater effluent samples. The TRPIDA_CH_3-AuNPs sensor was calibrated for the analysis with Cr(VI) standards in the concentration range of 0.01-100 µM displayed in Figure 4.16 (a). Additionally, all the effluent water samples were analysed without any further dilution. Effluent samples were collected from ETP for ten operational working days and were labelled Day 1 – 10. The results obtained using the TRPIDA_CH_3-AuNPs colorimetric sensor were compared with the results obtained using a DPC conventional method to double check the efficiency of the colorimetric sensor. Average absorbances and concentration (n=3) of Cr(VI) detected using both methods are displayed in Table 4.5. Traces of Cr(VI) were detected for both methods on Day 1, 5 and 9 and were 0.8987, 0.5662 and 0.6341, respectively. Furthermore, higher amounts of Cr(VI) were detected for both methods on Day 2, 4 and 6 and were 24.3270, 15.8444 and 21.5934, respectively. were detected in the ETP dam samples in ppb concentrations, from Day 1 to Day 10, these concentrations were found to be 35, 8, 6, 38, 22, 15, 44, 43, 55 and 18 ppb, respectively. The concentration of Cr(VI) obtained using both methods are presented in a bar graph Figure 4.20 and both methods almost displayed similar results.

Table 4.5: Showing TRPIDA_CH_3-AuNPs and DPC method results the detection of Cr(VI) in wastewater effluent samples.

Days	TRPIDA_CH_3 method		DPC-method		
	Absorbance (@645/520 nm)	**Concentration (µM)**	**Absorbance (@ 540 nm)**	**Concentration (µg/L)**	**Concentration (µM)**
blank	0.0000	0.0000	0.0000	0.0000	0.0000
1	0.1847	0.8956	0.0484	41.2564	0.7935
2	0.4448	24.3268	1.4681	1133.3077	21.7960
3	0.2398	5.8560	0.2915	228.2051	4.3889
4	0.3507	15.8440	1.3216	1020.5897	19.6282
5	0.1811	0.5659	0.0089	10.8718	0.2091
6	0.4145	21.5920	1.5138	1168.4359	22.4716
7	0.2200	4.0710	0.3405	265.9487	5.1148
8	0.2453	6.3518	0.4376	340.5897	6.5503
9	0.1818	0.6316	0.0274	25.1026	0.4828
10	0.2292	4.8971	0.2782	217.9744	4.1921

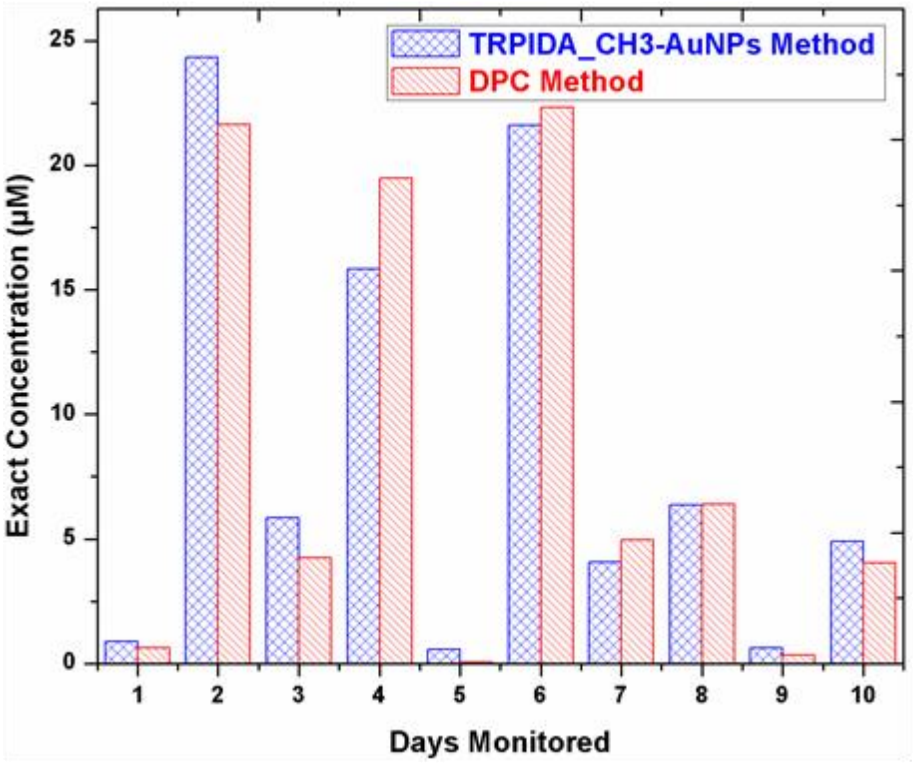

Figure 4.20: Bar graph showing exact concentration of Cr(VI) detected in wastewater effluent using the TRPIDA_CH_3-AuNPs and DPC method over a period of 10 days**.**

4.1.11 Statistical analysis or wastewater effluent samples

The obtained colorimetric detection results of Cr(VI) presented in Table 4.5 were statistically analysed to ensure there was no significant difference between the results from the TRPIDA_CH_3-AuNPs sensor method and the conventional DPC method. This was achieved by using a paired student's t-test, which outlines there was no significant difference between the two methods in Table 4.6 as $t_{exp} < t_{crit}$. The F-Test Two Sample for Variance results displayed in Table 4.7 obtained suggested that, we reject the null hypothesis and accept the alternative hypothesis since $F_{exp} > F_{crit}$. This suggested that there was a difference between the two methods variances.

Table 4.6: t-Test: Paired Two Sample for Means

	TRPIDA_CH_3-AuNPs Method	**DPC Method**
Mean	9.349316337	9.272117719
Variance	79.79835084	83.98059689
Observations	9	9
Pearson Correlation	0.980955948	
Hypothesized Mean Difference	0	
Df	8	
t Stat	0.130048372	
P(T<=t) one-tail	0.449869341	
t Critical one-tail	1.859548038	
P(T<=t) two-tail	0.899738683	
t Critical two-tail	2.306004135	

Table 4.7: F-Test Two-Sample for Variances

	TRPIDA_CH_3-AuNPs Method	**DPC Method**
Mean	9.349316337	9.272117719
Variance	79.79835084	83.98059689
Observations	9	9
df	8	8
F	0.950199853	
P(F<=f) one-tail	0.472088293	
F Critical one-tail	0.290858219	

CHAPTER FIVE

CASE STUDY II

5.1 Development of a Smartphone and spectrophotometric based systems for colorimetric detection of hexavalent chromium using 1,5-diphenylcarbazide functionalized gold nanoparticles supported by CIE L*a*b*/Yxy colour space and molecular dynamics.

5.1.1 Sensitivity of the response of DPC-AuNPs to Cr(VI)

The digital image from Color Grab and the change in the colours of the DPC-AuNPs upon the addition of Cr(VI) standards solutions in the concentration range of 0.5-50.0 µM is presented in Table 5.1 and Figure 5.1 (a). The colour change of the DPC-AuNPs induced by Cr(VI) was monitored using the smartphone Color Grab App and UV–Vis spectrophotometry. This observation was further confirmed with UV spectrophotometer which showed two well separated peaks at 520 and 670 nm as shown in Figure 5.1 (b). The colour scheme represented by the photograph image in Figure 5.1 (a) was created by incorporating the resultant mean RGB values recorded for each calibration standard into the colour developer using the computer desktop colour application. The created colour pattern for the Cr(VI) standards matched the colours of the solutions. ImageJ software was used to analyse the colour coordinates between the reaction of DPC-AuNPs and Cr(VI) for image processing. A photograph image Figure 5.1 (a) was uploaded to the ImageJ application software to properly expose the colour shades and their corresponding intensities in the form of RGB values. TEM results image in Figure 5.1 (c) showed that the synthesised gold nanoparticles were monodispersed with a diameter of around 14 nm.

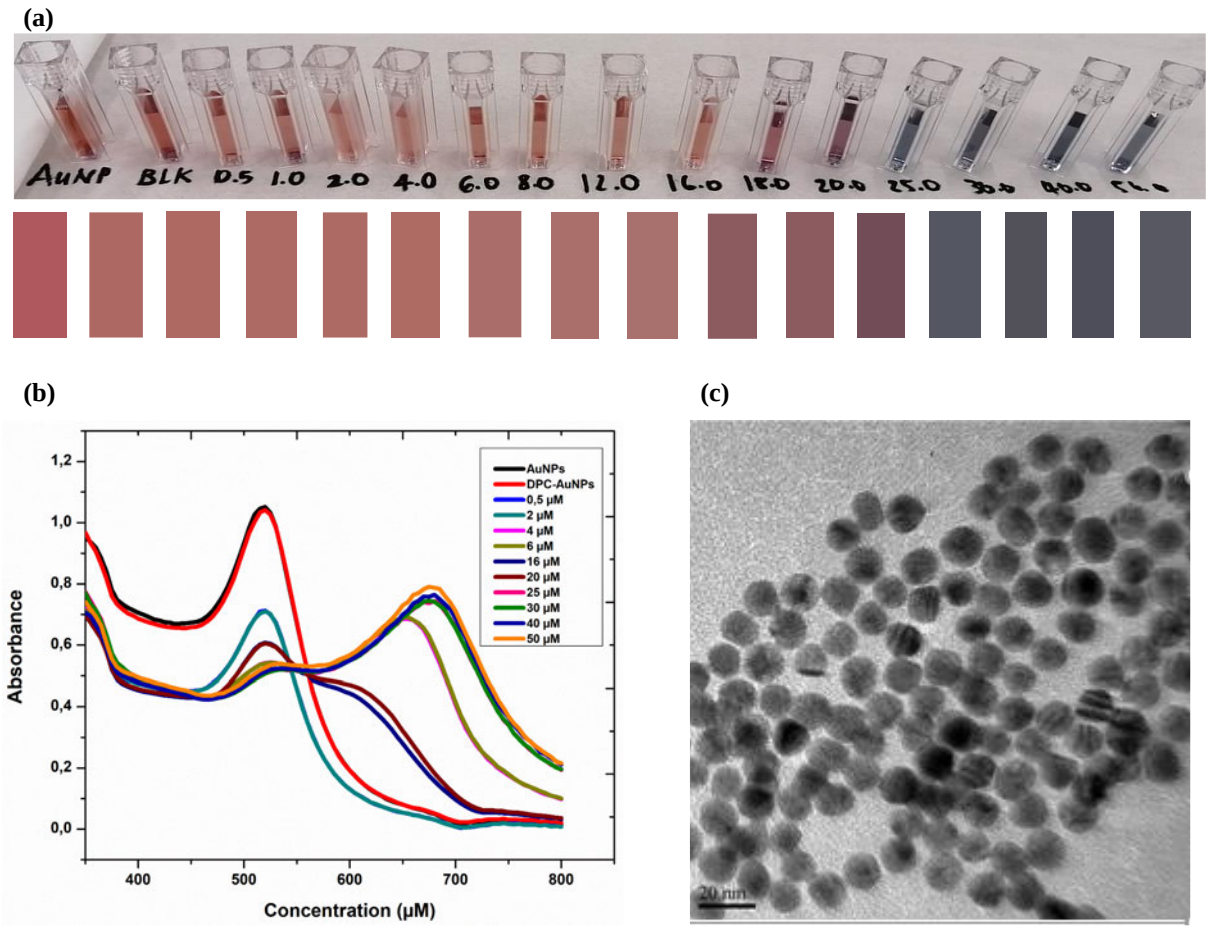

Figure 5.1: (a) Photograph image of the DPC-AuNPs blank and different concentrations of Cr(VI) in the range of 0.5-50.0 µM, (b) concentration-dependent extinction spectra of the DPC-AuNPs blank and different concentrations of Cr(VI) in the range of 0.5-50.0 µM and (c) TEM image of AuNPs sample at 20 nm scale

Results obtained from the Color Grab as shown in Table 5.1, indicated that upon the addition of different concentration of Cr onto DPC-AuNPs, there was a change in colour from red to blueish which is associated with the change of the dielectric environment of the surface of gold nanoparticles. A Further observation of the change upon increasing the concentration of Cr(VI) was observed from the UV-Vis spectra that the addition of 20 µM Cr(VI) led to a slight red shift to 670 nm wavelength and this is confirmed in Table 5.1 with the immediate change in colour which is again confirmed by the increased of the green from the RBG obtained to 187. The result of the Color Grab for 20 µM Cr(VI) was converted into an observable colour using the RGB values, this generated a clear violet colour which confirmed that an increase in the Cr(VI) concentration over 20 µM led to a second peak at 670 nm wavelength and a parallel decrease in the intensity of the SPR peak at 520 nm was observed as shown in Figure 5.1 (b).

Thus, the colour of the DPC-AuNPs changed from wine-red to blue as the Cr(VI) concentration increased Figure 5.1 (a).

Table 5.1: Showing photograph images of the DPC-AuNPs blank and different concentrations of Cr(VI) in the range of 0.5-50.0 µM, captured by smartphone using Color Grab.

Cr (VI) concentrations on DPC-AuNPs (µM)	**Color Grab image**	**RBG Values**			**Colour from RBG**
		R	**B**	**G**	
0	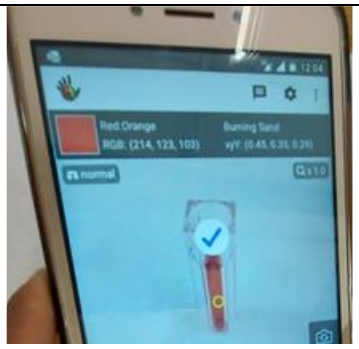	214	123	103	
0.5	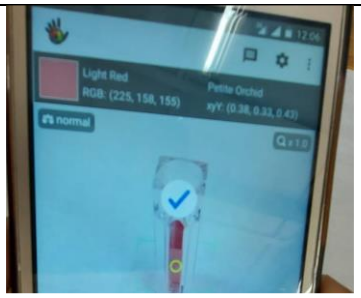	225	158	155	
2	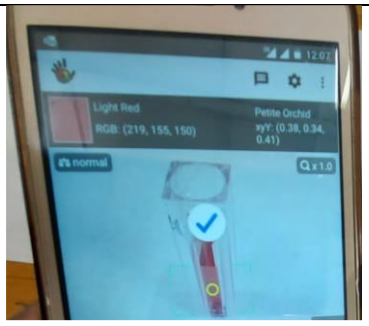	219	155	150	
4	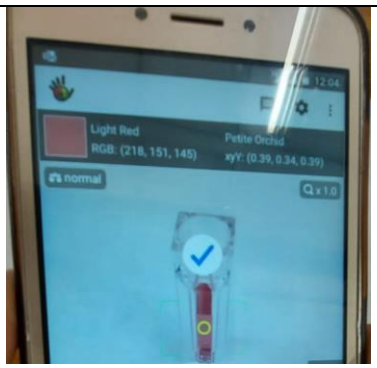	218	151	145	

6	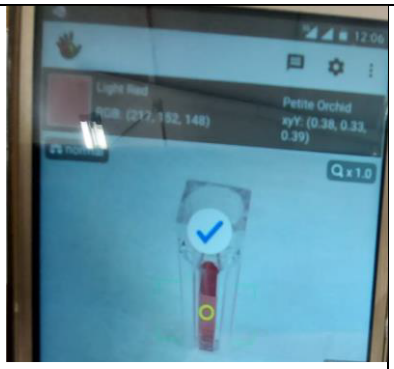	217	152	148	
16	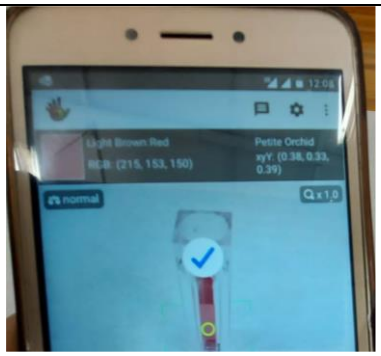	215	153	150	
20	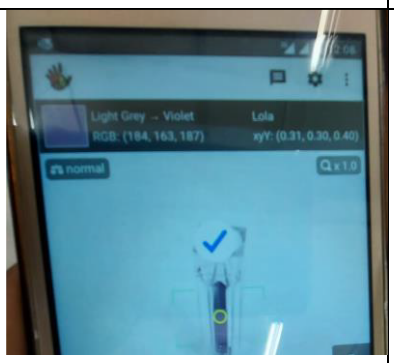	184	163	187	
25	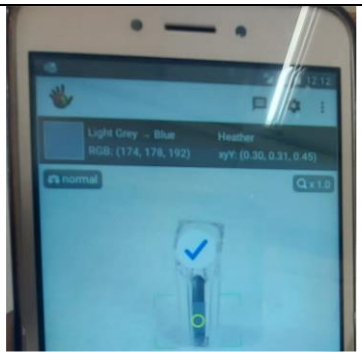	174	178	192	
30	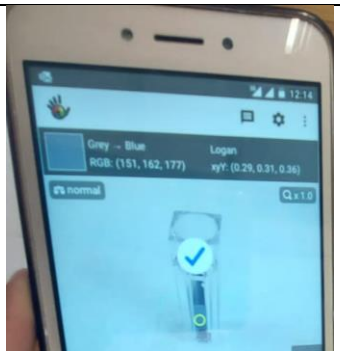	151	162	177	

40	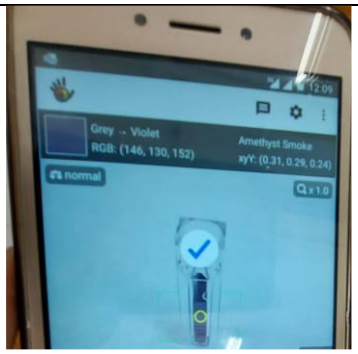	146	130	152	
50	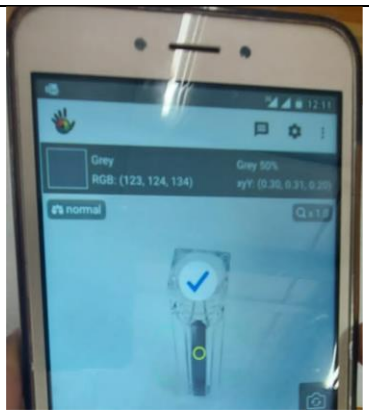	123	124	134	

5.1.2 Image analysis using RGB colour coordinates and CIE La*b*/Yxy colour system.

A scale ranges from 0-255 in the standard RGB which represented each of the three colour coordinates for the red, green and the blue region were obtained from Color Grab as shown in Table 5.1. The RBG values from Color Grab analysis and from UV spectrophotometer were plotted as shown in Figure 5.2 (a) and Figure 5.2 (b), respectively. A significant decrease for red colour component was observed in both curves though these degrees were slightly prominent from UV spectrophotometer curve. These trends were mainly predominant as a result of increasing the Cr(VI) concentration. Meanwhile, the green and blue curves followed the same trend where a gradual increase was observed from 0-16 µM and a significant decrease from 18-50 µM to lower values of green and blue, respectively as shown in Figure 5.2 (a) and Figure 5.2 (b).

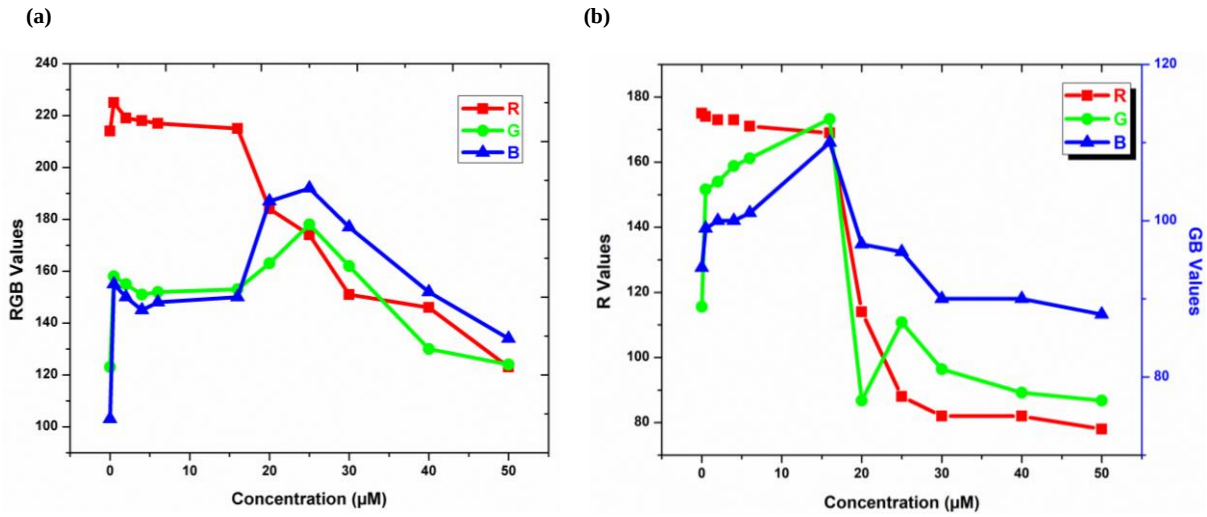

Figure 5.2: (a) RBG colour plot against the corresponding Cr(VI) concentration (Color Grab) and (b) RBG colour plot against the corresponding Cr(VI) concentration (UV spectrophotometer)

The RGB colour coordinates were then converted to the CIE L*a*b* colour space for measurement of CIE L*a*b* colour system coordinates which were used to create the chromaticity diagram. The results that are shown in Figure 5.3 (a) represent the L curve of the data that was obtained from Color Grab. It was noted that there was a gradually increase of the L values observed from 0-20 µM followed by a significant decrease from 18-50 µM suggesting the standards changed from lightness (red) to darkness (blue). Whereas, a* curve significantly decreased demonstrating that standards changed from red region (+a) to green region (–a). In a b* curve, from 0-16 µM the curve was almost constant then a significant decrease was observed from 18-20 µM indicating the colour change from red to blue, these results were in agreement with the data obtained from the UV spectrophotometer which are presented in Figure 5.3 (b).

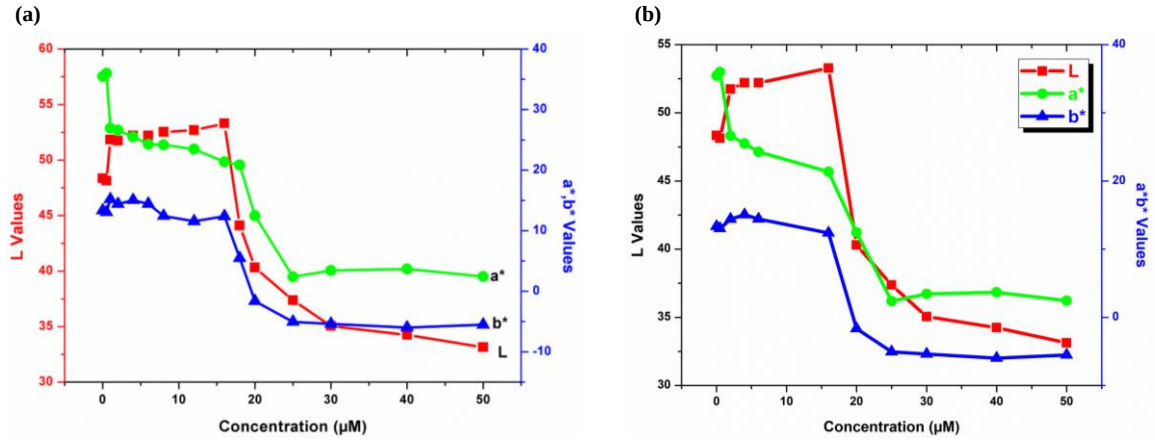

Figure 5.3: (a) Plots of L*a*b* against Cr(VI) concentration (Color Grab) and (b) plots of L*a*b* against Cr (VI) concentration (UV spectrophotometer).

5.1.3 Qualitative and quantitative analysis of the response of DPC-AuNPs to Cr (VI)

The colour difference (ΔE) was calculated using Equation 2-1 with the values of ΔL, Δa^* and Δb^* obtained from the colour produced on the calibration standards shown in Figure 5.1 (a) and Table 5.1. Figure 5.4 (a) and (b) show that the ΔE value increased significantly with increasing Cr(VI) concentration which confirmed high assay reproducibility, this incremental demonstrated by colour change is very instrumental in understanding the design of the Lovibond colour filters for detecting chromium in water. These colour changes which were measured are associated with the modulus of the distance vector between the initial colour values and the actual colour coordinates.

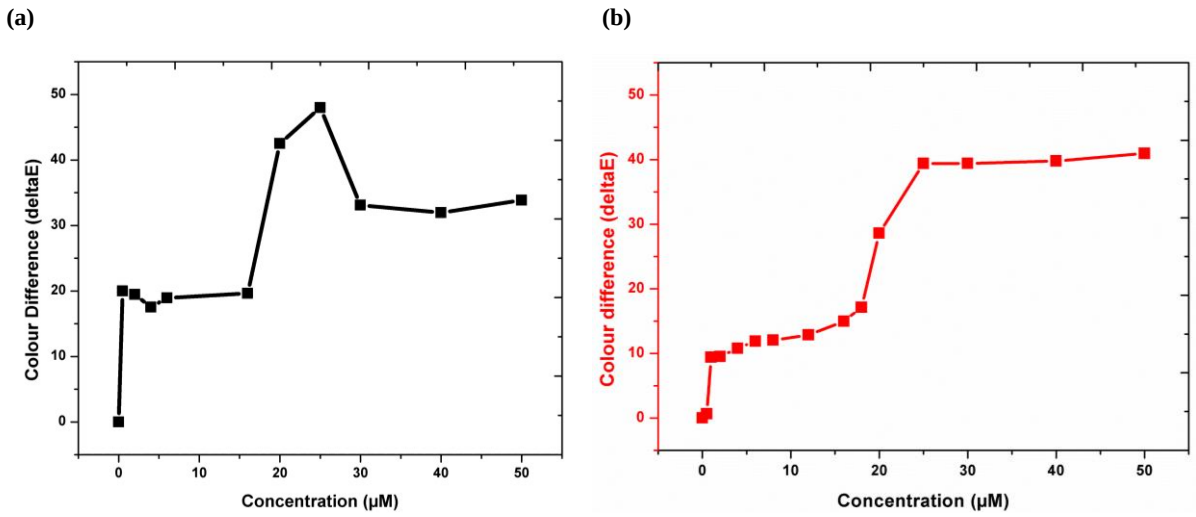

Figure 5.4: (a) Plot of colour difference against Cr(VI) concentration (Colour Grab) and (b) plot of colour difference against Cr(VI) concentration (UV spectrophotometer).

Chroma (C*) was also used as the quantitative attribute of colourfulness to determine the degree of difference of a hue in comparison to a grey colour with the same lightness. The higher chroma values were associated with high colour intensity of samples perceived by human eyes. Chroma was calculated using Equation 2-2. The chroma decreased significantly with the increase in Cr(VI) concentration up to 25 µM with a dullness of 4.260 and vividness of 35.908 in Figure 5.5 (a) and Figure 5.5 (b) for Color Grab and UV spectrophotometer data, respectively. Total colour difference and chroma was considered as the most sensitive parameter for the measurement of colour. Hue angle (h*) was considered the qualitative attribute of colour. It was used to define the difference of a certain colour with reference to grey colour with the same lightness. This attribute was related to the differences in absorbance

at different wavelengths. Hue was calculated using Equation 2-3 and the obtained values were plotted against concentration in Figure 5.5 (a) and Figure 5.5 (b) for Color Grab and UV spectrophotometer data, respectively. A significant decrease was observed for concentration of chromium ranging from 18-25 µM.

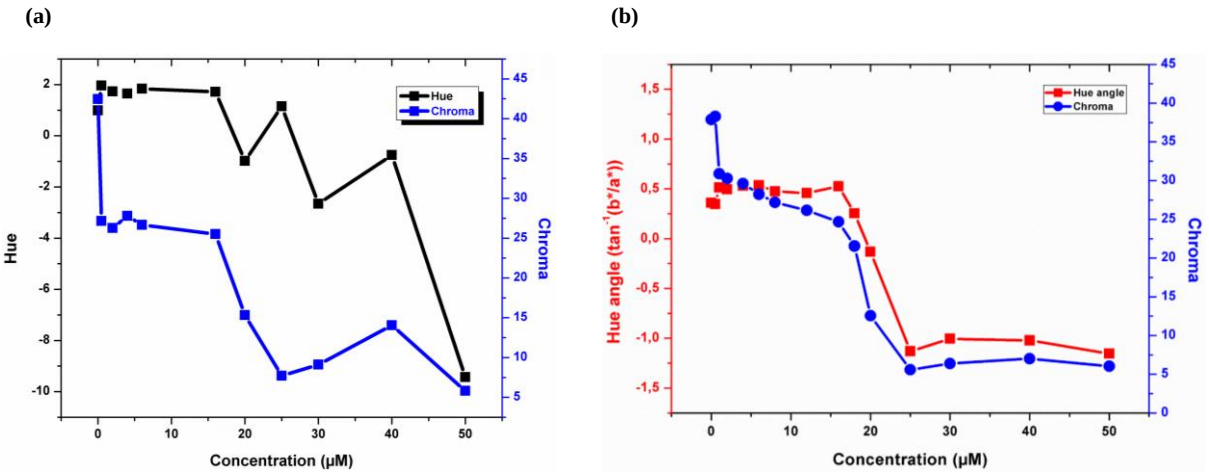

Figure 5.5: (a) Plots of hue angle and chroma values against Cr(VI) concentration (Color Grab) and (b) Plots of hue angle and chroma values against Cr(VI) concentration (UV spectrophotometer).

The final horseshoe chromaticity diagram is shown Figure 5.6 (a) for data obtained from the smartphone as well in Figure 5.6 (b) for UV spectrophotometric data. It was clearly visible from the plotted RBG point in chromaticity diagram that the increased concentration of chromium contributed to colour change from red to blue which is due to gold nanoparticle aggregation, this was explained by the colour that were shifted toward the blue region. In Figure 5.6 (a), it was noted that as the concentration of chromium was increased, the xy coordinates obtained from RBG coordinates occupied the blue region of the chromaticity diagram model, further evidence of this trend was also observed in Figure 5.6 (b) from UV spectrophotometric data.

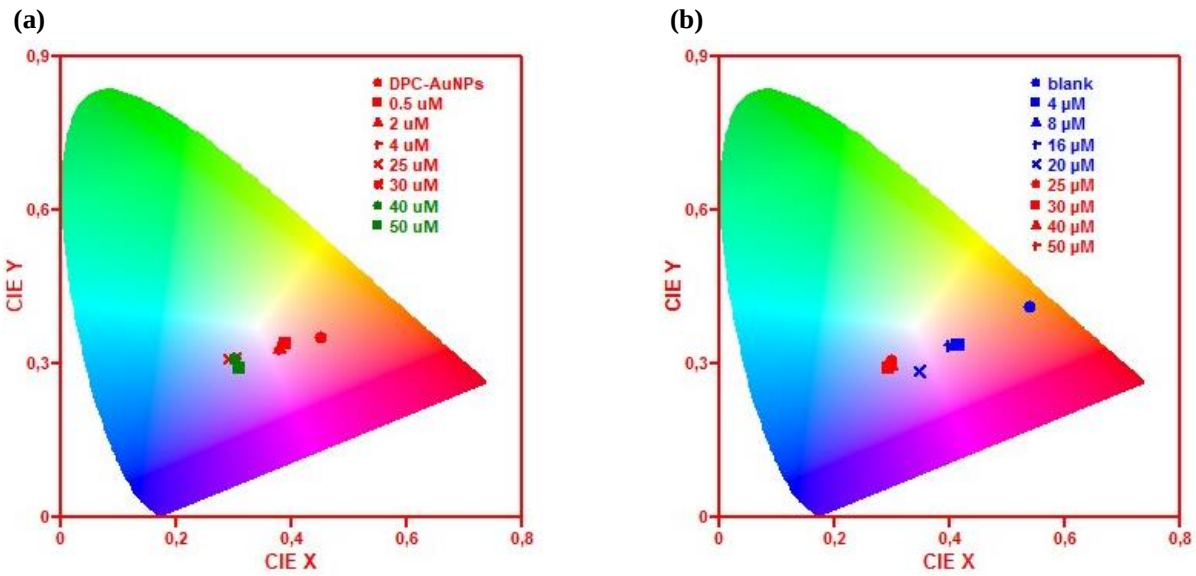

Figure 5.6: (a) Chromaticity image of calibration standards of Cr(VI) (colour Grab) and (b) chromaticity image of calibration standards of Cr(VI) (UV spectrophotometer).

5.1.4 Molecular simulation of DPC-AuNPs to Cr (VI)

The model depicting aggregation of DPC-AuNPs upon the addition of Cr(VI) is shown in Figure 5.7 (a). The charges of Cr(VI) were balanced with oxygen as shown with the red dots in Figure 5.7 (b). This figure demonstrated that upon the addition of hexavalent chromium, the aggregation was induced which could be clearly seen in Figure 5.7 (b) as compared to Figure 5.7 (a) where gold clusters are separated. The mechanism of aggregation was discussed in our published work (Magubane *et al.* 2019; Muthwa *et al.* 2020). The mechanism is due to the interaction of Cr(VI) with the capping DPC which is introduced by replacing citrate, the capping agent used during the synthesis of AuNPs. This results into the formation of Cr-DPC complex, thus leaving gold nanoparticle uncapped as result aggregation is induced as shown in Figure 5.7 (b).

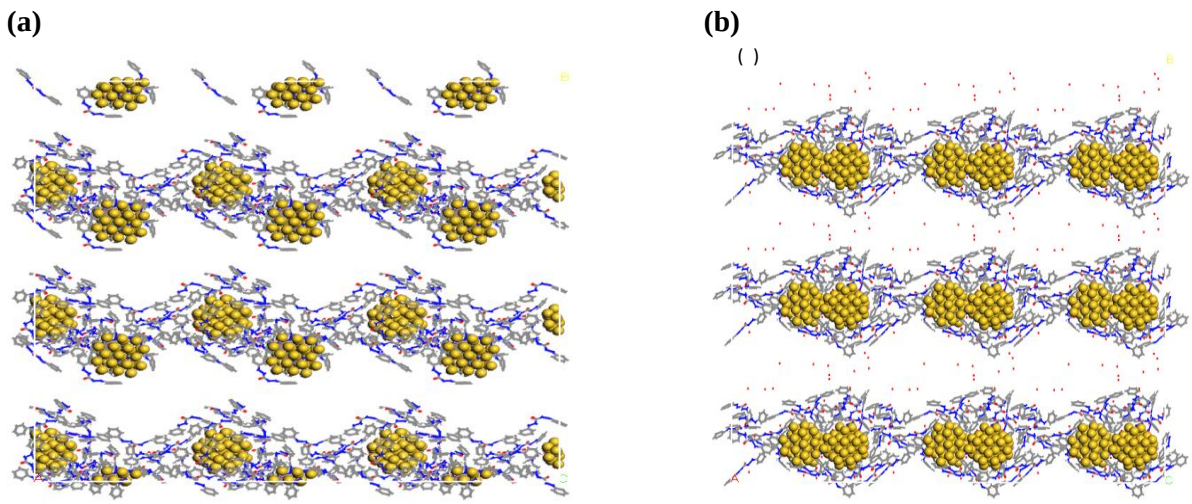

Figure 5.7: Model for simulation DPC-AuNPs and Cr (VI) (a) DPC-AuNPs and (b) Cr-DPC-AuNPs.

The simulated radial distribution functions (RDF) for different selected atoms of DPC-AuNPs and Cr(VI) were calculated to quantify interactions among the DPC groups, AuNPs, and Cr ions. The RDF provided the information regarding the intermolecular interaction among the three components (AuNPs, Cr and DPC). The peak height and the position were used for structural analysis of these interactions. The RDF of DPC-AuNPs is shown in Figure 5.8 (a). In this case, the simulation was done by interacting AuNPs with the carbonyl end of the DPC. In Figure 5.8 (b), it can be noted that the *r* (Å) at 3 Å is associated with RDF [g*(r)*] of 3.4 *r*, this is an indication of strong interaction with the surface of gold nanoparticles, where most of the DPC molecules are within 3 Å from the surface of gold nanoparticles. Further molecular simulation was done to depict the formation of new Cr-DPC complex. The formation Cr-DPC complex was simulated by looking at the bonds between Cr-N and Cr-AuNP bond formation using the radial distribution as shown in Figure 5.8 (a) and (b). A clear evident of the formation of strong Cr-N bond, leading to formation of Cr-DPC complex is evident from the radial distance from 3 Å. The height of the g(r) for Cr-AuNPs is 3.4 *r* at the radial distribution of 3 Å. Notable so, the radial distance at 3 Å for Cr-DPC bond is 8.4 *r*. It is very obvious from Figure 5.8 (c) that the radial distribution for Cr-DPC was increased by more than two folds when it is compared with the radial distribution of Cr-AuNPs. This demonstrated a clear evidence of the formation Cr-DPC complex. The formation of this complex was very crucial in understating the aggregation process of gold nanoparticles. The mechanism of this can be explained by the process that is similar to molecule exchange process, in this case gold nanoparticle are stabilized by DPC which covers the surface thus preventing aggregation. However, upon the addition of hexavalent chromium ions into the system they interact with

DPC leaving uncapped AuNPs which are likely to aggregate as attested with the simulated radial distribution functions in Figure 5.8 (a).

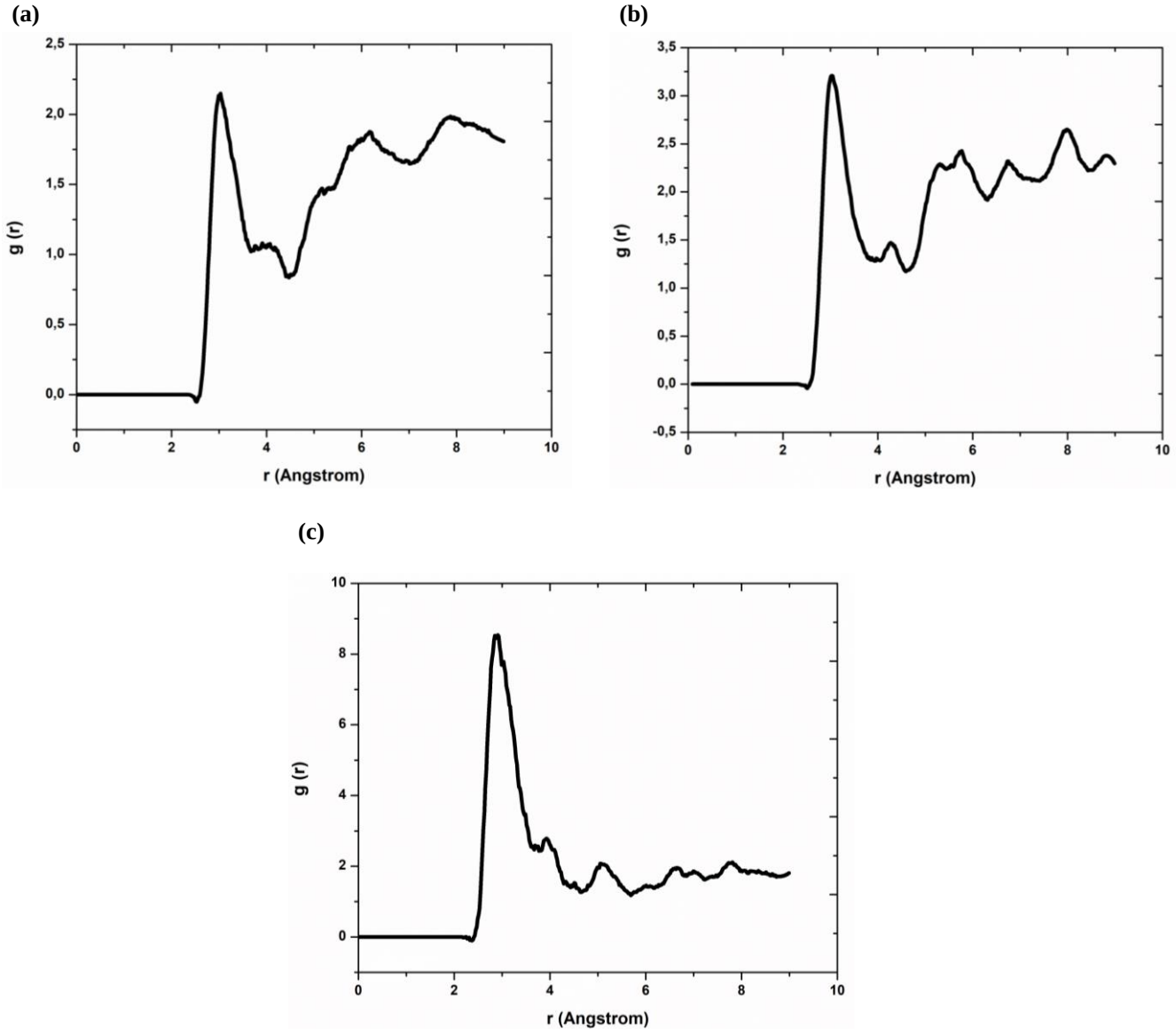

Figure 5.8: Radial distribution function for DPC-AuNPs and Cr(VI) (a) DPC-AuNPs, (b) Cr-AuNPs and (c) Cr-DPC.

CHAPTER SIX

CASE STUDY III

6.1 Understanding interaction between 1-methyl-6-phenyl-6, 7-dihydro-5H-indolo [3, 2-c] [1, 8] naphthyridine complex with silver nanoparticles and Pb(II): a CIE L*a*b*/Yxy and RGB colour coordinates study

6.1.1 Characterization of unmodified AgNPs

Well-dispersed silver nanoparticles exhibited an intense yellow colour in solution. The silver nanoparticles in aqueous solution were stable and the colour remained unchanged for at least 30 days. The unmodified AgNPs were further characterized by UV-Vis, TEM and DLS and the results are presented in Figure 6.1. The UV–Vis spectrum of the prepared AgNPs displayed a local surface plasmon resonance (LSPR) absorption with a peak maximum at 410 nm in Figure 6.1 (a). TEM results image in Figure 6.1 (b) showed that the synthesized silver nanoparticles were well dispersed in aqueous solution.

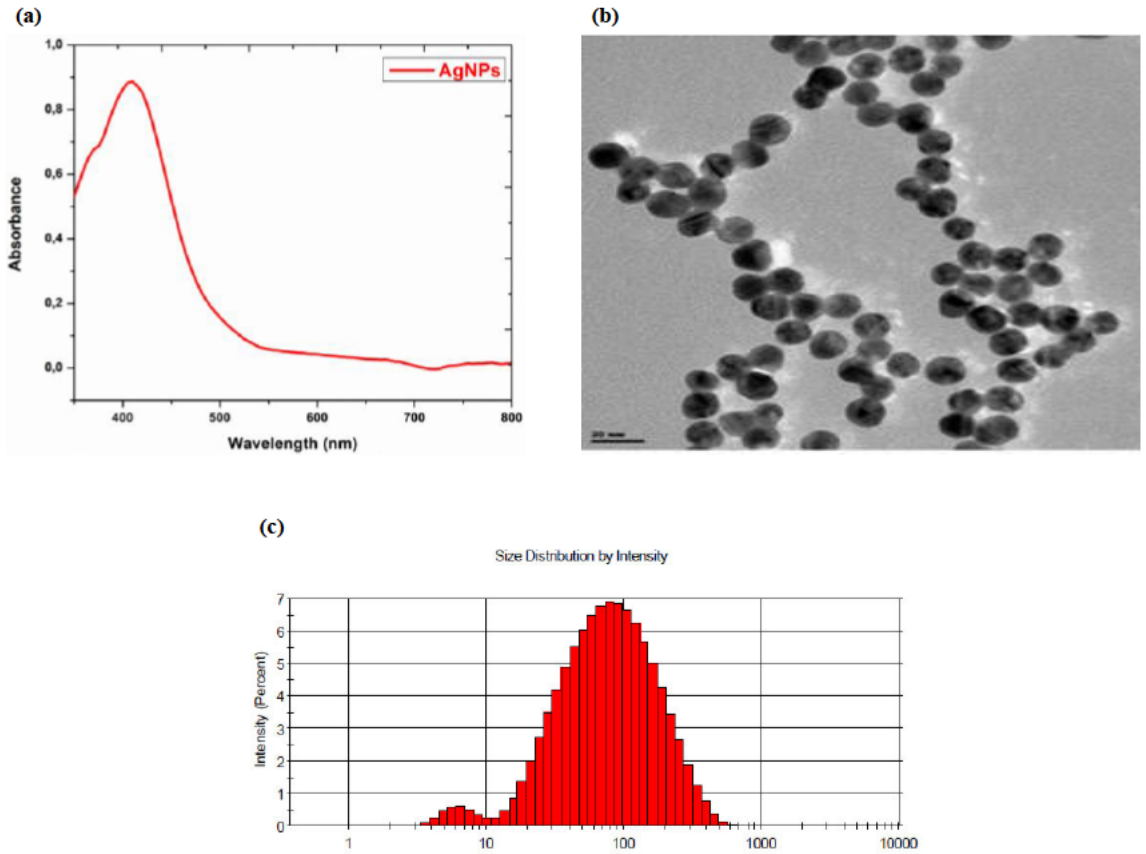

Figure 6.1: (a) UV-Vis absorption spectrum showing maxima at 410 nm, (b) TEM image of the synthesized AgNPs and (c) shows average particle distribution by DLS.

6.1.2 Characterization of 1- methyl-6-phenyl-6, 6a, 7, 11b-tetrahydro-5H-indolo [3, 2 - c] [1, 8] naphthyridine.

The characteristic absorption band in the FT-IR spectrum presented in Figure 6.2 (a) showed stretching absorptions (cm $^{-1}$) at 3390-3271 due to the secondary amine N-H stretch, C-H (sp3) stretch at 2854, C=C stretch and N-H bend at 1675- 1618, C-N stretch at 1479 and N-H out of plane bend at 744 cm $^{-1}$. The mass spectrum in Figure 6.1 (b) with a molecular ion peak at *m*/*z* 311.2 [M^+] corresponded to molecular formula $C_{21}H_{17}N_3$. Moreover, elemental analysis also confirmed the structure of TRPIDB_H compound as 1- methyl-6-phenyl-6, 6a, 7, 11b-tetrahydro-5H-indolo [3, 2 - c] [1, 8] naphthyridine.

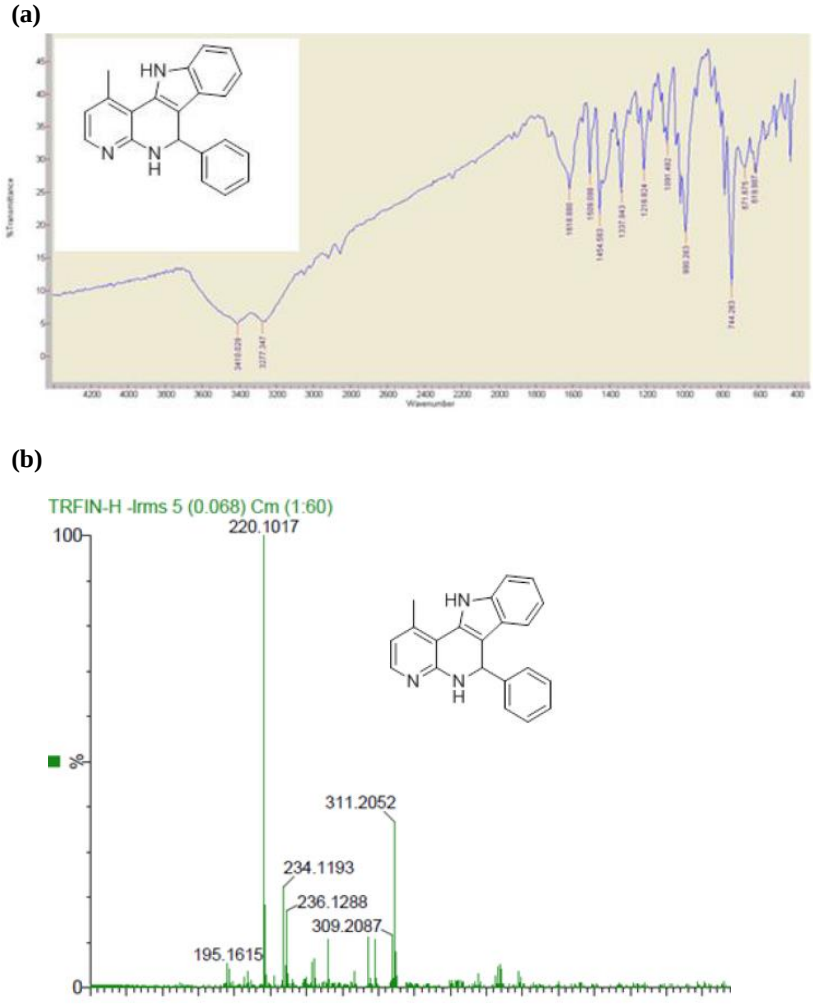

Figure 6.2: (a) IR spectrum and (b) TOF-MS spectrum for TRPIDB_H

Well distinct signal at δ 10.80 for overlapping NH-13 indole and NH-1 naphthyridine were observed in Figure 6.3 (a) in the ^{1}H NMR spectrum. The formation of a new ring was confirmed

by the aromatic protons at δ 7.39 (1H, d, *J* = 8.1 Hz, H-15) and 6.85 (1H, d, *J* = 8.1 Hz, H-14) corresponded to naphthyridine –CH whilst a signal at δ 5.87 (s, H-2) exhibited the presence of –CH (sp^3). The indole –CH was assigned by the 2 doublet at δ 7.37 (2H, d, *J* = 8.1 Hz, H-5 & H-8) and the 2 triplets at δ 7.07 (1H, t, *J* = 7.8 Hz, H-7) and 6.89 (1H, t, *J* = 7.8 Hz, H-6) were assigned to indole –CH, respectively. The phenyl ring exhibited five protons: 1 proton was triplets at δ 7.17 (1H, t, *J* = 8.2 Hz, H-4') and other 4 protons were doublets at δ 7.32 (2H, d, *J* = 8.1 Hz, H-2'& H-6') and δ 7.29 (2H, d, *J* = 7.4 Hz, H-3' & H-5') as shown in Figure 6.3 (a). The ^{13}C NMR in Figure 6.3 (b) spectrum showed the presence of 12 CH carbons at δ 39.7 (C2), 111.1 (C8), 118.0 (C14), 118.2 (C6), 120.9 (C7), 123.5 (C5), 125.8 (C4'), 127.9 (C2' & C6'), 128.4 (3' & C5') and 138.4 (C15). While, 8 quaternary carbons resonated at δ 111.4 (C3a), 119.1 (C12a), 128.2 (C4a), 131.0 (C11a), 136.6 (C9a), 138.4 (C1') and 144.9 (C13 & C16a).

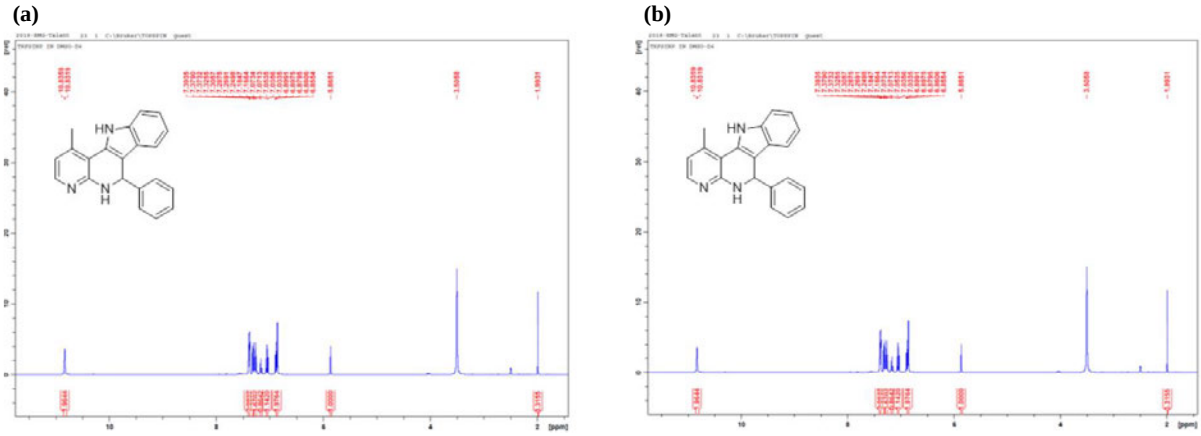

Figure 6.3: ^{1}H NMR spectrum and (b) ^{13}C NMR spectrum for TRPIDB_H

6.1.3 Characterization of TRPIDB_H-AgNPs aggregation

The photographic image and UV-Vis spectra of silver nanoparticles functionalized with 1-methyl-6-phenyl-6, 6a, 7, 11b-tetrahydro-5H-indolo [3, 2 - c] [1, 8] naphthyridine incubated with various concentrations Pb(II) standard solutions in the range of 1-100 mg/L are shown in Figure 6.4 (a) and (b), respectively. As observed in Figure 6.4 (a) the TRPIDB_H-AgNPs dispersion solution colour changed from yellow to reddish brown with increasing concentration from 60-100 mg/L. The absorption peak at 520 nm decreased and a new absorption peak emerged at 505 as the Pb(II) concentration increased as shown in Figure 6.4 (b) from the corresponding UV-Vis spectra which originated from the aggregation of AgNPs.

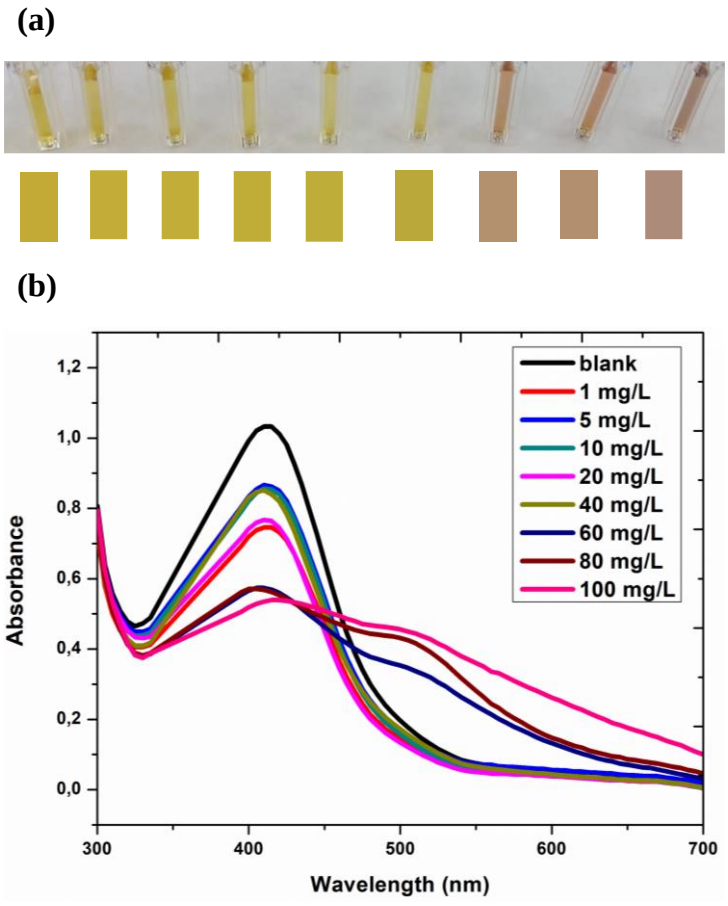

Figure 6.4: (a) Photographic image of TRPIDB_H-AuNPs (blank) in the presence of Pb(II) and (b) UV-Vis spectra of TRPIDB_H-AuNPs in the presence of Pb(II) concentration in the range of 1-100 mg/L.

Amines with electron-rich nitrogen are reported to easily attach onto the electron deficient surface of metal nanoparticles through the coordinating interaction (Li, Du and Zhang 2014). Additionally, the nitrogen atom of amines has strong affinity to AgNPs. 1- methyl-6-phenyl-6, 6a, 7, 11b-tetrahydro-5H-indolo [3, 2 - c] [1, 8] naphthyridine (TRPIDB_H) can easily induce aggregation of AgNPs due to crosslinking effect and results in colour change of AgNPs dispersion. Hence, when the TRPIDB_H-AgNPs were well dispersed in solution, the colloid exhibited a yellow colour with an absorption peak at 410 nm in Scheme 6.1 stage 4. However, the colour changes from yellow to reddish brown as the Pb(II) concentration increased resulting in a shift of the surface plasmon absorption to 505 nm due to the aggregation of AgNPs. Scheme 6.1 illustrates the mechanism for detection of Pb(II).

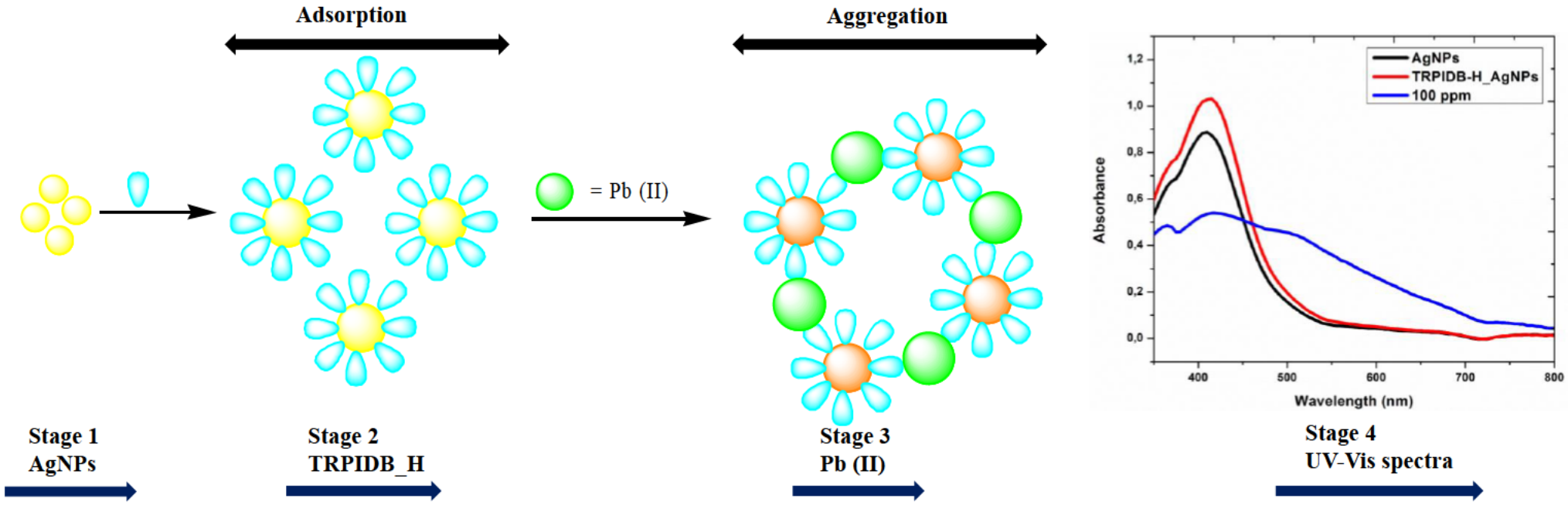

Scheme 6.1: Schematic of aggregating process of TRPIDB_H-AgNPs induced by adding Pb(II)

6.1.4 RGB colour coordinates measurements

The RGB colour coordinates are a preservative colour space and are mainly used through computer graphics as colour displays usually apply red, green and blue to create anticipated colours (Connolly and Fleiss 1997; Nxumalo 2019). The main purpose for the development of RGB colour space was the replication of human visual system. This colour model festers the colour of a photographic image into three RGB colour components which were used to create colour fills inserted in Figure 6.4 (a) to validate the obtained RGB values with the naked eye colorimetric colours. The RGB colour intensity analysis was conducted by using the captured photographic image in Figure 6.4 (a) snapshots of the colour histograms for each Pb(II) standard solution. A significant decrease in the red and green line was observed in Figure 6.5 with an increase in in Pb(II) concentration. Meanwhile, the blue line increased rapidly with an increase in Pb(II) concentration as shown in Figure 6.5.

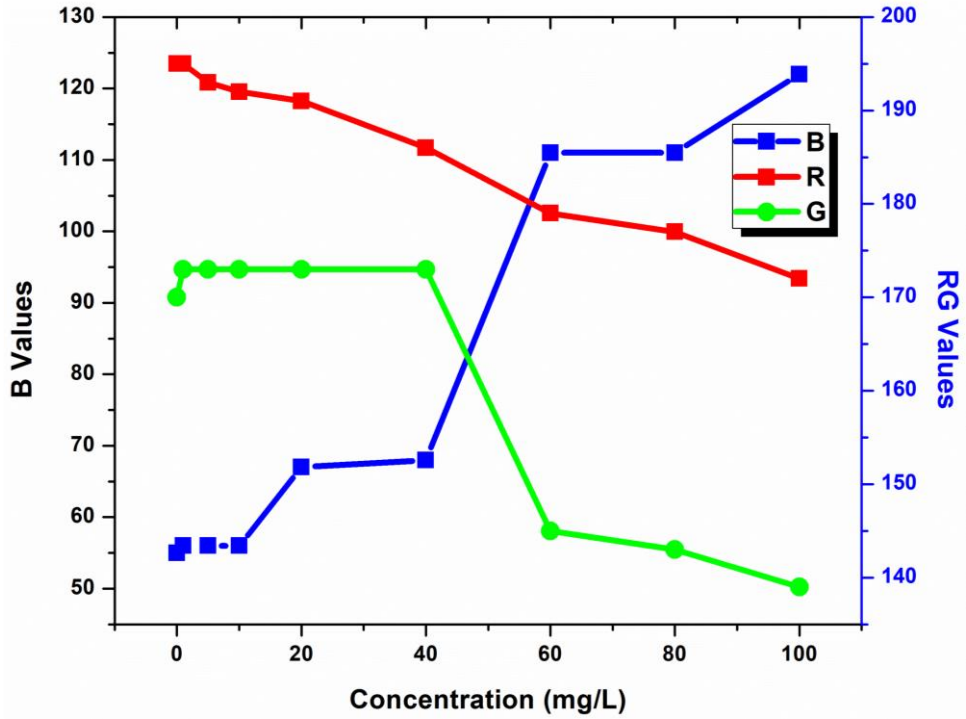

Figure 6.5: Plot of RGB colour coordinates vs concentration of Pb(II) in the range of 1-100 mg/L.

6.1.5 Optimization of CIE L*a*b* colour space

The CIE L*a*b* colour space is the first clear relationship between colours visualized by the human eye and the electromagnetic spectrum (Tauler *et al.* 1994; Nxumalo 2019). CIE L*a*b* colour space was adopted internationally on the 1970's for the main purpose of colour acceptability decision making from colour measurements by spectrophotometers and colorimeters. The colour device dependent RGB colour coordinates were converted to a standard device independent CIE L*a*b* colour space. The RGB values were then converted to L*a*b* values using Hunterlab (http://colormine.org/convert/rgb-lab/hunterlab) to obtain the corresponding L*a*b* values. A significant decrease in the L line was observed in Figure 6.6 as the Pb(II) concentration increase, indicating that the Pb(II) standard solutions lightness decreased with increasing Pb(II) concentration. Additionally, another significant decrease in the b* line was observed as the Pb(II) concentration increased in Figure 6.6 which was due to the yellow colour of the TRPIDB_H-AgNPs. Finally, a rapid decrease in a* values was noticed in Figure 6.6 from the blank (TRPIDB_H-AgNPs) to 40 mg/L yielding -a* indicating that these solutions were yellow in the presence of Pb(II) concentration. This was followed by a rapid increase in a* values yielding +a* values indicating that the solution changed colour from 60-100 mg/L to reddish brown.

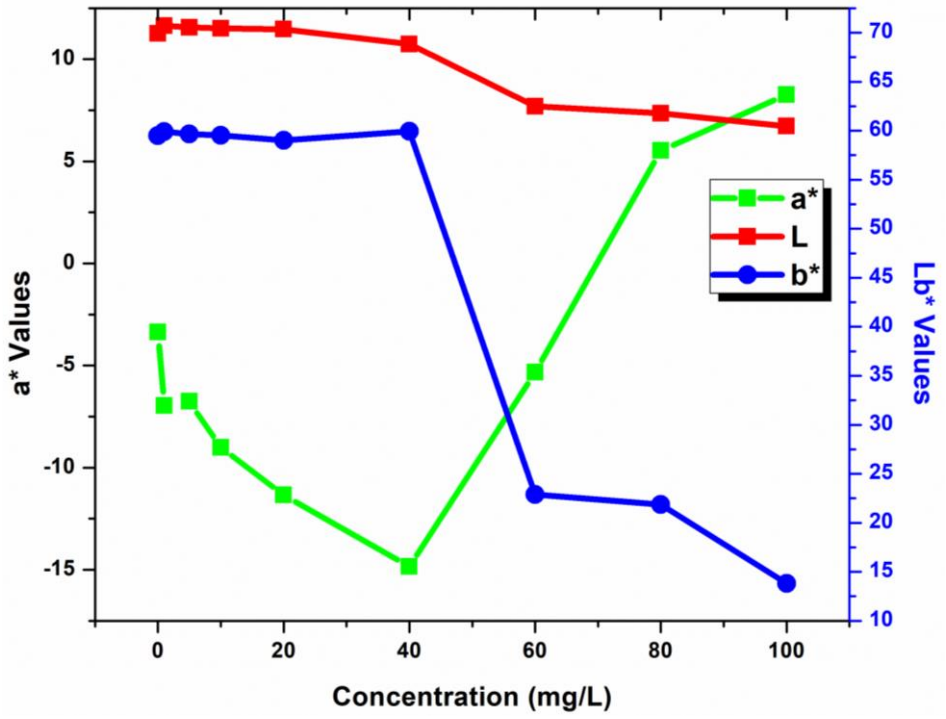

Figure 6.6: Plot of CIEL*a*b* values vs concentration of Pb(II) in the range of 1-100 mg/L.

6.1.6 Intensity and colour difference analysis

Further to the abovementioned analysis the photographic image was processed for the intensity. The colour intensity was obtained drawing a rectangle to the cuvette. The measure, analysis tabs were selected from the ImageJ software application toolbars. The obtained results for the colour intensity are shown Figure 6.7 (black line). The intensity increased from the blank to 20 mg/L followed by a rapid decrease from 40-100 mg/L in Figure 6.7 (black line). The total colour difference between the two colours is given in terms of L, a* and b* by the CIE 1976 formula (Hill, Roger and Vorhagen 1997; Mokrzycki and Tatol 2011) Equation 2-1. It was noticed that the colour difference gradually increased from the blank to 40 mg/L in Figure 6.7 (blue line) followed by a rapid increase from 60-100 mg/L.

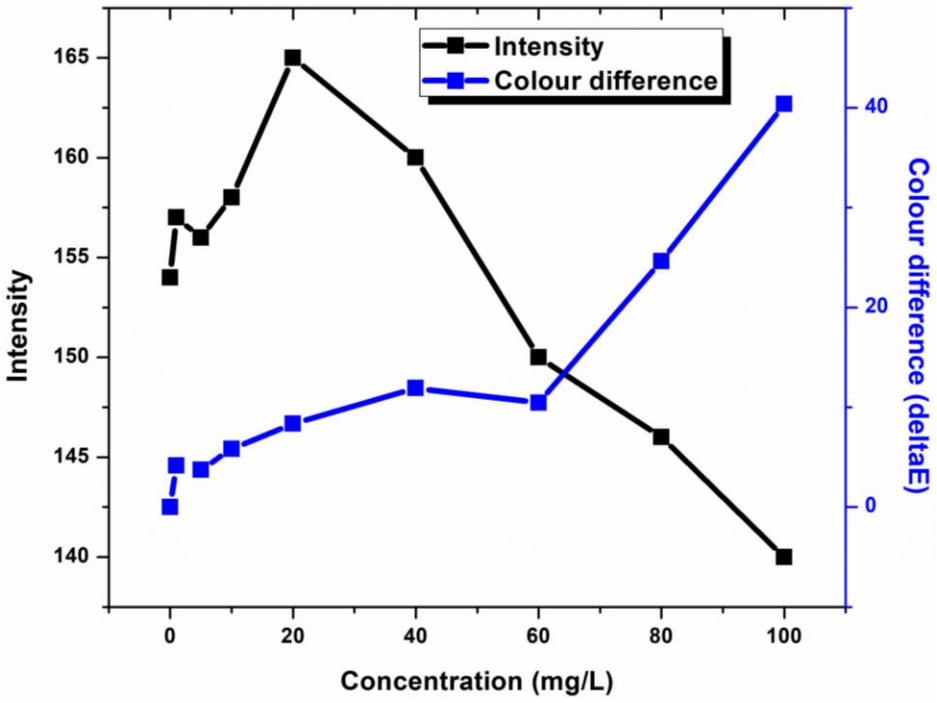

Figure 6.7: Plot of colour intensity *vs* concentration of Pb(II) *black line and plot of colour difference *vs* concentration of Pb(II) (blue line)

6.1.7 Hue and chroma evaluations

Hue angle is the basic unit of colour and was used to outline the difference of a certain colour with reference to gray colour with the same lightness. Hue angle was considered the qualitative characteristic of colour and was related to the differences in absorbance at different wavelengths. Hue was calculated using Equation 2-3 and the obtained values were plotted against concentration in Figure 6.8 (black line). No specific trend was observed for the hue in Figure 6.8 (black line). However, a significant decrease was observed from 1-10 mg/L and from 40-60 mg/L, respectively, as the Pb(II) concentration increases. This was followed by an increase in hue from 60-100 mg/L as the Pb(II) concentration increased. Moreover, chroma was used to determine the degree of difference of a hue in comparison to a gray colour with the same lightness as the quantitative attribute of colourfulness. Chroma was calculated using Equation 2-2. The higher chroma values were associated with high colour intensity of samples perceived by human eyes. The chroma decreased significantly with the increase in Pb(II) concentration, hence, the TRPIDB_H-AuNPs in the presence of Pb(II) standard solutions changed from vivid to dull as the concentration of Pb(II) standard solution increased in Figure 6.8 (blue line).

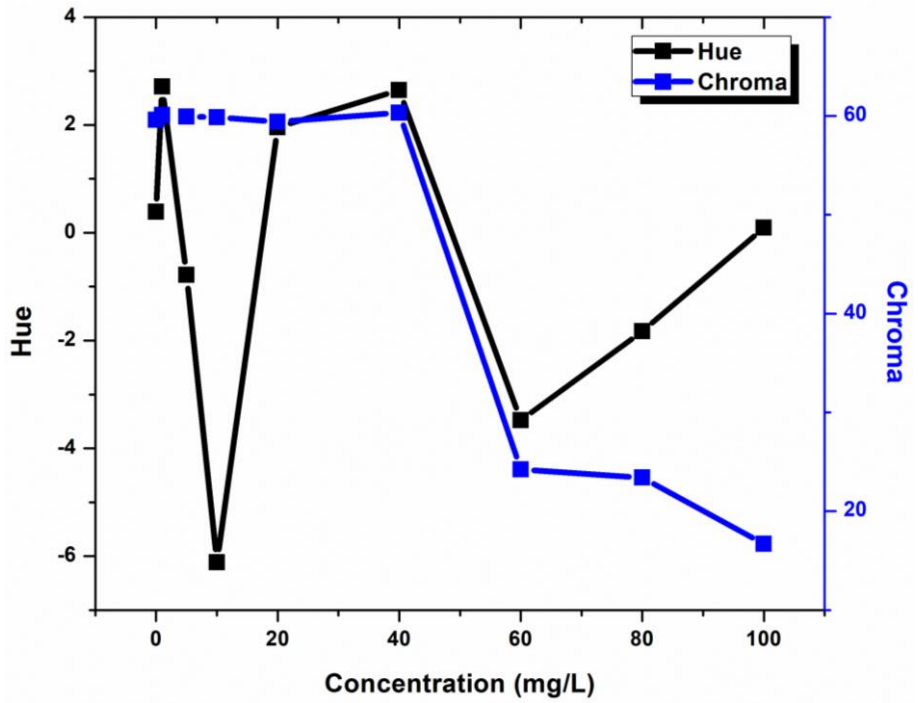

Figure 6.8: Plot of hue *vs* concentration of Pb(II) (black line) and plot of chroma *vs* concentration of Pb(II) (blue line)

6.1.8 Chromaticity system

The CIE system (Nxumalo 2019) is the most recognized method in which colour is represented by parameters x and y determining chromaticity of a colour and Y parameter representing luminance (brightness) of a colour. The colour space is then represented in a 2-D chromaticity diagram and can be used to predict outcome of colour mixtures (Hill, Roger and Vorhagen 1997). The chromaticity diagram for the colorimetric detection of Pb(II) using the TRPIDB_H-AuNPs is shown in Figure 6.9. From the chromaticity diagram it was noticed that the yellow-coloured solutions from the photographic image in Figure 6.4 (a) are situated in the yellow region of the chromaticity diagram. These are the blue coloured points in the chromaticity diagram labelled at blank, 1, 5, 10, 20 and 40 mg/L respectively. Meanwhile, the reddish brown-coloured samples are situated red region of the chromaticity diagram. These are red coloured points in the chromaticity diagram labelled 60, 80 and 100 mg/L, respectively. The results validated the RGB colour coordinates and CIE L*a*b* colour space as efficient and accurate colorimetric tool as they replicated the same colours as the photographic image.

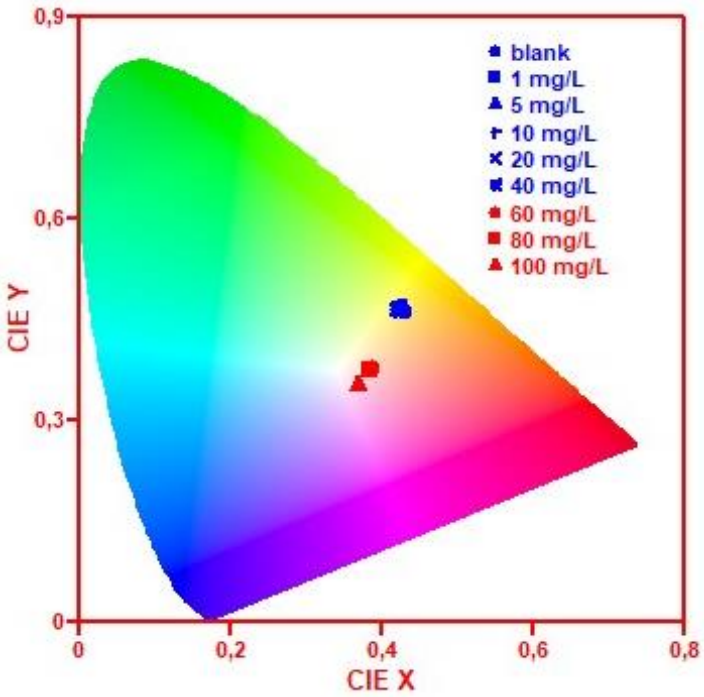

Figure 6.9: Chromaticity diagram of TRPIDB_H-AgNPs in the presence of Pb(II) concentration in the range of 1-100 mg/L.

CHAPTER SEVEN

7.0 CASE STUDY FOUR

7.1 Colorimetric detection of Mn(II) using 3-(4-hydroxy-3-methoxyphenyl)-2, 3-dihydropyrazolo [3, 4-b] indole-1(4H)-carbothioamide capped gold nanoparticles: A CIE L*a*b*/Yxy colour space study.

7.1.1 Characterization of TRPIDA_V complex

The FT-IR spectrum in Figure 7.1 (a) exhibited stretching absorption (cm $^{-1}$) at 3388, 1504, 1333, 734 and out of plane bend at 734 cm $^{-1}$ which were assigned to secondary N-H, C=S, C-N, C-O and N-H, respectively. Furthermore, the mass spectrum in Figure 7.1 (b) TOF-MS showed 340.4 [M^+] for the molecular ion confirming compound TRPIDA_V as 3-(4-hydroxy-3-methoxyphenyl)-2, 3-dihydropyrazolo [3, 4-b] indole-1(4H)-carbothioamide.

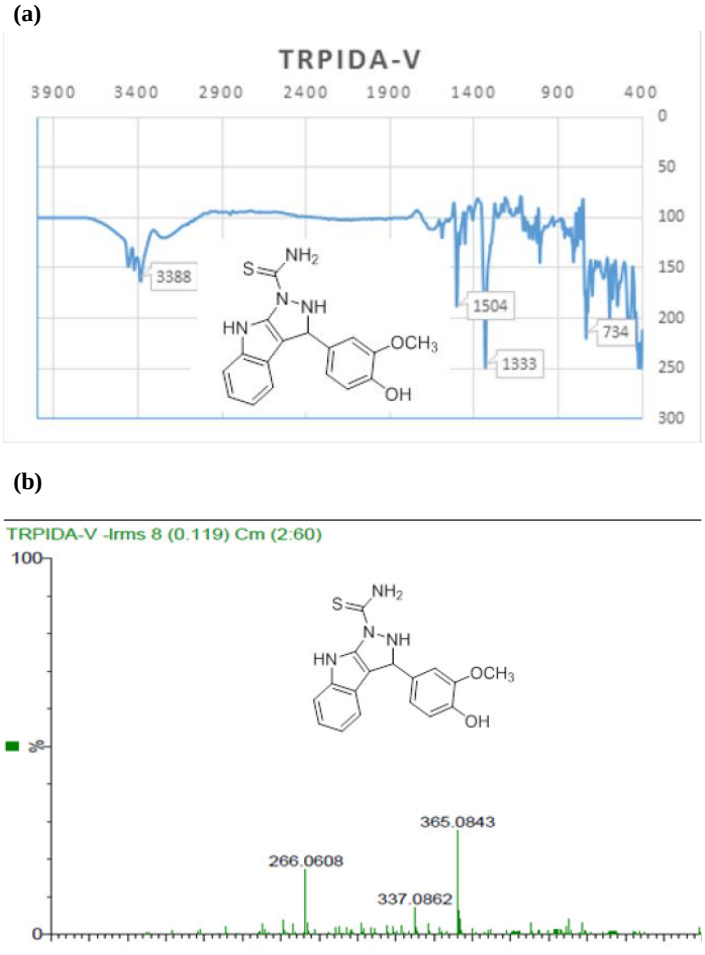

Figure 7.1: (a) IR spectrum and (b) TOF-MS spectrum for TRPIDA_V

The ^{1}H NMR spectrum in Figure 7.2 (a) exhibited signals at δ 10.9 for overlapping N-H indole and thioamide while at 2.0 exhibited signal for N-H pyrazole. Aromatic protons at 8.7 (s, OH), 7.4 (1H, d, *J* = 7.6 Hz), 7.3 (1H, d, *J* = 7.6 Hz), 7.1 (1H, t, *J* = 8.0 Hz), 7.0 (1H, d, *J* = 8.0 Hz), 6.9 (1H, s), 6.8 (1H, d, *J* = 7.6 Hz), 6.7 (1H, t, *J* = 8.0 Hz), 5.8 (1H, s), 3.7 (s, OCH3) ppm. The ^{13}C NMR spectrum in Figure 7.2 (b) exhibited the presence of CH carbons at δ 39.8, 55.6, 111.4, 112.8, 115.0, 118.0, 118.6, 119.2, 120.5, 120.8, 123.4, 135.9, 136.6, 144.5, 147.2, 170.3 ppm.

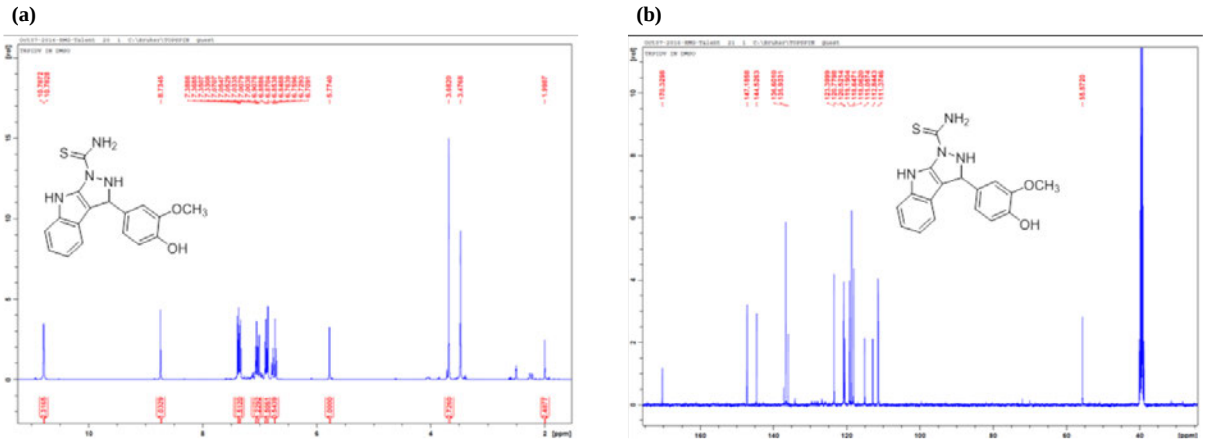

Figure 7.2: ^{1}H NMR spectrum and (b) ^{13}C NMR spectrum for TRPIDA_V

7.1.2 Optimization of TRPIDA_V-AuNPs colorimetric sensor

UV–Vis spectrophotometry was used for qualitative measurements of Mn(II) using TRPIDA_V-AuNPs to monitor the colour change induced the presence of Mn(II) as shown in Figure 7.3. The UV-Vis results presented in Figure 7.3 confirmed it by depicting two well separated peaks at 520 and 655 nm, respectively. A change upon increasing the concentration of Mn(II) was observed from the UV-Vis spectra upon the addition of 2 mg/L Mn(II) that led to a slight red shift to 655 nm wavelength.

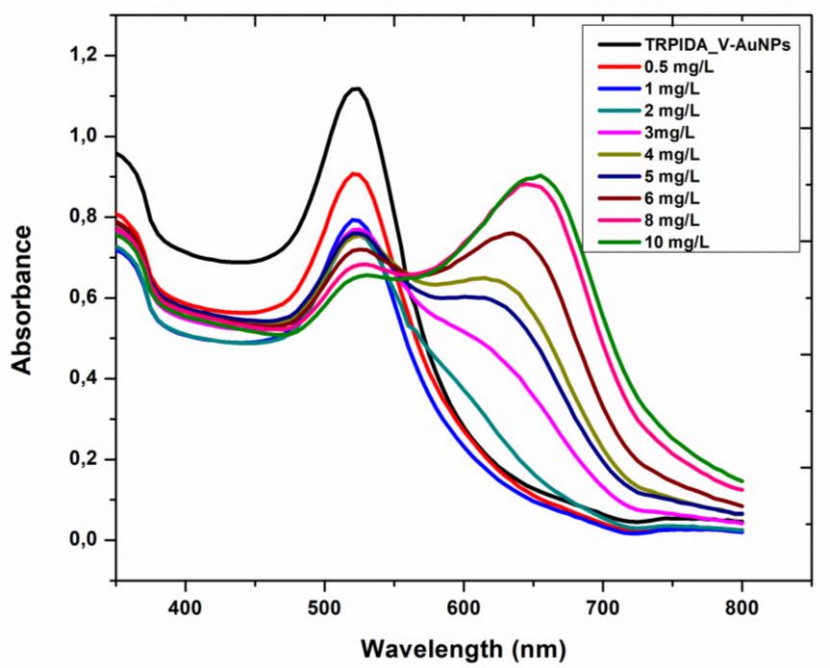

Figure 7.3: UV-Vis spectra of TRPIDA_V-AuNPs (blank) and different concentrations of Mn(II) in the range of 0.5-10.0 mg/L.

Both dispersed and aggregated forms of functionalized TRPIDA_V-AuNPs have strong extinction coefficients to enable colorimetric determinations even by naked eyes (Takatsuji, Ikeno and Haruyama 2012). The wine red colour of the functionalized TRPIDA_V-AuNPs turned to blue when the TRPIDA_V-AuNPs aggregate in solution in the presence of Mn(II) solution (Qi, Shang and Wu 2012) due to the alterations of SPR properties of the particles. In this work the use of Mn(II) standard solutions reacted with the TRPIDA_V-AuNPs to induce aggregation of the TRPIDA_V-AuNPs. The various colour changes produced from the colorimetric assay are shown in Scheme 7.1

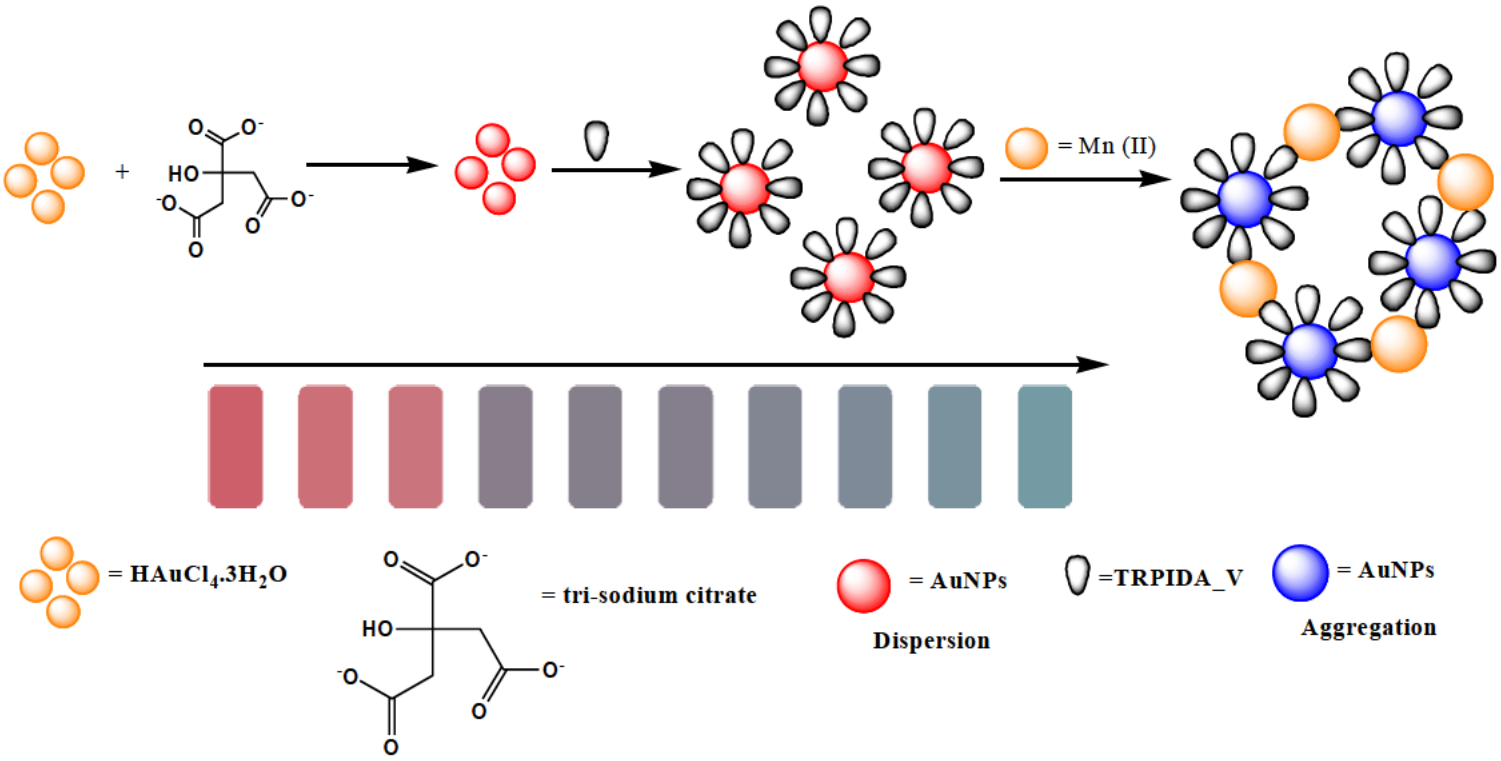

Scheme 7.1: Schematic illustration of the detection mechanism of Mn(II) ions based on the aggregation of TRPIDA_V modified AuNPs.

7.1.3 Selectivity and sensitivity of Mn(II)

The selectivity of the proposed colorimetric detection method was tested using 2 mg/L of eight metal ions namely; Cu(II), NO_3^-, Zn(II), Pb(II), NO_2^-, Cr(VI), Ni(II) and Mn(II). These metal ions were added into the TRPIDA_V-AuNPs. The photographic image and UV- Vis spectra of the TRPIDA_V-AuNPs in the presence of 2 mg/L metal ions are shown in Figure 7.4 (a) and (b), respectively. The TRPIDA_V-AuNPs remained wine red in colour after the addition of different metal ions at 2 mg/L except for Mn(II) which changed from wine red to blue as shown in Figure 7.4 (a). Additionally, the SPR absorption decreased rapidly with the addition of Mn(II) depicting a second peak at 655 nm. Plot of absorbance at 655/520 nm vs meal ions at 2 mg/L concentration is presented as a bar graph in Figure 7.4 (c) to display the selectivity of Mn(II). Therefore, these results confirmed that the selectivity of TRPIDA_V-AuNPs colorimetric detection system is excellent compared to other investigated interfering metal ions.

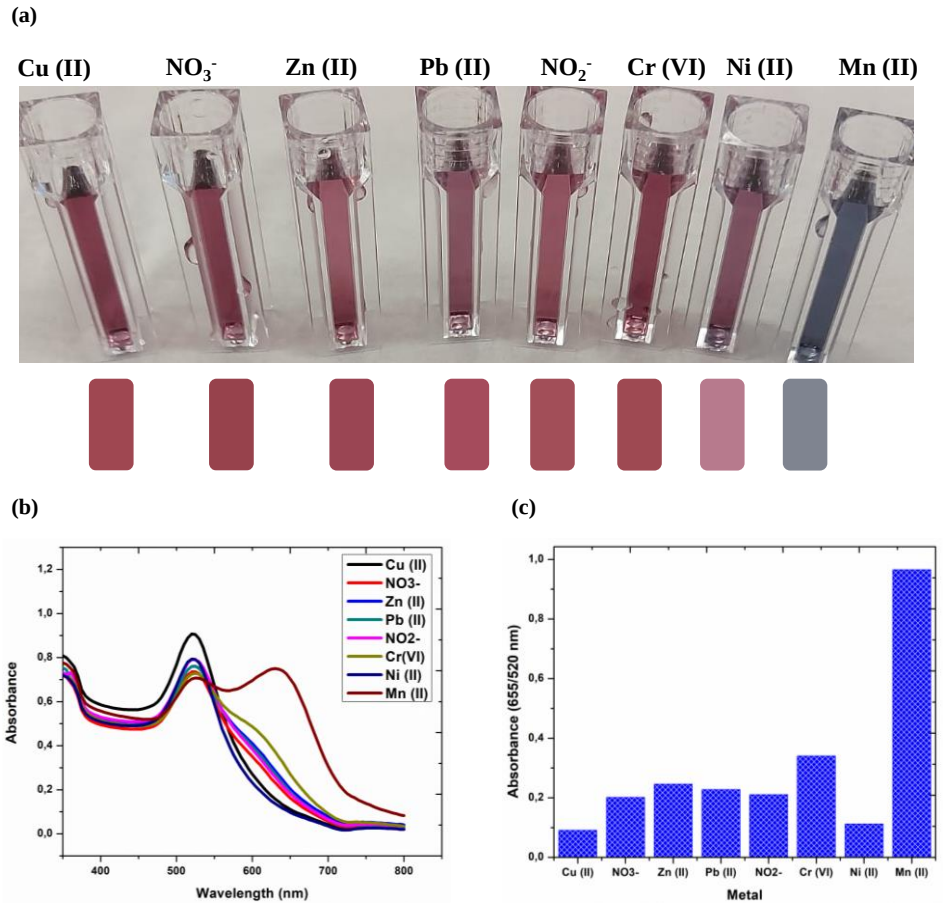

Figure 7.4: (a) Photographic image and (b) UV–Vis spectra of the TRPIDA_V-AuNPs in the presence of different metal ions at 2mg/L

The sensitivity of our proposed colorimetric detection method to Mn(II) under the optimized experimental conditions was recorded by the colour change of the TRPIDA_V-AuNPs solution. UV-Vis spectra of the TRPIDA_V-AuNPs containing different Mn (II) concentrations is shown in Figure 7.3. An observation was made that with the increasing concentration of Mn(II) from 2-10 mg/L the SPR absorption peak at 520 nm decreased and a second peak at 655 nm appeared. Moreover, the UV-Vis spectra of the TRPIDA_V-AuNPs with Mn (II) concentration in the range of 0.5-10 mg/L were for the quantitative analysis. Plot of absorbance at 655/520 nm against Mn(II) concentration in the range of 0.5-10 mg/L is shown in Figure 7.5 (a) gave a good linear relationship (R^2 = 0.97636) with a limit of detection and quantification of 0.006991 and 0.00233 mg/L, respectively. LOD and LOQ were calculated as 3×S/m and 10×S/m, respectively, where S is the standard deviation of the response factor and m is the slope of the calibration curve. Additionally, standards were analysed in triplicate. Plot of residual absorbance against Mn(II) concentration depicted that the plots are randomly distributed in Figure 7.5 (b).

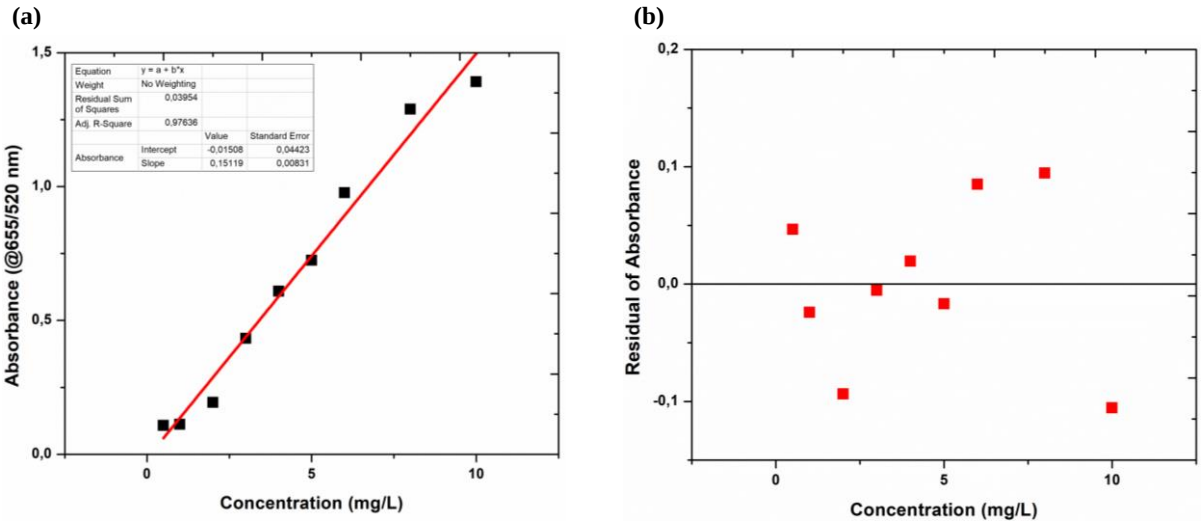

Figure 7.5: (a) Plot of absorbance (@655/520 nm) *vs* concentration and (b) plot of residual absorbance *vs* concentration of Mn(II)in the range of 0,10 mg/L.

7.1.4 Image processing

The captured photograph image was analysed using ImageJ Software Application histograms to obtain the RGB colour coordinates of the TRPIDA_V AuNPs (blank) and Mn(II) standard solutions in the concentration range of 0.5-10 mg/Lin Figure 7.6 (a). The obtained RGB values were then inserted to a Microsoft PowerPoint Shape Fill tab under More Fills colour model and the corresponding RGB values were inserted to obtain the presented block colour presented in Figure 7.6 (b). The obtained colour fills (insert below photographic image) agreed with the captured photograph image of the TRPIDA_V-AuNPs with different Mn(II) concentration. Additionally, the RGB colour coordinates were presented graphically in Figure 7.6 (b) to better understand the trend of each colour coordinate as the Mn(II) concentration increases. The red values decreased significantly with an increase in Mn(II) concentration. Whilst the green and blue values followed the same trend and rapidly increased with an increase in Mn(II) concentration. Indicating that the red colour changed to blue with an increase of Mn(II) concentration. The obtained RGB values were then converted to XYZ values using Equation 3-1.

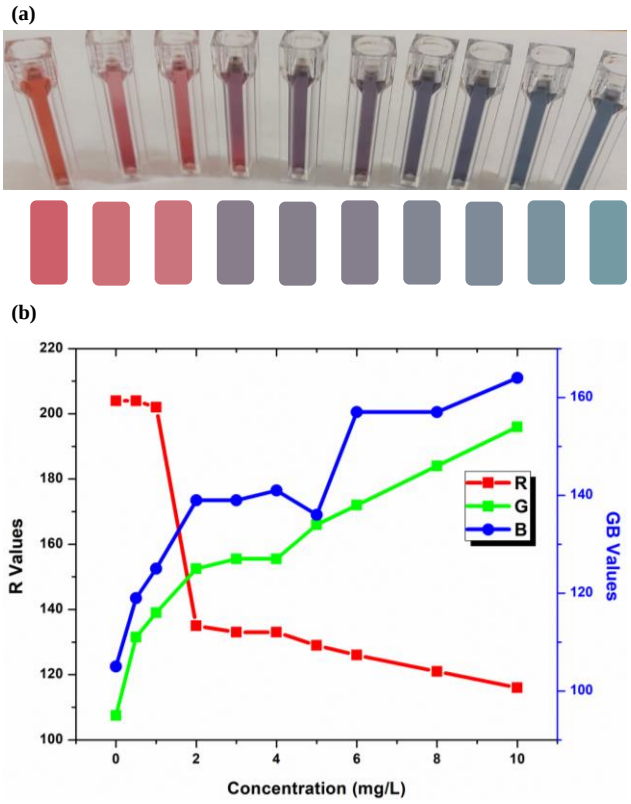

Figure 7.6: (a) Photographic image of TRPIDA_V-AuNPs and Mn(II) and (b) plot of RGB values *vs* Mn(II) concentration in the range of 0-10 mg/L.

The obtained XYZ values displayed similar trends as the RGB values where a rapid decrease in the X values was observed in Figure 7.7 (a) from 1-2 mg/L. The Y values increased from 0-1 mg/L and decreased significantly at 2 mg/L followed by an increase from 3-10 mg/L. The Z values increased rapid from 0-4 mg/L then a decrease at 5 mg/L was observed followed by a rapid increase from 6-10 mg/L/ Based on trends presented from the XYZ values it is safe to say that the obtained results agreed with the CIE 2° and 10° Standard Observers (Sharma 2018) in Figure 1.4. This phenomenon confirms that the proposed colorimetric sensor is efficient and can be further applied in the detection of Mn(II). The XYZ values were then converted to L*a*b* values using Equation 3-2 and the obtained results are shown in Figure 7.7 (b). It was observed that the X and L values trends are almost identical. The rapid decrease in the L values from 1-2 mg/L indicated that Mn(II) standard solution change from lightness to darkness. Thus, obtaining positive a* and b* values confirmed that the samples were red and blue, respectively.

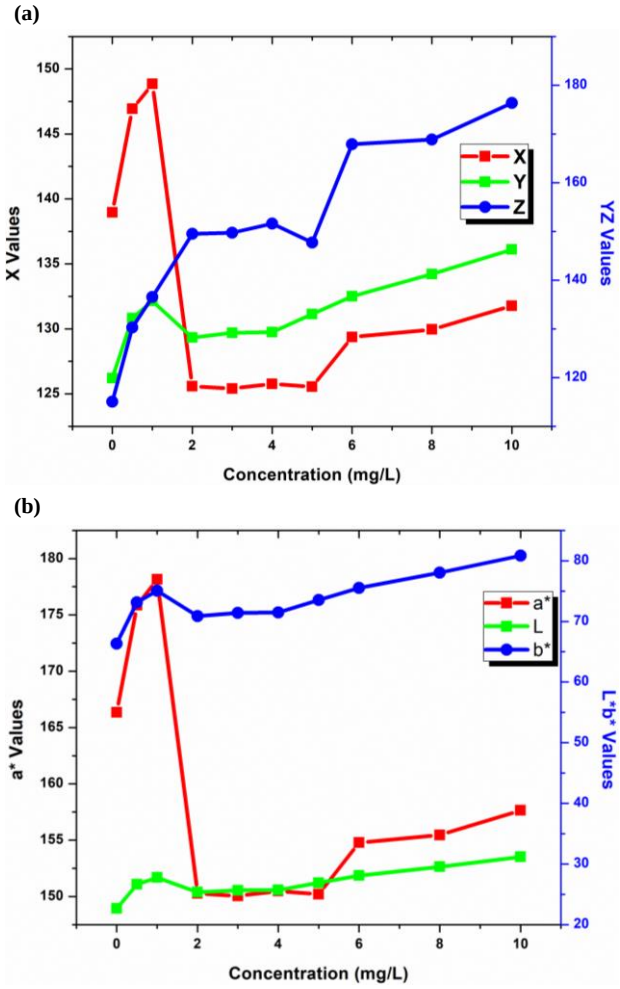

Figure 7.7: (a) Plot of XYZ values *vs* Mn(II) concentration and (b) plot of L*a*b* values *vs* Mn(II) concentration in the range of 0-10 mg/L.

The colour difference was calculated using Equation 2-1 using the obtained L*a*b* values from Equation 3-2. The results of the colour differences obtained from the colorimetric assay of the Mn(II) standard solution in the range of 0,5-10 mg/L are shown in Figure 7.8 (a) (black line) with TRPIDA_V-AuNPs as the blank. It was observed that the colour difference values increased with increasing Mn(II) standard concentration in Figure 7.8 (a). The colour intensity was obtained by using ImageJ software application. A 10 mm circle was drawn in each spot in the photographic image and a measure analysis was selected from toolbar. The colour intensity decreased as the Mn(II) standard solutions concentration increased as shown in Figure 7.8 (a) (blue line). The intensity of the colour was inversely proportional to the Mn(II) standard solution concentration. The hue decreased as the Mn(II) concentration increased in Figure 7.8 (b) (black line). Hue and the intensity followed the same trend. Meanwhile, the chroma decrease significantly in Figure 7.8 (b) (blue line) from 1-2 mg/L indicating the TRPIDA_V-AuNPs in the presence of Mn(II) standards solutions changed from vivid to dull as the Mn(II) increases (as they changed from wine red to blue).

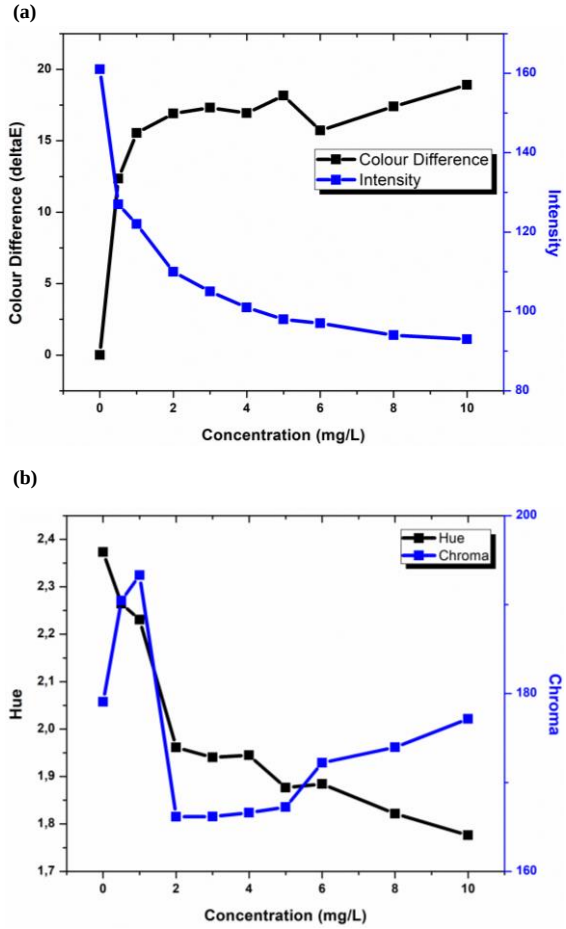

Figure 7.8: (a) Plot of colour difference (black line) and plot of colour intensity (blue line) *vs* Mn(II) concentration and (b) plot of hue (black line) and *vs* Mn(II) concentration.

7.1.5 Detection of river and tap water samples

UV-Vis results of TRPIDA_V-AuNPs spiked with 0.5, 2, 4, 6, and 10 river and tap water Mn(II) standard solutions are presented in Table 7.1. The %Recovery and %RSD of river water sample was between 90.42-102.45% and 0.02-0.58%, respectively. While the %Recovery and %RSD for tap water samples was between 98.06-104.87% and 0.01-0.34%, respectively. These results proved the proposed colorimetric sensor to be highly robust and efficient for both river and tap water samples.

Table 7.1: Showing the %Recovery and %RSD of the proposed colorimetric sensor for the detection of Mn(II)

Sample	Spiked (mg/L)	Absorbance (@655/520 nm)	Actual (mg/L)	Theoretical (mg/L)	Recovery (%)	RSD (%)
River Water	0.5	0.104013863	0.6595	0.6382	96.78	0.04
	2	0.176048678	1.2467	1.1273	90.42	0.12
	4	0.623805987	4.0673	4.1670	102.45	0.58
	6	0.934418346	6.5653	6.2758	95.59	0.02
	10	1.339143214	9.3769	9.0234	96.23	0.25
Tap Water	0.5	0.105257958	0.6595	0.6467	98.06	0.34
	2	0.20112389	1.2467	1.2975	104.07	0.05
	4	0.637302778	4.0673	4.2587	104.71	0.05
	6	1.023714681	6.5653	6.8820	104.82	0.01
	10	1.4141926	9.3769	9.5329	101.66	0.02

CHAPTER EIGHT

8.0 CONCLUSIONS

This study presents an innovative, simple, sensitive, selective, cost-efficient colorimetric sensors that were developed using functionalized gold and silver nanoparticles. The innovation part played a massive role in this study as three of the four functionalization ligands were synthesized in our laboratories and only one was commercially bought. A simple colorimetric method based on the aggregation TRPIDA_CH_3-AuNPs of was successfully developed for highly sensitive and selective detection Cr(VI). This colorimetric assay allowed the detection of Cr(VI) by simple UV–Vis spectroscopy as well as CEIL*a*b*/Yxy colour systems. Thus, the synthesized colorimetric sensor proved to be highly sensitive to Cr(VI) in aqueous solutions and also demonstrated pleasing selectivity over the investigated metal ions. Additionally, this method provided a great potential application in real water samples.

This study demonstrated a simple concentration measurement by a colorimetric method based on the detection of hexavalent chromium using CIEL*a*b* colour system and RGB colour coordinates. The use of colour difference *(ΔE*) was appropriate for a colorimetric concentration measurement based on the multiple colour changes due to the DPC-AuNPs aggregation. The combination of the DPC-AuNPs and image analysis based on *ΔE* enabled quantitative analysis for multiple colour changes as expected. The present method will accelerate applications to point of care testing and in resource limited settings. The aggregation of gold nanoparticles was further proved using molecular dynamics simulation.

The sensitive and rapid colorimetric detection sensor of Pb(II) ions based on the fact that the Pb(II) ions induced aggregation of the TRPIDB_H-AgNPs was successfully developed. The colour of the TRPIDB_H-AgNPs solution changed from yellow to reddish brown and was monitored by UV-Vis spectroscopy, RGB colour coordinates and CIE L*a*b*/Yxy colour space. The RGB colour coordinates and CIE L*a*b*/Yxy colour space measurements depicted colour dynamics that corresponded with the captured photographic image of TRPIDB_H-AgNPs in the presence of different Pb(II) standard concentration. Furthermore, no special additives or complex instrumentation were involved in this study.

A simple, rapid and efficient colorimetric detection system using TRPIDA_V-AuNPs was successfully developed for the selective and sensitive determination of Mn(II). The synthesis and functionalization of colorimetric detection system showed good sensitivity with a detection

limit of 0.00691 mg/L. The colorimetric proved to be highly selective only to Mn(II) ion compared to other investigated metal ions as there was no colour change on all the metal ions except for Mn(II). The UV-Vis spectra also validated the selectivity of the colorimetric detection system as there was one SPR peak at 520 nm for all the metal ions that were investigated and only Mn(II) showed two well separated peaks and 520 nm and 655 nm. Image processing using ImageJ software application yielded RGB values that matched the naked eye colorimetric response of the Mn(II) calibration standard solutions. The conversion of RGB values to XYZ values and conversion of XYZ values to L*a*b* values was a success as this was confirmed by the values matching the colours obtained in the captured photographic image. Furthermore, the L*a*b* values yielded a colour difference which was directly proportional to Mn(II) concentration as the colour difference increased as the Mn(II) concentration increased. The CIE L*a*b* colour system confirmed the intensity colour variation for the chroma and hue of the Mn(II) standards solutions. Finally, the colorimetric detection system yielded high %Recoveries and very low %RSD on the spiked river and tap water samples.

REFERENCES

Abira, M. A. 2008. *A Pilot Constructed Treatment Wetland for Pulp and Paper Mill Wastewater: Performance, Processes and Implications for the Nzoia River, Kenya, UNESCO-IHE PhD*. CRC Press.

Balavigneswaran, C., Kumar, T. S. J., Packiaraj, R. M. and Prakash, S. 2014. Rapid detection of Cr(VI) by AgNPs probe produced by Anacardium occidentale fresh leaf extracts. *Applied Nanoscience*, 4 (3): 367-378.

Barciszewska, M. Z., Szymanski, M., Wyszko, E., Pas, J., Rychlewski, L. and Barciszewski, J. 2005. Lead toxicity through the leadzyme. *Mutation Research/Reviews in Mutation Research*, 589 (2): 103-110.

Baskar, G., Deeptha, V. and Rahman. 2009. Treatment of wastewater from kitchen in an institution hostel mess using constructed wetland. *International Journal of Recent Trends in Engineering*, 1 (6): 54.

Baysal, A., Ozbek, N., Akman, S. 2013. Determination of trace metals in waste water and their removal processes. *Waste Water-Treatment Technologies and Recent Analytical Developments*, 145-171.

Beauchemin, D. and Berman, S. 1989. Determination of trace metals in reference water standards by inductively coupled plasma mass spectrometry with on-line preconcentration. *Analytical Chemistry*, 61 (17): 1857-1862.

Beebe, N. H. 2019. A Bibliography of Post-Script and Portable Document Format Literature.

Boisselier, E. and Astruc, D. 2009. Gold nanoparticles in nanomedicine: preparations, imaging, diagnostics, therapies and toxicity. *Chemical Society Reviews*, 38 (6): 1759-1782.

Bower, C. E. and Holm-Hansen, T. 1980. A salicylate–hypochlorite method for determining ammonia in seawater. *Canadian Journal of Fisheries and Aquatic Sciences*, 37 (5): 794-798.

Campbell, F. W. and Compton, R. G. 2010. The use of nanoparticles in electroanalysis: an updated review. *Analytical and Bioanalytical Chemistry*, 396 (1): 241-259.

Cao, P., Gu, Y., Liu, F., Liu, H., Zhang, H., Shen, F., Zhang, Q., Zhong, D., Li, J. and Liu, S. 2005. Fabrication of carbon nanotube bundles and measurement of field electron emission properties. *Applied Physics A*, 80 (1): 195-199.

Cenens, J. and Schoonheydt, R. 1988. Visible spectroscopy of methylene blue on hectorite, laponite B, and barasym in aqueous suspension. *Clays and Clay Minerals*, 36 (3): 214-224.

Chai, F., Wang, C., Wang, T., Li, L. and Su, Z. 2010. Colorimetric detection of Pb(II) using glutathione functionalized gold nanoparticles. *ACS Applied Materials & Interfaces*, 2 (5): 1466-1470.

Chen, M.-L., Zhao, Y.-N., Zhang, D.-W., Tian, Y. and Wang, J.-H. 2010. The immobilization of hydrophilic ionic liquid for Cr(VI) retention and chromium speciation. *Journal of Analytical Atomic Spectrometry*, 25 (11): 1688-1694.

Chen, M., Cai, H.-H., Yang, F., Lin, D., Yang, P.-H. and Cai, J. 2014. Highly sensitive detection of chromium(III) ions by resonance Rayleigh scattering enhanced by gold nanoparticles. *Spectrochimica Acta Part A: Molecular and Biomolecular Spectroscopy*, 118: 776-781.

Chen, W., Cao, F., Zheng, W., Tian, Y., Xianyu, Y., Xu, P., Zhang, W., Wang, Z., Deng, K. and Jiang, X. 2015. Detection of the nanomolar level of total Cr[(III) and (VI)] by functionalized gold nanoparticles and a smartphone with the assistance of theoretical calculation models. *Nanoscale*, 7 (5): 2042-2049.

Chen, Y.-C., Lee, I.-L., Sung, Y.-M. and Wu, S.-P. 2013. Triazole functionalized gold nanoparticles for colorimetric Cr(III) sensing. *Sensors and Actuators B: Chemical*, 188: 354-359.

Cheng, G., He, M., Peng, H. and Hu, B. 2012. Dithizone modified magnetic nanoparticles for fast and selective solid phase extraction of trace elements in environmental and biological samples prior to their determination by ICP-OES. *Talanta*, 88: 507-515.

Cheng, X., Dai, D., Yuan, Z., Peng, L., He, Y. and Yeung, E. S. 2014. Color difference amplification between gold nanoparticles in colorimetric analysis with actively controlled multiband illumination. *Analytical Chemistry*, 86 (15): 7584-7592.

Choudhury, A. R. and Chatterjee, S. 1996. Evaluation of the performance of metameric indices. *Color Research & Application*, 21 (1): 26-34.

Chwastowska, J., Skwara, W., Sterlińska, E. and Pszonicki, L. 2005. Speciation of chromium in mineral waters and salinas by solid-phase extraction and graphite furnace atomic absorption spectrometry. *Talanta*, 66 (5): 1345-1349.

Connolly, C. and Fleiss, T. 1997. A study of efficiency and accuracy in the transformation from RGB to CIELAB color space. *IEEE transactions on image processing*, 6 (7): 1046-1048.

Dadiboyena, S. and Nefzi, A. 2011. Synthesis of functionalized tetrasubstituted pyrazolyl heterocycles–A review. *European Journal of Medicinal Chemistry*, 46 (11): 5258-5275.

Dahlquist, R. and Knoll, J. 1978. Inductively coupled plasma-atomic emission spectrometry: analysis of biological materials and soils for major, trace, and ultra-trace elements. *Applied Spectroscopy*, 32 (1): 1-30.

Dang, Y.-Q., Li, H.-W., Wang, B., Li, L. and Wu, Y. 2009. Selective detection of trace Cr(III) in aqueous solution by using 5, 5′-dithiobis (2-nitrobenzoic acid)-modified gold nanoparticles. *ACS applied materials & interfaces*, 1 (7): 1533-1538.

Daniel, M.-C. and Astruc, D. 2004. Gold nanoparticles: assembly, supramolecular chemistry, quantum-size-related properties, and applications toward biology, catalysis, and nanotechnology. *Chemical Reviews*, 104 (1): 293-346.

Doyen, M., Bartik, K. and Bruylants, G. 2013. UV–Vis and NMR study of the formation of gold nanoparticles by citrate reduction: Observation of gold–citrate aggregates. *Journal of colloid and interface science*, 399: 1-5.

Dungeni, M. and Momba, M. J. W. S. 2010. The abundance of Cryptosporidium and Giardia spp. in treated effluents produced by four wastewater treatment plants in the Gauteng Province of South Africa. 36 (4)

Dunn, G., Harris, L., Cook, C. and Prystajecky, N. 2014. A comparative analysis of current microbial water quality risk assessment and management practices in British Columbia and Ontario, Canada. *Science of the Total Environment*, 468: 544-552.

Ford, A. and Roberts, A. 1998. Colour space conversions. *Westminster University, London*, 1998: 1-31.

Gao, Y.-X., Xin, J.-W., Shen, Z.-Y., Pan, W., Li, X. and Wu, A.-G. 2013. A new rapid colorimetric detection method of Mn(II) based on tripolyphosphate modified silver nanoparticles. *Sensors and Actuators B: Chemical*, 181: 288-293.

Gomez, V. and Callao, M. 2006. Chromium determination and speciation since 2000. *TrAC Trends in Analytical Chemistry*, 25 (10): 1006-1015.

Gonzalez, R. C. and Woods, R. E. 2002. Prentice hall Upper Saddle River, NJ. *Digital image processing*,

Guerrero, M. L., Alonso, E. V., Pavón, J. C., Cordero, M. S. and de Torres, A. G. 2012. On-line preconcentration using chelating and ion-exchange minicolumns for the speciation of chromium(III) and chromium(VI) and their quantitative determination in natural waters by

inductively coupled plasma mass spectrometry. *Journal of Analytical Atomic Spectrometry*, 27 (4): 682-688.

Guo, J.-F., Huo, D.-Q., Yang, M., Hou, C.-J., Li, J.-J., Fa, H.-B., Luo, H.-B. and Yang, P. 2016. Colorimetric detection of Cr(VI) based on the leaching of gold nanoparticles using a paper-based sensor. *Talanta*, 161: 819-825.

Guo, Y., Wang, Z., Qu, W., Shao, H. and Jiang, X. 2011. Colorimetric detection of mercury, lead and copper ions simultaneously using protein-functionalized gold nanoparticles. *Biosensors and Bioelectronics*, 26 (10): 4064-4069.

Hamadeh, A. F., Sharma, S. K., Amy, G. 2014. Comparative assessment of managed aquifer recharge versus constructed wetlands in managing chemical and microbial risks during wastewater reuse: a review. *Journal of Water Reuse and Desalination*, 4 (1): 1-8.

Harris, R., Mlambo, M. and Mdluli, P. 2016. Qualitative analysis of some alkanethiols on Au nanoparticles during SERS. *Royal Society of Chemistry Advances*, 6 (15): 12131-12142.

Hashemi, M. and Daryanavard, S. M. 2012. Ultrasound-assisted cloud point extraction for speciation and indirect spectrophotometric determination of chromium (III) and (VI) in water samples. *Spectrochimica Acta Part A: Molecular and Biomolecular Spectroscopy*, 92: 189-193.

Hearn, D. and Baker, M. P. 2004. Upper Saddle River, NJ: Pearson Prentice Hall. *Computer graphics with OpenGL*,

Hemmateenejad, B., Shakerizadeh-shirazi, F. and Samari, F. 2014. BSA-modified gold nanoclusters for sensing of folic acid. *Sensors and Actuators B: Chemical*, 199: 42-46.

Hill, B., Roger, T. and Vorhagen, F. W. 1997. Comparative analysis of the quantization of color spaces on the basis of the CIELAB color-difference formula. *ACM Transactions on Graphics (TOG)*, 16 (2): 109-154.

Hong, W., Liu, S.-Q., Han, C., Chang, G.-F., Liu, B. and Zou, X.-F. 2017. Research about impacts of specific pollutants like herbicides upon microbial activity of activated sludge systems in wastewater treatment plants. In: Proceedings of *IOP Conference Series: Earth and Environmental Science*. IOP Publishing, 012001.

Hossain, A., Canning, J., Ast, S., Rutledge, P. J., Yen, T. L. and Jamalipour, A. 2015. Lab-in-a-phone: Smartphone-based portable fluorometer for pH measurements of environmental water. *IEEE Sensors Journal*, 15 (9): 5095-5102.

Hosseini, M., Khabbaz, H., Dadmehr, M., Ganjali, M. R. and Mohamadnejad, J. 2015. Aptamer-based Colorimetric and Chemiluminescence detection of Aflatoxin B1 in foods samples. *Acta Chimica Slovenica*, 62 (3): 721-728.

Huang, X., Jain, P. K., El-Sayed, I. H. and El-Sayed, M. A. 2007. Gold nanoparticles: interesting optical properties and recent applications in cancer diagnostics and therapy. *Future Medicine Ltd 2,* (5), 681-693.

Hughes, S. I., Dasary, S. S., Singh, A. K., Glenn, Z., Jamison, H., Ray, P. C. and Yu, H. 2013. Sensitive and selective detection of trivalent chromium using hyper Rayleigh scattering with 5, 5′-dithio-bis-(2-nitrobenzoic acid)-modified gold nanoparticles. *Sensors and Actuators B: Chemical*, 178: 514-519.

Hunt, R. W. G. and Pointer, M. R. 2011. *Measuring colour*. John Wiley & Sons.

Imene, B., Cui, Z., Zhang, X., Gan, B., Yin, Y., Tian, Y., Deng, H. and Li, H. 2014. 4-Amino-3-mercaptobenzoic acid functionalized gold nanoparticles: synthesis, selective recognition and colorimetric detection of cyhalothrin. *Sensors and Actuators B: Chemical*, 199: 161-167.

Jhansi, S. C. and Mishra, S. K. 2013. Wastewater treatment and reuse: sustainability options. (10): *Journal of Consilience,* 1-15.

Jian-feng, G., Chang-jun, H., Mei, Y., Dan-qun, H., Jun-jie, L., Huan-bao, F., Hui-bo, L. and Ping, Y. 2016. Colorimetric sensing of chromium (VI) ions in aqueous solution based on the leaching of protein-stabled gold nanoparticles. *Analytical Methods*, 8 (27): 5526-5532.

Jin, W., Wu, G. and Chen, A. 2014. Sensitive and selective electrochemical detection of chromium (VI) based on gold nanoparticle-decorated titania nanotube arrays. *Analyst*, 139 (1): 235-241.

Kale, S., Pawar, R. and Kale, A. 2016. Imidazole, its derivatives & their importance: a review. *Applied Physics Letters*, 5 (5): 906-911.

Kanagaraj, R., Nam, Y.-S., Pai, S. J., Han, S. S. and Lee, K.-B. 2017. Highly selective and sensitive detection of Cr(VI) ions using size-specific label-free gold nanoparticles. *Sensors and Actuators B: Chemical*, 251: 683-691.

Kargosha, K. and Noroozifar, M. 2000. Solid-phase sodium bismuthate as an oxidant in flow injection analysis: determination of manganese in effluent streams. *Analytica Chimica Acta*, 413 (1-2): 57-61.

Kim, S. C., Jalal, U. M., Im, S. B., Ko, S. and Shim, J. S. 2017. A smartphone-based optical platform for colorimetric analysis of microfluidic device. *Sensors and Actuators B: Chemical*, 239: 52-59.

Kong, B., Zhu, A., Luo, Y., Tian, Y., Yu, Y. and Shi, G. 2011. Sensitive and selective colorimetric visualization of cerebral dopamine based on double molecular recognition. *Angewandte Chemie International Edition*, 50 (8): 1837-1840.

Kotaś, J. and Stasicka, Z. 2000. Chromium occurrence in the environment and methods of its speciation. *Environmental pollution*, 107 (3): 263-283.

Krishna, R., Fulekar, M. and Patakg, B. 2012. Rhizofiltration: a green technology for remediation of heavy metals. *International Journal of Innovation in Bio-Sciences*, (2): 4.

Kumar, T. and Verma, K. 2010. A Theory Based on Conversion of RGB image to Gray image. *International Journal of Computer Applications*, 7 (2): 7-10.

Kumar, V., Kaur, K., Gupta, G. K. and Sharma, A. K. 2013. Pyrazole containing natural products: synthetic preview and biological significance. *European Journal of Medicinal Chemistry*, 69: 735-753.

Lai, Y.-J. and Tseng, W.-L. 2011. Role of 5-thio-(2-nitrobenzoic acid)-capped gold nanoparticles in the sensing of chromium (VI): remover and sensor. *Analyst*, 136 (13): 2712-2717.

Lee, K.-S. and El-Sayed, M. A. 2006. Gold and silver nanoparticles in sensing and imaging: sensitivity of plasmon response to size, shape, and metal composition. *The Journal of Physical Chemistry B*, 110 (39): 19220-19225.

Lee, P. and Meisel, D. 1982. Adsorption and surface-enhanced Raman of dyes on silver and gold sols. *The Journal of Physical Chemistry*, 86 (17): 3391-3395.

Li, J., Du, J. and Zhang, J. 2014. Ethylenediaminetetraacetic acid functionalized gold nanoparticles for sensitive colorimetric detection of chromium(III). *Journal of the Chinese Chemical Society*, 61 (12): 1395-1399.

Liang, J., Liu, H., Lan, C., Fu, Q., Huang, C., Luo, Z., Jiang, T. and Tang, Y. 2014. Silver nanoparticle enhanced Raman scattering-based lateral flow immunoassays for ultra-sensitive detection of the heavy metal chromium. *Nanotechnology*, 25 (49): 495501.

Lin, Y., Gritsenko, D., Feng, S., Teh, Y. C., Lu, X. and Xu, J. 2016. Detection of heavy metal by paper-based microfluidics. *Biosensors and Bioelectronics*, 83: 256-266.

Liu, D., Wang, Z. and Jiang, X. 2011. Gold nanoparticles for the colorimetric and fluorescent detection of ions and small organic molecules. *Nanoscale*, 3 (4): 1421-1433.

Liu, H.-W., Jiang, S.-J. and Liu, S.-H. 1999. Determination of cadmium, mercury and lead in seawater by electrothermal vaporization isotope dilution inductively coupled plasma mass spectrometry. *Spectrochimica Acta Part B: Atomic Spectroscopy*, 54 (9): 1367-1375.

Liu, L., Leng, Y. and Lin, H. 2016. Photometric and visual detection of Cr(VI) using gold nanoparticles modified with 1, 5-diphenylcarbazide. *Microchimica Acta*, 183 (4): 1367-1373.

Lo, S.-H., Wu, M.-C., Venkatesan, P. and Wu, S.-P. 2015. Colorimetric detection of chromium(III) using O-phospho-l-serine dithiocarbamic acid functionalized gold nanoparticles. *Sensors and Actuators B: Chemical*, 220: 772-778.

Luther III, G. W., Nuzzio, D. B. and Wu, J. 1994. Speciation of manganese in Chesapeake Bay waters by voltammetric methods. *Analytica Chimica Acta*, 284 (3): 473-480.

Ly, N. and Joo, S.-W. 2015. Silver nanoparticle-enhanced resonance raman sensor of chromium(III) in seawater samples. *Sensors*, 15 (5): 10088-10099.

Ly, N. H., Oh, C. H. and Joo, S.-W. 2015. A submicromolar Cr(III) sensor with a complex of methionine using gold nanoparticles. *Sensors and Actuators B: Chemical*, 219: 276-282.

Ma, J., Yang, B. and Byrne, R. H. 2012. Determination of nanomolar chromate in drinking water with solid phase extraction and a portable spectrophotometer. *Journal of Hazardous Materials*, 219: 247-252.

Magubane, S. E., Mlambo, M., Mabaso, M. H., Muthwa, S. F., Kruger, H. G. and Mdluli, P. S. 2019. Optimization of CIEL* a* b*/Yxy colour system for colorimetric devices fabricated with gold nanoparticles. *Journal of Molecular Structure*, 1191: 271-277.

Makhanya, T. R. 2019. Synthesis, characterisation and biological activity of selected pyrazoles and naphthyrides.

Margulis, D. 2005. *Photoshop LAB color: The canyon conundrum and other adventures in the most powerful colorspace*. Peachpit Press.

Maunder, M. d. F. 1974. A field test for hallucinogens: further improvements. *Journal of Pharmacy and Pharmacology*, 26 (8): 637-638.

Meeravali, N. N., Madhavi, K. and Kumar, S. J. 2011. A sensitive sequential non-chromatographic speciation analysis of chromium in natural/wastewaters by inductively coupled plasma optical emission spectrometry. *Journal of Analytical Atomic Spectrometry*, 26 (1): 214-219.

Milosevic, N. and Maier, P. 2000. Lead stimulates intercellular signalling between hepatocytes and Kupffer cells. *European Journal of Pharmacology*, 401 (3): 317-328.

Mokrzycki, W. and Tatol, M. 2011. Colour differenceΔ E-A survey. *Machine Graphics and Vision*, 20 (4): 383-411.

Montangero, M. 2015. Determining the amount of copper(II) ions in a solution using a smartphone. *Journal of Chemical Education*, 92 (10): 1759-1762.

Mutaftchiev, K. L. 2001. Kinetic determination of nanogram levels of manganese(II) by Naphthol blue black–potassium periodate–1, 10-phenanthroline system. *Microchimica Acta*, 136 (1-2): 79-82.

Muthwa, S. F., Makhanya, T. R., Mlambo, M., Shumbula, N. P., Shumbula, P. M., Onwubu, S. C., Moloto, N., Gengan, R. M. and Mdluli, P. S. 2020. Synthesis and characterization of 3-(p-tolyl)-2, 3-dihydropyrazolo [3, 4-b] indole-1 (4H)-carbothioamide functionalized gold nanoparticles for the CIEL* a* b*/Yxy colorimetric detection of Cr(VI). *Journal of Molecular Structure*: 127985.

Myers, R. J. 2009. One-hundred years of pH. *Journal of Chemical Education*, 87 (1): 30-32.

Nascentes, C. C., Kamogawa, M. Y., Fernandes, K. G., Arruda, M. A., Nogueira, A. R. A. and Nóbrega, J. A. 2005. Direct determination of Cu, Mn, Pb, and Zn in beer by thermospray flame furnace atomic absorption spectrometry. *Spectrochimica Acta Part B: Atomic Spectroscopy*, 60 (5): 749-753.

Nxumalo, N. L. 2019. Development of paper-based microfluidic strips for quantification of ammonia.

OB, A., Muchie, M. 2010. Bioremediation of polluted wastewater influent: Phosphorus and nitrogen removal. *Scientific Research and Essays*, 5 (21): 3222-3230.

Odinga, C. A. 2018. Assessment of heavy metals and pathogens removal from municipal wastewater using a constructed rhizofiltration system.

Oliveira, E., Nunez, C., Santos, H. M., Fernandez-Lodeiro, J., Fernandez-Lodeiro, A., Capelo, J. L. and Lodeiro, C. 2015. Revisiting the use of gold and silver functionalised nanoparticles as colorimetric and fluorometric chemosensors for metal ions. *Sensors and Actuators B: Chemical*, 212: 297-328.

Organization, W. H. 1996. *Trace elements in human nutrition and health*. World Health Organization.

Parmar, M., Thakur, L. S. 2013. Heavy metal Cu, Ni and Zn: Toxicity, health hazards and their removal techniques by low cost adsorbents: A short overview. *International Journal of Plant, Animal and Environmental Sciences,* 3 (3): 143-157.

Priyadarshini, E. and Pradhan, N. 2017a. Gold nanoparticles as efficient sensors in colorimetric detection of toxic metal ions: a review. *Sensors and Actuators B: Chemical*, 238: 888-902.

Priyadarshini, E. and Pradhan, N. 2017b. Metal-induced aggregation of valine capped gold nanoparticles: an efficient and rapid approach for colorimetric detection of Pb(II) ions. *Scientific reports*, 7 (1): 1-8.

Qi, L., Shang, Y. and Wu, F. 2012. Colorimetric detection of lead(II) based on silver nanoparticles capped with iminodiacetic acid. *Microchimica Acta*, 178 (1-2): 221-227.

Rakhunde, R., Deshpande, L. and Juneja, H. 2012. Chemical speciation of chromium in water: a review. *Critical reviews in environmental science and technology*, 42 (7): 776-810.

Ratnarathorn, N., Chailapakul, O. and Dungchai, W. 2015. Highly sensitive colorimetric detection of lead using maleic acid functionalized gold nanoparticles. *Talanta*, 132: 613-618.

Ravindran, A., Elavarasi, M., Prathna, T., Raichur, A. M., Chandrasekaran, N. and Mukherjee, A. 2012. Selective colorimetric detection of nanomolar Cr(VI) in aqueous solutions using unmodified silver nanoparticles. *Sensors and Actuators B: Chemical*, 166: 365-371.

Sağ, Y., Özer, D. and Kutsal, T. 1995. A comparative study of the biosorption of lead(II) ions to Z. ramigera and R. arrhizus. *Process Biochemistry*, 30 (2): 169-174.

Shahrivari, S., Faridbod, F. and Ganjali, M. R. 2018. Highly selective and sensitive colorimetric determination of Cr3+ ion by 4-amino-5-methyl-4H-1, 2, 4-triazole-3-thiol functionalized Au nanoparticles. *Spectrochimica Acta Part A: Molecular and Biomolecular Spectroscopy*, 191: 189-194.

Shaikh, R., Memon, N., Solangi, A. R., Shaikh, H. I., Agheem, M. H., Ali, S. A., Shah, M. R. and Kandhro, A. 2017. 2, 3-Pyridine dicarboxylic acid functionalized gold nanoparticles: Insight into experimental conditions for Cr(III) sensing. *Spectrochimica Acta Part A: Molecular and Biomolecular Spectroscopy*, 173: 241-250.

Shamsipur, M., Memari, Z., Ganjali, M. R., Norouzi, P. and Faridbod, F. 2016. Highly sensitive gold nanoparticles-based optical sensing of DNA hybridization using bis (8-hydroxyquinoline-5-solphonate) cerium(III) chloride as a novel fluorescence probe. *Journal of pharmaceutical and biomedical analysis*, 118: 356-362.

Sharif, T., Niaz, A., Najeeb, M., Zaman, M. I. and Ihsan, M. 2015. Isonicotinic acid hydrazide-based silver nanoparticles as simple colorimetric sensor for the detection of Cr(III). *Sensors and Actuators B: Chemical*, 216: 402-408.

Sharma, A. 2018. *Understanding color management*. John Wiley & Sons.

Sharma, G., Wu, W. and Dalal, E. N. 2005. The CIEDE2000 color-difference formula: Implementation notes, supplementary test data, and mathematical observations. *Color Research & Application: Endorsed by Inter-Society Color Council, The Colour Group (Great Britain), Canadian Society for Color, Color Science Association of Japan, Dutch Society for the Study of Color, The Swedish Colour Centre Foundation, Colour Society of Australia, Centre Français de la Couleur*, 30 (1): 21-30.

Shen, Z. 2003. Colour differentiation in digitial images. Victoria University of Technology.

Sheng, S.-R., Wang, X.-Y., Xu, H.-Z., Zhu, G.-Q. and Zhou, Y.-F. 2010. Anatomy of large animal spines and its comparison to the human spine: A systematic review. *European Spine Journal*, 19 (1): 46-56.

Shiraishi, Y., Tanaka, H., Sakamoto, H., Ichikawa, S. and Hirai, T. 2017. Photoreductive synthesis of monodispersed Au nanoparticles with citric acid as reductant and surface stabilizing reagent. *Royal Society of Chemistry Advances*, 7 (11): 6187-6192.

Sivaraman, S. K., Kumar, S. and Santhanam, V. 2011. Monodisperse sub-10 nm gold nanoparticles by reversing the order of addition in Turkevich method–The role of chloroauric acid. *Journal of colloid and Interface Science*, 361 (2): 543-547.

Soto-Neira, J., Zhu, Q. and Aller, R. C. 2011. A new spectrophotometric method to quantify dissolved manganese in marine pore waters. *Marine Chemistry*, 127 (1-4): 56-63.

Sung, Y.-M. and Wu, S.-P. 2014. Highly selective and sensitive colorimetric detection of Ag(I) using N-1-(2-mercaptoethyl) adenine functionalized gold nanoparticles. *Sensors and Actuators B: Chemical*, 197: 172-176.

Takatsuji, Y., Ikeno, S. and Haruyama, T. 2012. Gold nanoparticles functionalized with peptides for specific affinity aggregation assays of estrogen receptors and their agonists. *Sensors*, 12 (4): 4952-4961.

Tauler, R., Smilde, A., Henshaw, J., Burgess, L. and Kowalski, B. 1994. Multicomponent Determination of Chlorinated Hydrocarbons Using a Reaction-based Chemical Sensor. Part 2. Chemical Speciation Using Multivariate Curve Resolution. *Analytical chemistry*, 66 (20): 3337-3344.

Tewari, A. K., Singh, V. P., Yadav, P., Gupta, G., Singh, A., Goel, R. K., Shinde, P. and Mohan. 2014. Synthesis, biological evaluation and molecular modeling study of pyrazole derivatives as selective COX-2 inhibitors and anti-inflammatory agents. *Bioorganic Chemistry Journal*, 56: 8-15.

Tolaymat, T. M., El Badawy, A. M., Genaidy, A., Scheckel, K. G., Luxton, T. P. and Suidan, M. 2010. An evidence-based environmental perspective of manufactured silver nanoparticle in syntheses and applications: a systematic review and critical appraisal of peer-reviewed scientific papers. *Science of the Total Environment*, 408 (5): 999-1006.

Tripathy, S. K., Woo, J. Y. and Han, C.-S. 2013. Colorimetric detection of Fe(III) ions using label-free gold nanoparticles and acidic thiourea mixture. *Sensors and Actuators B: Chemical*, 181: 114-118.

Tsuyumoto, I. and Maruyama, Y. 2011. X-ray fluorescence analysis of hexavalent chromium using Kβ satellite peak observed as counterpart of X-ray absorption near-edge structure pre-edge peak. *Analytical Chemistry*, 83 (19): 7566-7569.

Turkevich, J. 1985. Colloidal gold. Part II. *Gold bulletin*, 18 (4): 125-131.

Turkevich, J., Stevenson, P. C. and Hillier, J. 1951. A study of the nucleation and growth processes in the synthesis of colloidal gold. *Discussions of the Faraday Society*, 11: 55-75.

Vaitukaitis, J. L. 2004. Development of the home pregnancy test. *Annals of the New York Academy of Sciences*, 1038 (1): 220-222.

Wang, A.-J., Guo, H., Zhang, M., Zhou, D.-L., Wang, R.-Z. and Feng, J.-J. 2013. Sensitive and selective colorimetric detection of cadmium(II) using gold nanoparticles modified with 4-amino-3-hydrazino-5-mercapto-1, 2, 4-triazole. *Microchimica Acta*, 180 (11-12): 1051-1057.

Wang, L.-L., Wang, J.-Q., Zheng, Z.-X. and Xiao, P. 2010. Cloud point extraction combined with high-performance liquid chromatography for speciation of chromium(III) and chromium(VI) in environmental sediment samples. *Journal of Hazardous Materials*, 177 (1-3): 114-118.

Wang, X., Wei, Y., Wang, S. and Chen, L. 2015. Red-to-blue colorimetric detection of chromium via Cr(III)-citrate chelating based on Tween 20-stabilized gold nanoparticles. *Colloids and Surfaces A: Physicochemical and Engineering Aspects*, 472: 57-62.

Wang, Z., Lee, J. H. and Lu, Y. 2008. Label-free colorimetric detection of lead ions with a nanomolar detection limit and tunable dynamic range by using gold nanoparticles and DNAzyme. *Advanced Materials*, 20 (17): 3263-3267.

Wei, H., Chen, C., Han, B. and Wang, E. 2008. Enzyme colorimetric assay using unmodified silver nanoparticles. *Analytical chemistry*, 80 (18): 7051-7055.

Wei, Q., Yan, L., Chang, G. and Ou, Q. 2003. Kinetic spectrophotometric determination of trace manganese(II) with dahlia violet in nonionic microemulsion medium. *Talanta*, 59 (2): 253-259.

Welch, C. M. and Compton, R. G. 2006. The use of nanoparticles in electroanalysis: a review. *Analytical and bioanalytical chemistry*, 384 (3): 601-619.

Wen, B., Shan, X.-Q. and Lian, J. 2002. Separation of Cr(III) and Cr(VI) in river and reservoir water with 8-hydroxyquinoline immobilized polyacrylonitrile fiber for determination by inductively coupled plasma mass spectrometry. *Talanta*, 56 (4): 681-687.

Wu, S.-P., Chen, Y.-P. and Sung, Y.-M. 2011. Colorimetric detection of Fe(III) ions using pyrophosphate functionalized gold nanoparticles. *Analyst*, 136 (9): 1887-1891.

Wu, X., Xu, Y., Dong, Y., Jiang, X. and Zhu, N. 2013. Colorimetric determination of hexavalent chromium with ascorbic acid capped silver nanoparticles. *Analytical Methods*, 5 (2): 560-565.

Wyszecki, G. and Stiles, W. S. 1982. Color science: concepts and methods, quantitative data and formulas. *Wiley*,

Xin, J., Miao, L., Chen, S. and Wu, A. 2012. Colorimetric detection of Cr(III) using tripolyphosphate modified gold nanoparticles in aqueous solutions. *Analytical Methods*, 4 (5): 1259-1264.

Xing, S., Xu, H., Chen, J., Shi, G. and Jin, L. 2011. Nafion stabilized silver nanoparticles modified electrode and its application to Cr(VI) detection. *Journal of Electroanalytical Chemistry*, 652 (1-2): 60-65.

Yoosaf, K., Ipe, B. I., Suresh, C. H. and Thomas, K. G. 2007. In situ synthesis of metal nanoparticles and selective naked-eye detection of lead ions from aqueous media. *The Journal of Physical Chemistry C*, 111 (34): 12839-12847.

Yu, Y., Hong, Y., Wang, Y., Sun, X. and Liu, B. 2017. Mecaptosuccinic acid modified gold nanoparticles as colorimetric sensor for fast detection and simultaneous identification of Cr(III). *Sensors and Actuators B: Chemical*, 239: 865-873.

Zaw, M. and Chiswell, B. 1999. Iron and manganese dynamics in lake water. *Water Research*, 33 (8): 1900-1910.

Zhang, H., Liu, Q., Wang, T., Yun, Z., Li, G., Liu, J. and Jiang, G. 2013. Facile preparation of glutathione-stabilized gold nanoclusters for selective determination of chromium(III) and chromium(VI) in environmental water samples. *Analytica Chimica Acta*, 770: 140-146.

Zhang, X.-X., Tang, S.-S., Chen, M.-L. and Wang, J.-H. 2012. Iron phosphate as a novel sorbent for selective adsorption of chromium(III) and chromium speciation with detection by ETAAS. *Journal of Analytical Atomic Spectrometry*, 27 (3): 466-472.

Zhang, X. and Wandell, B. A. 1996. A spatial extension of CIELAB for digital color image reproduction. In: Proceedings of *SID international symposium digest of technical papers*. Citeseer, 731-734.

Zhao, L., Jin, Y., Yan, Z., Liu, Y. and Zhu, H. 2012. Novel, highly selective detection of Cr(III) in aqueous solution based on a gold nanoparticles colorimetric assay and its application for determining Cr(VI). *Analytica Chimica Acta*, 731: 75-81.

Zheng, Y., Wang, Y. and Yang, X. 2011. Aptamer-based colorimetric biosensing of dopamine using unmodified gold nanoparticles. *Sensors and Actuators B: Chemical*, 156 (1): 95-99.

Zhou, Y., Dong, H., Liu, L., Li, M., Xiao, K. and Xu, M. 2014. Selective and sensitive colorimetric sensor of mercury(II) based on gold nanoparticles and 4-mercaptophenylboronic acid. *Sensors and Actuators B: Chemical*, 196: 106-111.

Zhou, Y., Zhao, H., Li, C., He, P., Peng, W., Yuan, L., Zeng, L. and He, Y. 2012. Colorimetric detection of Mn(II) using silver nanoparticles cofunctionalized with 4-mercaptobenzoic acid and melamine as a probe. *Talanta*, 97: 331-335.

Zielińska, A., Skwarek, E., Zaleska, A., Gazda, M. and Hupka, J. 2009. Preparation of silver nanoparticles with controlled particle size. *Procedia Chemistry*, 1 (2): 1560-1566.